THE UNIVERSITY OF CHICAGO

DESIGN AND FABRICATION OF CEPHALIC VEIN MODELS OF END STAGE RENAL DISEASE PATIENTS FOR HEMODYNAMICS CHARACTERIZATION

A DISSERTATION SUBMITTED TO

THE FACULTY OF THE DIVISION OF THE PHYSICAL SCIENCES

AND

THE FACULTY OF THE DIVISION OF THE BIOLOGICAL SCIENCES

AND THE PRITZKER SCHOOL OF MEDICINE

IN CANDIDACY FOR THE DEGREE OF

DOCTOR OF PHILOSOPHY

GRADUATE PROGRAM IN BIOPHYSICAL SCIENCES

BY

ANDRÉS MOYA RODRÍGUEZ

CHICAGO, ILLINOIS

DECEMBER 2022

Lo importante es participar.

Contents

List of Figures

List of Tables

Acknowledgements

To my soul sister, Glory: You have been constant source of support, laughter and encouragement throughout the PhD experience and I doubt I would have finished it without you in the picture. Thank you for roasting me to tears (of laughter)! It does build character and has made this ride much more fun and colorful! Love you with all of my being and I am forever indebted to you. Now, let me help getting you across your own PhD finish line. I've got you.

To my lovely Mike: If I could only put in words how instrumental you have been for the completion of this doctorate. It was truly a blessing to have met you just days before the pandemic hit. Your unconditional love and support have made quarantine and the later stages of the PhD much more manageable. Thanks for being patient and understanding with me when the going got tough, heavens know I am not the easiest person to deal with when under a lot of pressure. This PhD got completed because of the support of one extraordinary buckaroo like yourself. I will forever love you, dearest and darling Mike.

To my family: Mami, René, Lorein, tití Uíto, Razy, María, Che y Tata, thanks for the pep talks, pampering me and feeding me delicious dishes every time I visited the motherland. Seeing you all excel and succeed in your respective fields despite all of life's hardships has been truly inspiring and motivated me to work harder with each passing day. I could not be prouder of every single one of you and cannot wait for all of us to reunite soon in the warm, lively and lovely Puerto Rico! ¡Capitanes, ahí!

To my López-Garriga lab family: Ramonita, Josiris, Elddie, Gardi, Darya, Bessie, Los Carlos, Rafael, Ruth y Garriga, I do not think I could have been introduced to science by a better research group. Your enthusiasm and commitment to community outreach and teaching the youth of Puerto Rico made the process of learning about science and making discoveries extremely fun! Your collective and individual influences on me starting up in the academic world truly inspired me to embark on the PhD journey. To this day, I still consider you the gold standard when it comes to getting people excited about science. Highly respect and appreciate you all and never lose the fun-loving and enthusiastic scientific spirit within you.

To my chosen family: Jessy, Whitney, Christian, Cisco, Raymond, Joel, Stephen, Jonas, Wasserboiii, Jill, Sylvia, Gabi, Dulce, Gloriví and Grace, thanks for adding so much color to the picture when days looked grim and grey! Love you all, you crazy bunch, and I treasure all of our shared experiences which most certainly helped ease the stress and turmoil during the PhD route. When I felt like giving up, you re-kindled the fire within me and lifted my spirits to summon the strength to keep moving forward. For that I am forever grateful. Thanks for letting me be a part of your lives. You make me feel like I am one heck of a lucky guy.

To my previous research mentors: Caleb Levar, Daniel Bond, “Pancho” Bezanilla, Joao De Souza, Michael Priest, Tomoya Kubota, Jorge Sánchez-Rodríguez and Lisa Petti, thanks for giving me the opportunity to be a part of your lab. Your patience, empathy and professionalism while training me back then are qualities I mimic as best as I can when training the new generation of scientists. Wholesomely appreciate how you introduced me to very diverse research projects that forged me

into a confident scientist when facing fields outside my comfort zone. You were key for me to mature culturally, professionally and personally and for that I thank you all!

To Julie and Michele: You were undoubtedly the highlight of being part of BPHYS. Our hot chocolate morning conversations kept me sane and in check when the project or life in general was going sideways. Because of you I was able to get the NSF GRFP, develop leadership skills and the peer mentoring program while getting some laughs along the way. You are the heart of BPHYS and your commitment to your graduate students make you the greatest asset. Here's to more chit-chats with my gal pals, love you both!

To the Basu group: Thanks to all the past and current Basu group members for all the emotional and technical support given throughout this crazy process. The collaborative and light-hearted lab culture you have fostered is truly something magical. Your kindness, constructive feedback and contributions to this project undoubtedly helped keep the science moving forward while making facing new challenges way less intimidating. You are a very very special group!

To Oni and Mary: I am especially grateful to you. It is pretty amazing how your leadership and mentoring has allowed a non-engineer nor computer scientist to be able to make all of these computational models and millifluidic devices. I came in completely unfamiliar to all aspects of this dissertation project, but through your encouragement, understanding and mentoring, we were able to do something very special for the end-stage renal disease population. I wish you all the best with this project's future and will forever cherish my time as your graduate student.

To my thesis committee members, Dr. Yun Fang and Dr. Kenneth Bader: You two were absolute lifesavers considering you joined in as part of my thesis committee during the later stages of the project. Your willingness to help out a student in need and your enthusiasm regarding the science I do was a nice (and necessary) breath of fresh air. Thanks for making our committee meetings feel relaxed, good-spirited and full of helpful advice and constructive criticism. It really helped me orient myself on my research while making the workload seem more manageable**.** You are two incredible scientists and I feel lucky to have you around for guidance towards the PhD.

Abstract

In this doctoral dissertation, we expand on how we engineered replicas of vein geometries prone to pathologic vein lumen narrowing and blood clot formation, also known as stenosis and thrombosis, respectively, in end-stage renal disease patients undergoing hemodialysis treatment. Our main goal is to develop millifluidic technology that serves as a research tool to study patient-specific hemodynamics *in vitro* which can potentially help elucidate vascular pathogenesis mechanisms. Here, we elaborate on how we created cephalic vein computational models of our patient cohort to explore hemodynamics via computational fluid dynamics flow simulations. Moreover, we show how we fabricated millifluidic devices parting from these cephalic vein computational models to experimentally characterize hemodynamics under healthy physiologic flow rates. Alas, future efforts to mimic pathologic flow conditions for hemodynamics characterization will help us contrast resulting wall shear stress from that obtained from healthy flow conditions to better understand stenosis and thrombosis in the cephalic vein arch.

The developed and patented technology presented here would allow for systematic dissection of stenosis and thrombosis contributing factors in order to shed light onto the heterogeneity in vascular complications and vascular access outcomes during hemodialysis. Moreover, these devices could also contribute to the discovery of more efficient anti-thrombotic and thrombolytic medication that ultimately serves our mission; to improve the quality of life of hemodialysis patients by understanding and preventing clotting complications and advance vascular clinical care.

Chapter 1

Introduction

1.1 End-Stage Renal Disease, Hemodialysis and Arteriovenous Fistulas

End-stage renal disease (ESRD) is a terminal illness where kidney function is severely compromised, leading to poor excess fluid and waste products excretion from the body which can lead to systemic complications [1]. In order to compensate for poor kidney function and sustain life, hemodialysis is often employed to treat patients when a kidney transplant is not an available option. During hemodialysis the patient's blood is artificially filtered through a hemodialyzer and returned to the patient in 3 to 4-hour sessions thrice a week. Moreover, in order to provide this treatment, a robust access point to the patient's blood is needed; thus, an arteriovenous fistula (AVF) is created. AVF remains the gold standard for hemodialysis treatment compared to other methods such as: central venous catheter, arteriovenous graft and peritoneal dialysis catheter where higher frequency of access infection and clotting is observed in the clinic [1]. An AVF entails the

surgical junction of an artery and a vein in order to artificially drain high blood flow rates and pressures from the arterial system directly into the low flow rate and pressure venous system [2]. This procedure forces the vein to adapt to the sudden increase of blood flow by remodeling its geometry in the form of vein lumen diameter and wall thickness increase [2]. This results in larger and stronger veins that are able to whistand the excess arterial blood input and high filtration rates of hemodialysis while accommodating the large needles used for this treatment.

Among the 492,000 patients receiving regular hemodialysis in the United States, 64% (275,000 patients) have an AVF for their vascular access which allows for patient blood filtration [1]. Two thirds of all AVFs placed in the US are in the upper arm using the brachiocephalic (BCF) configuration, which commonly fails due to cephalic arch stenosis (14-60%) and thrombosis (17-28%) [3-5]. The BCF is created by an anastomosis between the brachial artery and the cephalic vein in the upper arm (**Fig. 1.1**) [6].

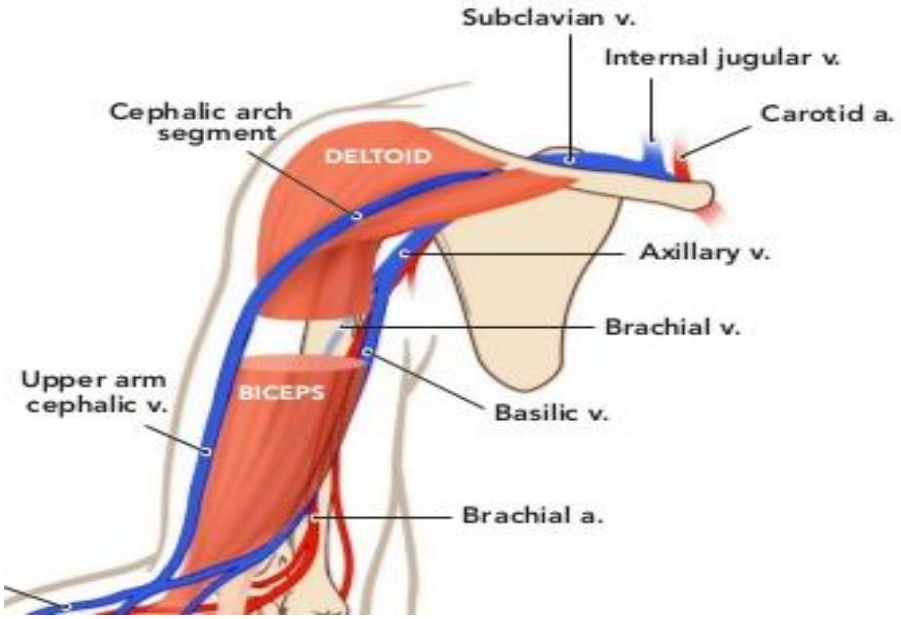

Figure 1.1: Schematic of the venous and arterial anatomy in the upper arm depicting the brachial artery, the cephalic vein and cephalic arch extracted from the Dialysis Access Atlas [6].

Failed AVFs lead to missed hemodialysis sessions, which contributes to the morbidity, mortality and financial burden of interventional procedures for ESRD patients [7]. Efforts have been spent on increasing the success rates of AVF maturation and maintenance while decreasing the mortality rate on these patients with Japan demonstrating promising outcomes compared to other nations [8-20]. Moreover, our understanding of the mechanisms of stenosis and thrombosis in renal failure is incomplete because we lack specific tools to study these in AVF clinical scenarios. Traditional anti-platelet and anti-coagulants do not effectively prevent or treat access thrombosis and can cause significant side effects [21, 22]. In the absence of reliable clinical predictors of thrombosis, the current standard of care is to treat AVF thrombosis *a posteriori.* Consequently, there is an urgent need to define how thrombosis occurs in ESRD downstream from the vascular access in order to establish effective treatment options or preventative care.

1.2 Cephalic vein arch

1.2.1 Anatomy

We concentrate on the cephalic arch as we posit that its geometric bend has rheological implications since this is where stenosis and thrombosis commonly occur [23]. The cephalic vein is lateral and superficial in the upper arm with a final bend called the cephalic arch that terminates at the axillary vein called the cephalic arch (CA) (**Fig. 1.2**).

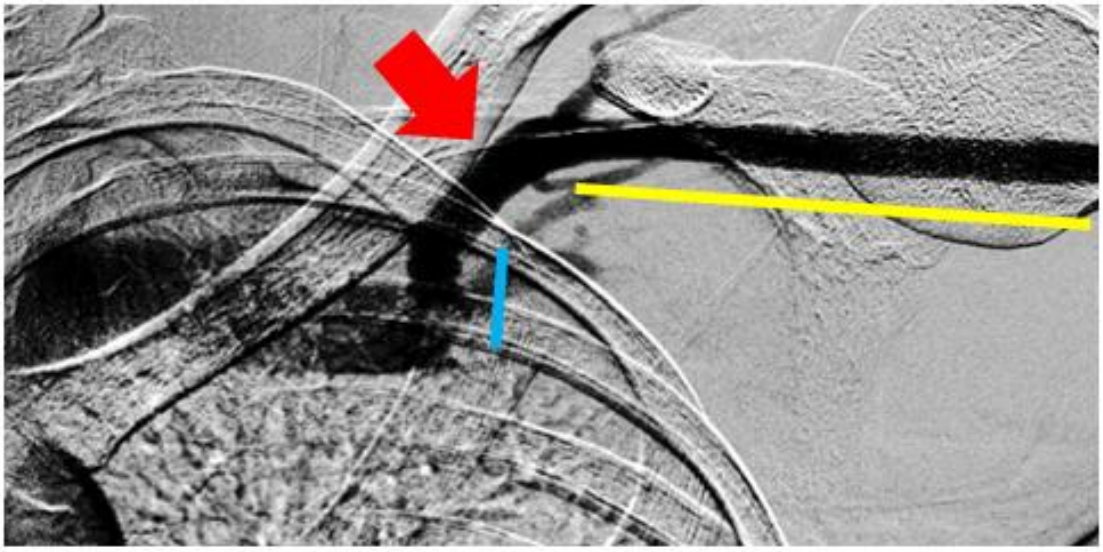

Figure 1.2: Venogram showing the straight cephalic vein (Prebend; yellow), the bend of the cephalic arch (Bend; red arrow) and straight vein (Postbend; blue).

Using the BCF venous portion to access the patient by means of syringes, the hemodialyzer filters patient blood at rates usually surpassing 300 mL/min. To put this in perspective, a native cephalic vein can have blood flow rates spanning from [3 – 44] mL/min, whereas the surgically connected brachial artery inherently have blood flow rates of >700 mL/min [24-27]. The patient cohort studied here had BCFs, which roughly translates to their respective cephalic veins adapting to an influx arterial blood flowing at >15 times the healthy flow rates of cephalic veins.

1.2.2 Stenosis and Thrombosis

While the BCF provides a superb location for cannulation needed at every hemodialysis session, pathological complications of venous outflow stenosis and thrombosis, specifically of the CA are all too common [28]. Stenosis is referred to the longitudinal and pathological narrowing of blood vessels and it is the leading cause of BCF failure [29]. Unfortunately, CA stenosis (CAS) tends to resurface even after it has been treated, sometimes repeatedly, by means of stents, angioplasty and surgical revisions [28]. Moreover, Hammes et al documented that CAS prevalence

in ESRD patient population with BCF is ~77% [30]. Previous comparative studies focusing on CAS prevalence in diabetics and non-diabetics found no real difference between the two populations, but determined that the mean number of years for CAS development is 2.93 ± 1.93. This presents a huge burden on ESRD patients given that BFC patency is need for treatment, but the BCF will be usable for approximately 3 years before collapsing.

Consequently, hemodialysis sessions are potentially missed due to costly interventions to: 1) mend the stenosed CA, 2) clear blood clots that potentially formed during BCF failure, 3) create an alternate fistula for future treatment and 4) provide temporary dialysis treatment while the newly created fistula matures which is not an infallible process to start with. These complications alongside the pathologic detriment of the terminal disease and missed hemodialysis sessions when CAS and BCF failure occurs greatly hinders the quality of life of these patients.

Mechanistically, scientists have suggested that CAS occurs post-BCF creation due to the cephalic vein adapting to the increased and pulsating sheer rates which trigger neointimal hyperplasia [29]. The latter refers to the pathologic muscle layer growth in blood vessels which results in hypertrophic vein remodeling and a decrease in lumen diameter, and thus, stenosis. Studies reveal that CAS occurs predominantly in the arch postbend region upon venogram evaluations. This is the region close to the end of the cephalic vein where blood drains into the axillary vein [29]. Nonetheless, another study suggested that the inner bend of the cephalic arch would the most prone to stenosis, but closer inspection of hemodynamics across the entire arch is necessary to forge a concrete biophysical foundation of the pathology [31]. This could result in patient care optimization in the dialysis unit to prevent further vascular complications.

On the other hand, thrombosis is often the aftermath of CAS [32]. Thrombosis is the formation of blood clots in blood vessels which can lead to severe complications such as

myocardial infarction, strokes, limb ischemia, deep vein thrombosis and pulmonary embolism [33]. Maturation failure, meaning failure of the vein to dilate and thicken prior to use for hemodialysis treatment, occurs in 26-60% of patients with BCF often due to early thrombosis [34, 35, 36]. The mechanism of why these complications occur is mostly unknown, but past research efforts have pointed towards altered hemodynamics in the CA causing stenosis which often leads to thrombosis and loss of access.

1.2.3 Hemodynamics

The CA is an area of active and persistent geometric remodeling due to abnormal hemodynamic flow initiated with the surgical creation of the AVF. The cephalic vein experiences increased pulsatile flow velocities from the brachial artery which is transmitted up to the CA bend. As the vein dilates over time, the high flow velocities, pulsatile flow and the geometric bend of the CA, together, lead to abnormal hemodynamics in the region, including turbulent flow conditions and abnormal wall shear stress (WSS), that promote formation of stenosis, recurrent thrombosis, and eventual access failure [37, 38, 39].

Vascular pathogenesis can be better understood if cephalic arch geometries and flow conditions are faithfully recreated for extensive *in vitro* studies. This way, hemodynamics can be dissected in terms of local acting forces which are intimately tied to vessel geometry, blood viscosity and flow rate. These forces are best described by wall shear stress (WSS). Although BCF creation initially increases overall WSS due to dramatically increased blood flow, computational modeling showed that low WSS develops in the cephalic arch over time [37, 40]. 2D computational fluid dynamics of the cephalic arch revealed that local WSS in the curved region of the arch can be lower than the physiologic range [76-760 mPa], which can promote venous stenosis and

thrombosis [41]. We performed a five-year study of an ESRD patient cohort with upper arm BCF and observed that venous stenosis was common, and 40% of patients experienced thrombosis resulting in loss of access. We and others found that AVF placement predisposed the cephalic vein to increased blood flow velocity, pulsatile flow, areas of low WSS, and increased risk of stenosis and thrombosis [37, 40-44].

Past computational fluid models have shown the importance of the endothelium in thrombosis and established the flow and direction of WSS [41, 45] in the AVF, but these models do not provide a research platform with which to perform time-dependent perfusion experiments for testing hypothesis or intervention options. Given the larger cephalic vein diameters and increased flow rates associated with AVF, microfluidic systems used to study arterial circulation are not applicable to study complex patient-specific hemodynamics in large vein geometries [46]. This thesis highlights the development of a novel application of routine diagnostic measures such as Intravascular Ultrasound (IVUS) and venogram to create patient-specific millifluidic models of the cephalic vein arch downstream of flow in the AVF.

Although WSS, pressure and pulsatility are important determinates of AVF maturation, the roles that these parameters play in thrombosis, stenosis and AVF failure arising in ESRD patients undergoing hemodialysis are poorly quantified and *in vivo* measurements of these parameters are problematic. Computational modeling can be a powerful engineering tool to model hemodynamic parameters in vascular systems, given the problems inherent in rigorous hemodynamic assessment and WSS derivation. Efforts to derive WSS by computational modeling have been done but only in a small number of cases [47, 48]. The longitudinal assessment of an AVF with repeated imaging and measurements as it matures is needed to understand the complications and longevity of the AVF [49].

Chapter 2

Creating Patient-Specific Cephalic Vein Computational Models

2.1 Introduction

In the current investigation, we modeled the three-dimensional (3D) geometries of the CA from five ESRD patients at two time-points using venogram and intravascular ultrasound (IVUS) at 3 and 12 months (mo.). The 3D model captures the irregularities of vein geometry that are easy to miss in two-dimension (2D), especially if these irregularities do not lie in the plane of 2D imaging. IVUS gives a microscopic snapshot; venogram captures the global topology but in 2D. Combining these, we can get a nuanced view of the CA geometry. We then used patient-specific flow velocities and pulse rates (from Doppler measurements), patient-specific whole blood viscosity and average intra-vascular pressures to simulate patient-specific hemodynamic flow in the 3D models of the CA. We performed hemodynamic modeling in 5 patients at 3 and 12 months (mo.) after the surgical placement of the AVF. Our simulations showed regions of interest where low WSS or stenosis is likely to develop. Even as early as 3 mo. we could predict areas of abnormal hemodynamics in the CA models. These areas were likely to worsen with time and seemed to exacerbate in the same patient's CA model at the 12-mo. time-point. The overall aim of this work is to demonstrate the feasibility of computational modeling to unveil abnormal flow dynamics in the CA that are unique to individual patients. Our first hypothesis is that abnormal hemodynamics

and high flow velocities in the CA can predict areas of interest that develop into stenosis and associated pathological conditions. Our second hypothesis is that the hemodynamics modeled from actual detailed anatomic vein images are unique of each patient and differ based on the maturation of the AVF.

2.2 Methods and Materials

2.2.1 Trial Design and Protocol

This prospective observational trial was conducted at a single center University-affiliated medical center from December 16, 2011 through April 20, 2020. This protocol [6] was approved by the Institutional Review Board from the University of Chicago (Protocol number 11-0269) on August 10, 2011. The current study details the 5 subjects included as a subset for a small-scale study that had Doppler, venogram and IVUS imaging at 3 mo. and 12 mo. This trial was conducted with good clinical practice and the Declaration of Helsinki. The trial was registered at ClinicalTrials.gov (NCT 01693263) August 8, 2012. Informed consent was obtained in writing prior to any trial-related activities.

This study represents a cohort of a larger population enrolled to determine the hemodynamic consequences of the post-fistula environment. Patients were consented to enroll in the study if they had advanced renal failure or were on hemodialysis in need of a permanent access with a BCF planned. During the study 161 patients consented, but only 40 completed the study [40]. Five subjects were chosen from the 161 consented for inclusion in the study as we selected subjects with presumed normal anatomic configuration of the BCF without previous catheter access on the side of the AVF (**Fig. 2.1**).

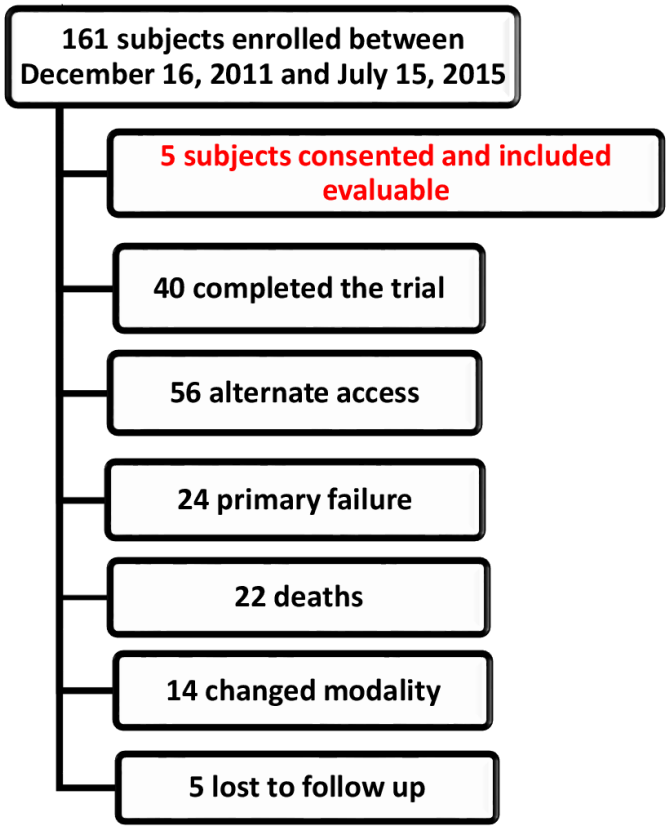

Figure 2.1: Study subject inclusion and discontinuation. Of 161 subjects enrolled, 5 subjects were suitable and agreed to participate with IVUS measurements at 3 and 12 months. 40 subjects completed the trial, 56 had alternate access placed, 24 had primary failure and never used the access for dialysis, 22 deaths occurred which were unrelated to the study, 14 subjects either received renal transplant or transitioned to peritoneal dialysis, and 5 subjects were lost to follow-up.

The 5 patients included in the study were brought to the cardiac catherization lab and the following were obtained by an interventional cardiologist and radiologist sequentially on the same day: Venous blood sample for whole blood viscosity (WBV); Doppler spectral analysis; 2D venogram imaging and IVUS of the CA. WBV was measured from venous blood samples obtained on the day of the protocol study. The blood was drawn during intravenous insertion on the day of the protocol and collected in 4.5 mL tubes containing 3.2% buffered sodium citrate. WBV was measured using a Brookfield programmable DV-II+ cone and plate viscometer. The WBV was measured at 220 s^{-1} at 37 ºC [50]. Three measurements of viscosity were determined at the above

shear rate and the average value was used for the simulations. Spectral Doppler analysis of the CA was made at the same location in all patients. The point of measurement was marked 10 cm from the greater tubercle of the humerus as previously reported [46] which was approximately 10 cm proximal to the CA. The peak systolic velocity at a 60-degree angle of insonation was measured. The optimal Doppler angle to measure blood flow velocity is between 45 and 60 degrees [51, 52]. A 60-degree angle of insonation was used to standardize the velocity measurements as the Doppler angle of insonation has a significant effect on spectral Doppler velocity measurements [52]. Velocity measurements were taken three times, approximately 1 minute apart and then averaged. 2D venography was performed in the angiography suite by an interventional radiologist. Vascular access was obtained in the direction of the venous outflow using a micropuncture system (Cook Medical Inc., Bloomington, IN). A digital subtraction angiogram (DSA) fistulogram was then performed through the 5 French Pinnacle vascular introducer sheath (Terumo Medical Corporation, Somerset, NJ) with imaging of the venous outflow from the puncture site to the right heart. Over a 0.035-inch guide-wire, a 5 French diagnostic multipurpose angled catheter (Boston Scientific, Natick, MA) was then advanced to a straight portion of the cephalic vein approximately 10 cm downstream from the CA. A high-fidelity pressure monitor (Namic Preceptor Morse Manifold; Boston Scientific) was connected to the end of the catheter and intravascular pressure measurements were obtained. Next, a 0.014 in x 180 cm Asahi Prowater coronary guidewire (Asahi Intecc USA, Inc., Irvine, CA) was advanced through the cephalic arch under the guidance of a fluoroscopic map and IVUS was performed using a Volcano Eagle Eye Platinum 20 MHz IVUS catheter (Philips, Amsterdam NE). Images were obtained at 30 fps during automated pullback of the catheter from the axillary vein to the cephalic vein at a rate of 1 mm/sec.

2.2.2 Image Processing and 3D Reconstruction of the Cephalic Arch

Image processing was performed on venogram, IVUS, and Doppler image sets with ImageJ (NIH, USA) and MATLAB (Mathworks) and 3D reconstructions of the CA for each patient were generated using Computer Aided Design (CAD) software- AutoCAD (Autodesk) and SolidWorks (Dassault Systèmes). We used a venogram recording to capture the gross anatomy of the CA, including the cephalic bend (**Fig. 2.2**).

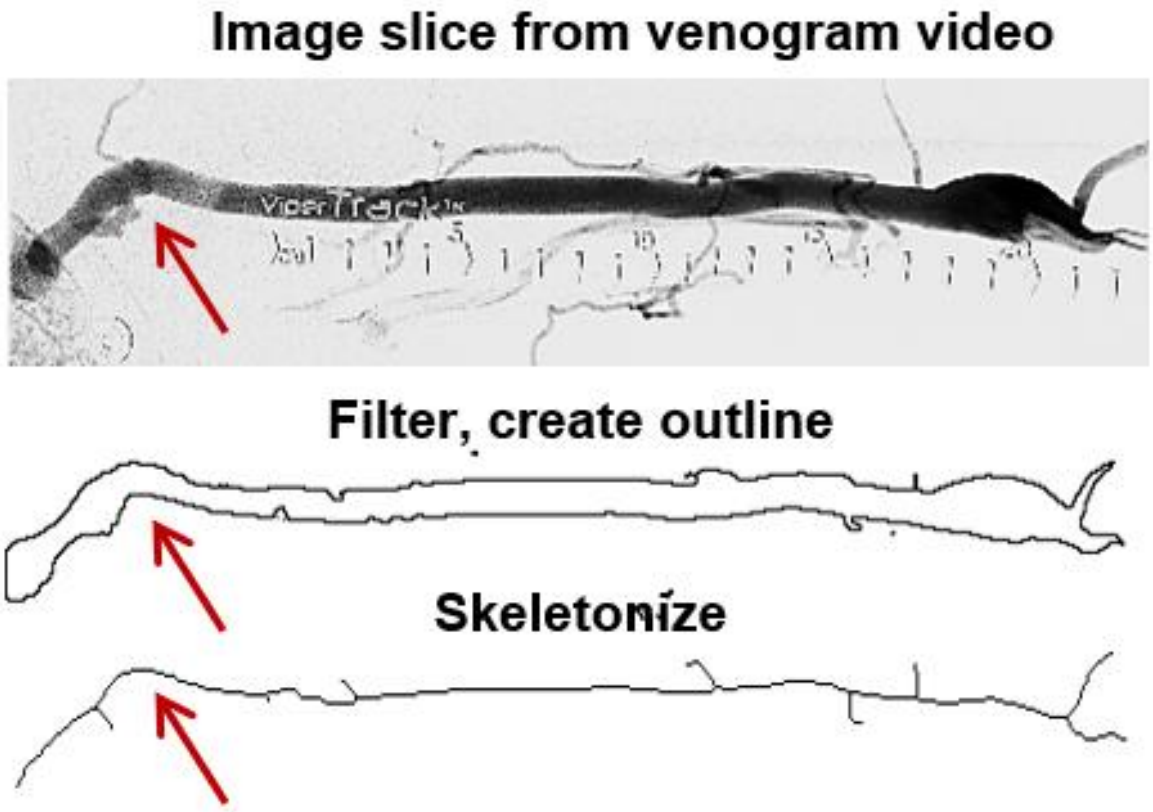

Figure 2.2: Step-by-step processing of venogram to reconstruct the 3D geometry of a patient's cephalic arch (CA) downstream of AVF placement that are used to calculate internal vein contours. Red arrows indicate the CA.

Briefly, all image slices were aggregated using the 'Z Project' function and 'minimum intensity' option in ImageJ to generate a 2D projection of the CA. This image was converted from gray-scale to binary (using 'Make Binary' function), cleaned to remove any features that are not associated with the CA (using 'Clear' function), inverted (using 'Invert' function) and the contour

of the CA was extracted (using 'Skeletonize' function). The skeletonized image was exported in .tiff format, converted into vector graphics files (as .svg) and finally converted into a CAD file format (.dxf) that can be imported into AutoCAD and SolidWorks for 3D modeling.

IVUS images with non-directional color flow imaging (ChromaFlo), capturing 1/30 mm increments of the vein path per frame were recorded in the standard DICOM format. These pullback measurements set the lower limit of resolution along the z axis as ~1 mm. The vein contours were traced manually. The outline of the vein lumen's cross-section of every 30^{th} image of the IVUS image stack was traced onto the image frame using ImageJ, the outline was binarized, and the X and Y coordinates of the CA's cross-sectional outline for each slice were extracted using MATLAB, as shown in **Fig. 2.3**.

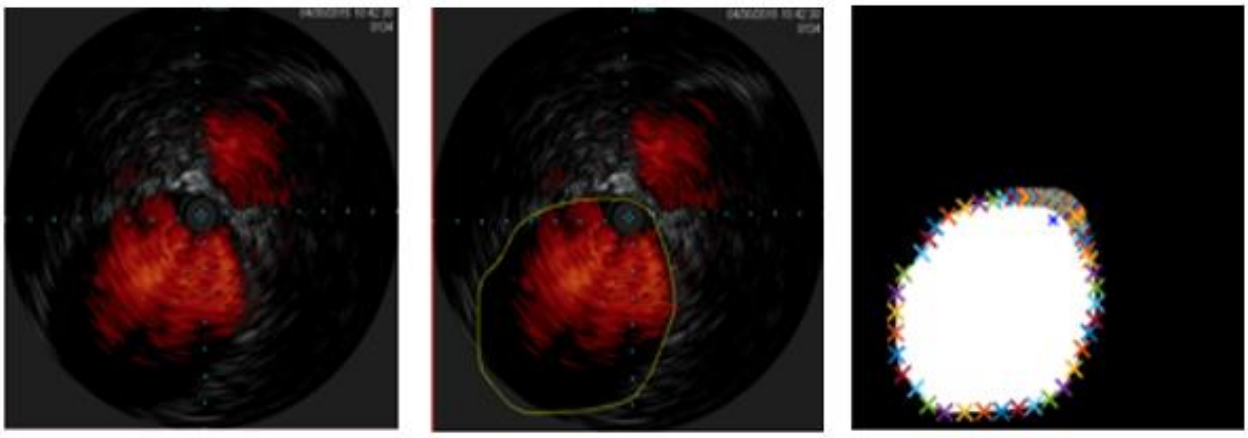

Figure 2.3: Step-by-step processing of IVUS to reconstruct the 3D geometry of a patient's cephalic arch (CA) downstream of AVF placement that are used to calculate internal vein contours.

Each slice of the IVUS at 500 x 500 $pixel^2$ or 16 x 16 mm^2 was thus processed and exported as individual files. The files were batch-processed using the free '*dxf2dwg*' plug-in for AutoCAD to generate corresponding .dwg files.

The area inside the traced contour in each slice was calculated in AutoCAD using the 'Extract Data' function, under the 'Annotate' tab. This step was processed in the batch-processing mode for all IVUS slices for a given time-point (3 or 12 mo.) and exported as a single text file. The mean area of cross-section and the standard deviation were calculated for all slices. The average diameter of the patient's CA was calculated from the cross-sectional area, as $2*(\text{area}/\pi)^{1/2}$. The arch angle was obtained from the venogram by marking two straight sections of the brachial vein- one upstream and the other downstream to the bend, drawing tangents to the two sections, and measuring the angle inscribed between the tangents at the point where they intersect [19].

The 3D model of the CA was reconstructed by combining the global topography of the skeletonized venogram with the local topography of the contours of the vein's cross-sections from IVUS. X and Y coordinates defining each slice's cross-section were imported into AutoCAD, where the contour was properly scaled, and the geometric center of each cross-sectional slice of the vein lumen was marked. A detailed and complete 3D model of the CA was generated in SolidWorks software by importing each contour to a plane perpendicular to the path at 1 mm intervals, and aligning the center of mass of the contour with the vein path, as shown in **Fig. 2.4**.

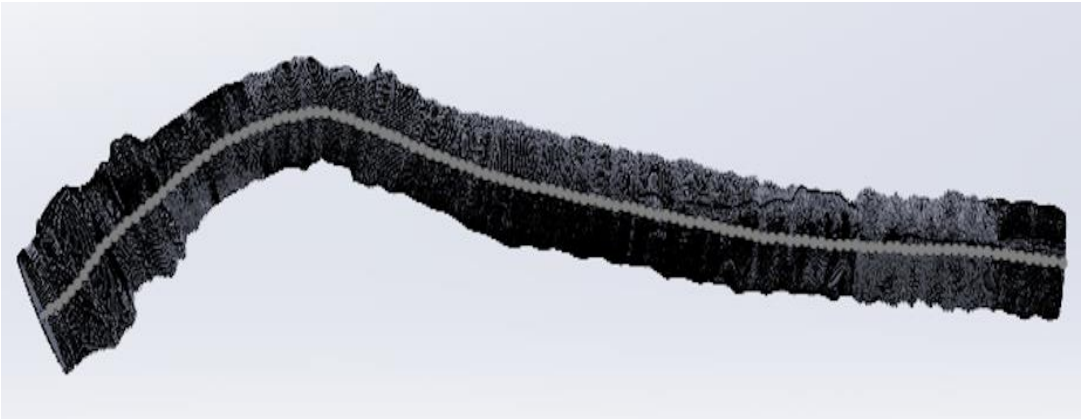

Figure 2.4: Venogram and IVUS data are combined to reconstruct model of the patient's CA in 3D.

Using the knowledge that IVUS imaging of the CA began at the axillary vein and then moved into the CA, we utilized the rapid shift in diameters of IVUS contours to align the correct IVUS frame with where the CA model began along the skeletonized path obtained from the venogram. The digital 3D model was then lofted together across all contours, creating a smooth curved surface along the structure, shown in **Fig. 2.5** to replicate the continuous curvature of the vein. Designs for five subjects at 2 time-points each (3 and 12 mo.) were thus generated (**Fig. 2.6**).

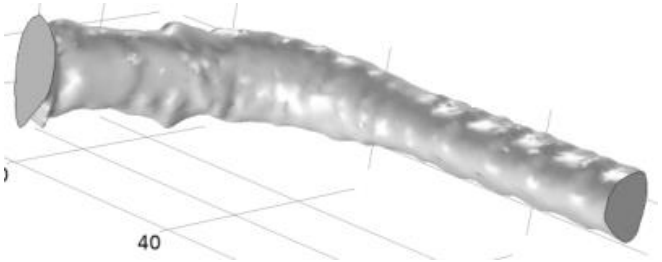

Figure 2.5: Reconstructed model shown is lofted and smoothed to render the 3D model used for flow simulation.

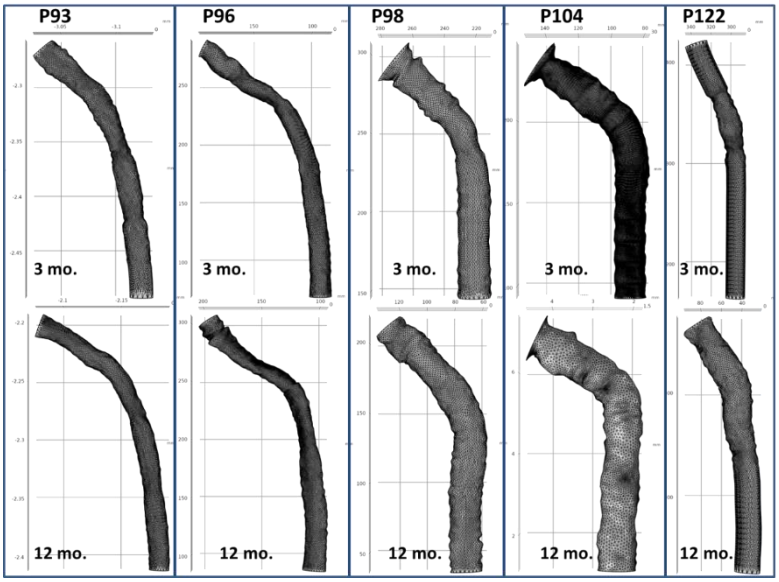

Figure 2.6: Three dimensional models of cephalic arches in five ESRD patients obtained 3 months (top) and 12 months (bottom) after their AVF placement.The models, displayed in the xy-plane, are reconstructed from venogram and IVUS imaging.

2.3 Conclusions

In the current study, we successfully modeled the CA in 3D using two independent and orthogonal imaging techniques, viz., IVUS and venogram. Being able to visualize the model in 3D helped identify stenosis and other topological irregularities that may not be directly evident in a 2D image taken on a single, fixed plane. We observed the overall geometry for the CA, including average vein diameter, arch angle, and irregularities in the vein walls to be highly variable between subjects that can be associated with pathologic stenosis at later time points, e.g., P93, P96 and P122. This heterogeneity coupled with variations of hemodynamic parameters of each patient, e.g., velocity, viscosity, pulsatility, etc., measured independently through Doppler and viscosity tests, make the CA an interesting but complex system to study. Individualized computational modeling can be of great importance in understanding the contribution of each of the above parameters to the CA remodeling and/or AVF failure.

2.4 Acknowledgements

We thank Travis Bee for helpful advice on 3D modeling. The work was partly funded by the Ginny and Simon Aronson Research Award, University of Chicago Institute of Translational Medicine Pilot Award, and A.B.'s research development funds. We thank all the patients who gave their time for the procedures.

Chapter 3

Computational Fluid Dynamics

3.1 Introduction

While attempts to computationally model vasculature for the surgical placement of an AVF [53] and to track geometric and hemodynamic alterations as an AVF matures have been done [54], to our knowledge, this is the first study that models geometry and flow in ESRD patients using the exact geometry of the cephalic arch in 3D at different time-points using patient-specific parameters. We note that there is significant heterogeneity between patients and between time-points which makes any conclusions made from population-averaged data difficult to interpret. Hence, we underscore the need for patient-specific models to understand the range of possible hemodynamic conditions in the CA and predict outcomes.

3.1.1 Reynolds number

Reynolds number, $Re = \frac{\rho u L}{\eta}$ is a dimensionless parameter used to characterize flow. At low *Re*, flow is laminar but transitions to turbulent as *Re* increases, along with the appearance of eddies and vortices. *Re* was calculated for each subject at 3 and 12 mo. time-points, where *u* is the peak systolic velocity measured from Doppler, *L* is the average vein diameter measured from IVUS and

η is the WBV measured from viscosity measurements. Density, ρ was set to 1060 kg/m^3, the average density of whole blood [55].

3.2 Flow Simulation Methods

We used COMSOL Multiphysics (COMSOL Inc.), version 5.5, Physics simulation software based on finite element analysis and partial differential equations [COMSOL], to simulate blood flow in the CA of patients with ESRD. In addition to the 'Multiphysics' module, the 'Microfluidics' and CAD import' modules were also used. Since *Re* < 2,000 for all patients (**Table 3.1**), all flow were simulated using the 'Single Phase Flow' and 'Laminar Flow' physics.

Table 3.1: Patient Measured and Calculated Parameters

Patient ID: Time point	Systolic velocity (cm/s)	Diastolic velocity (cm/s)	WBV (cP)	B/P (mm Hg)	Pulse (beat/ min)	Vein area of X-sections (cm^2)	Vein diameter (cm)	Reynolds number	Arch angle (^{o})
P93: 3-month	17.6	9.4	4.12	134/84	83	0.513	0.81	367	145
P93: 12-month	17.6	5.7	3.96	119/81	71	0.337	0.66	311	113
P96: 3-month	66.6	38.3	2.96	174/96	101	0.347	0.66	1,574	133
P96: 12-month	43.5	21.0	4.08	122/70	81	0.337	0.66	746	132
P98: 3-month	49.7	38.2	3.20	130/76	90	0.532	0.82	1,350	130
P98: 12-month	17.6	8.2	3.86	143/82	79	0.840	1.03	498	115
P104: 3-month	39.6	29.2	2.68	124/80	81	0.930	0.90	1,723	125
P104: 12-month	9.4	4.6	4.63	125/81	84	0.594	1.10	194	115
P122: 3-month	52.5	24.3	3.96	99/60	88	0.559	0.84	1,180	150
P122: 12-month	56.6	41.2	3.35	130/74	88	0.935	1.09	1,952	152

WBV = whole blood viscosity

To test the effect of fluid flow in an idealized, simplified CA, we generated an idealized 3D vein model with a diameter of ~ 9.5 mm and a bend angle of 125^o (**Fig. 3.1**) to mimic the remodeled cephalic arch in patients after AFV placement. Inflow velocities ranging between 1 – 100 cm/s were tested.

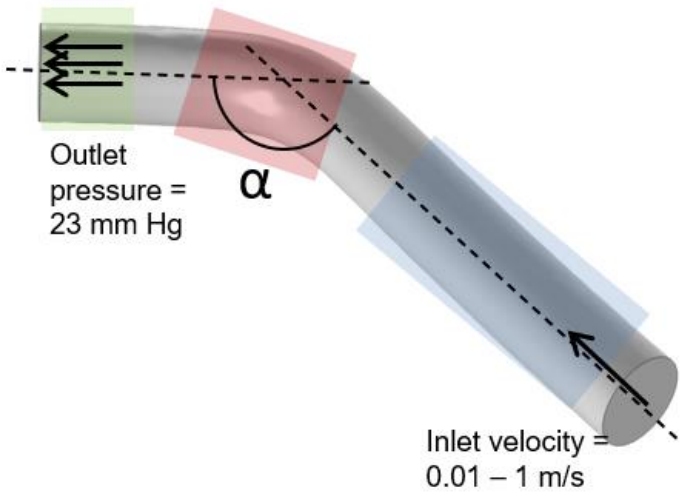

Figure 3.1: An idealized model of the a cephalic arch in ESRD patient. The diameter of the model is 9.5 mm and bend angle, α is 125°. The blue, red and green regions indicate the prebend, bend and postbend regions, respectively.

These include average flow rate measured in ESRD patients prior to AVF placement (5 cm/s) to peak flow rate measured in ESRD patients (70 cm/s) without stenosis [25]. Flow is simulated in COMSOL as both steady-state and pulsatile, using the 'Stationary' and 'Time Dependent' options, respectively. For steady-state flow, outlet pressure is set to 23 mm Hg, approximating the peak systolic pressure measured in patients' CA. Density, ρ and viscosity, η values used in the idealized model are approximated from whole blood: ρ = 1,060 kg/m^3 and η = 3.45 mPa.s [55]. 'Fully developed flow' option is selected for both inlet and outlet, along with 'no-slip boundary' condition and 'incompressible flow' options. Though whole blood is shear thinning, it has been shown previously [56] that under similar conditions, it makes no appreciable difference whether blood is modeled as Newtonian or shear-thinning fluid. We use WBV measurements in our patient cohort for fixed η in our simulations. The 'Physics' in COMSOL is described by the following equations: $\rho(\mathbf{u}\cdot\nabla)\mathbf{u} = \nabla\cdot[-\mathrm{p}\mathbf{I} + \eta(\nabla\mathbf{u} + (\nabla\mathbf{u})^T)] + \mathbf{F}$; and $\rho\nabla\cdot\mathbf{u} = 0$, where ρ is density, η is viscosity, **u** is the velocity vector, and **F** is the volume force vector, respectively. Physics-controlled meshes of coarse element sizes were generated using COMSOL.

This mesh elements of variable size that match the local topology or surface roughness of 3D model of the CA were generated. We were able to obtain mesh convergence on a few, randomly selected CA models of patients and time-points. Parallel Sparse Direct and Multi-Recursive Iterative Linear Solver (PARDISO) in COMSOL with a relative tolerance of 0.001 was used for steady state flow. For pulsatile flow, an iterative solver, Generalized Minimum Residual (GMRES) was used with a residual tolerance of 0.01.

We simulated flow in the 3D models of all five patients' CAs reconstructed from IVUS and venogram images as described above, at two time-points each. Patient-specific peak systolic velocity and whole blood viscosity measured in our previous studies were used to simulate flow in all 10 models, along with the modules and parameters described above. Flow velocity and pressure profiles for each time point were calculated as output parameters for comparison. All other parameters were set as described for the idealized CA model. Shear stress was calculated as the product of shear stress function, 'spf.sr' in COMSOL and measured WBV for all cases. We also reported the cell Reynolds number parameter defined in COMSOL, Re_{cell} using ρ and η described above, u as the local flow velocity, and L as the size of the local mesh element. $Re_{cell,}$ can be conveniently used to compare flow within a CA model, across different patient models, time-points, flow conditions, etc.

To investigate geometric and flow characteristics within each model, we demarcated the CA of each subject into 'prebend', 'bend' and 'postbend' regions and calculated the maximum velocity, pressure, and WSS from a randomly chosen 2D slice from each of these regions. Prebend was defined as the straight segment of the cephalic vein before the curve; bend was defined as the segment of the vein where it arches; postbend was defined as the straight segment of the cephalic vein before termination at the axillary vein (**Fig. 1.2**).

To simulate pulsatile flow, inlet flow velocity was applied as a sinusoidal wave to each CA reconstructed from each patient at 3 and 12 mo. time-points. For each model, the velocity amplitude was varied between peak systolic velocity, u_{max} and diastolic velocity, u_{min} at patient- and time-point specific pulse frequency, f obtained from Doppler measurements, as (u_{max}-u_{min})*sin(2πf)+u_{min}. Outlet pressure was maintained at 20 mm Hg (3 mo.) or 23 mm Hg (12 mo.). An interval of 1.5 s was simulated in steps of 0.05 s for pulsatile flow; this time ©nterval is in excess of the duration of a complete pulse cycle for all patients and time-points. Total time taken for each time-dependent simulation to complete was less than 1 hr. for all patients and time-points. All steady state simulations took < 10 min to run.

3.3 Results

3.3.1 Study Population

Five patients who completed two protocol imaging procedures, blood flow velocity and viscosity measurements at 3 and 12 mo. were included in this investigation. Patient demographics and past history were obtained from electronic medical records **(Table 3.2**).

Table 3.2: Patient characteristics

Patient ID	Age (yr)	Sex	Ethnic	Weight (kg)	Height (cm)	BMI	Diabetic	HTN	CAD	PVD
93	29	M	AA	142	167	50	+	-	-	-
96	34	F	AA	103.5	160	40.4	+	+	-	-
98	58	M	AA	99.3	175.3	32.3	+	+	-	-
104	23	M	AA	63.5	175.3	20.6	-	-	-	-
122	29	M	AA	113.4	182.9	33.9	-	-	-	-

Yr = years; F=female; M =male; AA = African American; kg = kilogram; cm = centimeter; BMI = body mass index; HTN = hypertension; CAD = coronary artery disease; PVD = peripheral vascular disease; + = yes; - = no.

A patient was considered to have coronary artery disease (CAD) if they had a myocardial infarction, or if cardiac catheterization showed significant coronary disease. A patient was considered to have peripheral vascular disease (PVD) if they had a history of amputation from ischemic disease or if vascular study showed ankle-brachial index less than 0.9. We chose all subjects with the need for a primary BCF who were receiving hemodialysis three days a week. All patients were less than 60 years of age with no history of clinical vascular disease. Peak systolic and diastolic velocities measured using Doppler, vitals, and calculated venous area, diameter, Reynolds number and arch angle are summarized in **Table 3.1.**

We noted significant changes in measured parameters local to the AVF, e.g., average vein diameter, and peak systolic and diastolic flow velocities in each patient at these two time-points, though overall blood pressure and pulse rates remained largely unchanged. There was local remodeling of the CA from the AVF maturation process, as shown by the increased mean cephalic vein diameters (0.85 ± 0.16 cm at 3 mo. to 0.87 ± 0.2 cm at 12 mo.). The mean arch angle of the CA, α, as measured from venogram images decreased slightly (137 ± 11^{o} at 3 mo. to 125 ± 17^{o} at 12 mo.), indicating that the bend may grow more acute over time [29].

Blood flow velocities downstream to the AVF were measured in the subjects using Doppler imaging. We noted significant variability in the measured peak systolic and diastolic values across subjects and time-points, highlighting the dynamic nature of flow in the CA. The average flow velocity at 3 mo. (~45.2 ± 18.2 cm/s) was significantly higher (~50%) than the average at the 12 mo. time-point (~28.9 ± 20.1 cm/s).

Using measured vein diameter, flow velocity, and whole blood viscosity values (**Table 3.1**), we calculated *Re* for each subject and time-point (**Table 3.1**). As expected, there were large variations in *Re* between subjects and time-points, with an average of 1,239 ± 530 at 3 mo. and

740 ± 709 at 12 mo. We also noted overall difference among subjects, with patient P93 experiencing relatively low *Re* at both time-points (Re_{avg} = 339) while we record much higher values for P122 (Re_{avg} = 1,566).

3.3.2 Flow Simulations in Idealized Cephalic Arch Computational Model

An idealized model of the CA was created to simulate flow under physiologic parameters associated with blood flow in patients with BCF access. Briefly, a cylindrical tube with a diameter of 0.95 cm (nominal vessel diameter in ESRD patients at QB0 = 0.3 – 0.8 cm; QB350 = 0.4 – 1.8 cm), and bent at a 125^{o} angle was used to model the CA in ESRD patients. To recapitulate blood flow in the cephalic vein which goes up the arm into the cephalic arch, we modeled flow entering through the end of the long arm of the CA model and exiting at the end of the short arm. For ease of discussion, we will call the longer arm of the model prior to the arch as 'pre-bend', the bent region as 'bend', and the shorter arm after the bend as 'post-bend'. Initial conditions for the simulation were set as follows: inlet flow velocity, *u*, was varied between 1 – 100 cm/s which includes the flow velocities in the CA of healthy adults (5-10 cm/s) and patients with AVF (QB0 = 25 – 185 cm/s, QB350 = 25 – 288 cm/s). Moreover, flow velocity (**Fig. 3.2A**) and pressure (**Fig. 3.2B**) were plotted in 3D across the length of the idealized model at *u* = 70 cm/s.

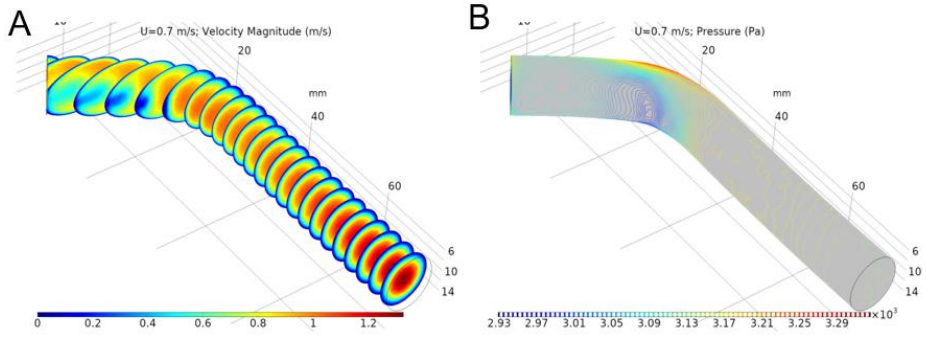

Figure 3.2: Simulated velocity (A) and pressure (B) profiles in the 3D idealized model under ESRD-specific physiological conditions.

We saw lower flow rates and lower pressures along the inner wall of the bend and correspondingly higher velocities and higher pressure along the outer wall, as indicated by the color of the velocity and pressure heatmaps. As endothelial activation is associated with areas of low WSS along the inner wall of the bend, we paid particular attention to this area as nidus for endothelial activation and clot formation.

Next, we plotted the normalized velocity profiles across the tube as function of distance from the center of the tube with the tube's center set as zero (**Figs. 3.3**).

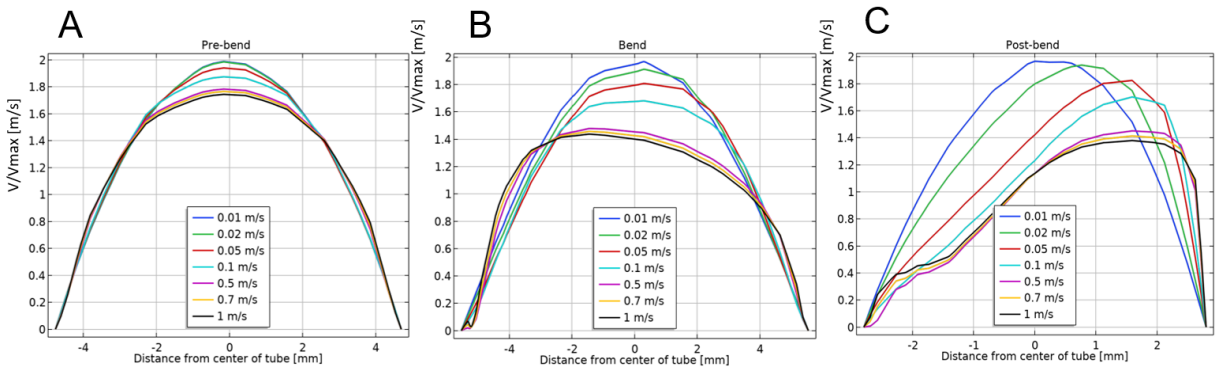

Figure 3.3: Velocity profiles across the CA model in the (A) pre-bend, (B) bend, and (C) post-bend regions in the idealized model across the tube cross-section. Different inlet flow velocities range from healthy to ESRD values.

The velocities were normalized by the maximum velocity, u_{max}, in each case for ease of comparison. This was done for three arbitrary slices chosen from the pre-bend, bend and post-bend regions. For the pre-bend region (**Fig. 3.3A**), the parabolic velocity profiles at low flow velocities (u < 10 cm/s) reflect Newtonian fluid under pipe-flow conditions [57, 58], but as u was increased to those seen in ESRD patients (u > 25 cm/s), the velocity profiles started to flatten and transition to plug-flow behavior of non-Newtonian fluids [57, 58]. This change in flow from Newtonian to shear-thinning with increasing flow velocity persisted in the 'bend' and 'post-bend' regions (**Figs. 3.3B&C**). The velocity profiles also became non-axisymmetric in the 'bend' and 'post-bend'

regions at high velocities. This is expected for flow along the bend region, as the average distance traversed by the fluid along the inner wall is less than that along the outer wall; the velocity along the outer wall has to increase to compensate for the extra distance travelled (**Fig. 3.3B**). Immediately into the post-bend region, the axial asymmetry switched direction (**Fig. 3.3C**), such that the relative velocity along the inner wall was higher than that of the outer wall. These asymmetries in velocity profile led us to predict two regions of abnormal WSS, one directly in the inner wall of the bend region, and the other at the beginning of the post-bend region, but along the outer wall of the CA. These predictions match a similar study in 2D [40].

3.3.3 Flow Simulations in Patient-Specific Cephalic Arch Models

Informed by general trends in flow characteristics obtained from simulations on the idealized models, we simulated flow in patient-specific models. Computational models of the CA at 3 and 12 mo. were used as the flow conduit. Although all subjects had primary outflow through the cephalic vein to support dialysis, we noted significant variations in anatomic geometry between patients. In a previous investigation, we measured the inlet pressure in a normal cephalic arch (without obvious stenosis) and found the average pressure to be 19.88 mm Hg at 3 mo. and 23.3 mm Hg at 12 mo. Using the patients' peak systolic velocity as the inlet velocity, WBV and average pressure measured in the CA as the outlet pressure at 3 and 12 mo., we plot the steady-state velocity (top) and pressure (bottom) profiles (**Fig. 3.4**) in the 3D models of the CA for 5 patients at 3 and 12 mo. after the AVF placement.

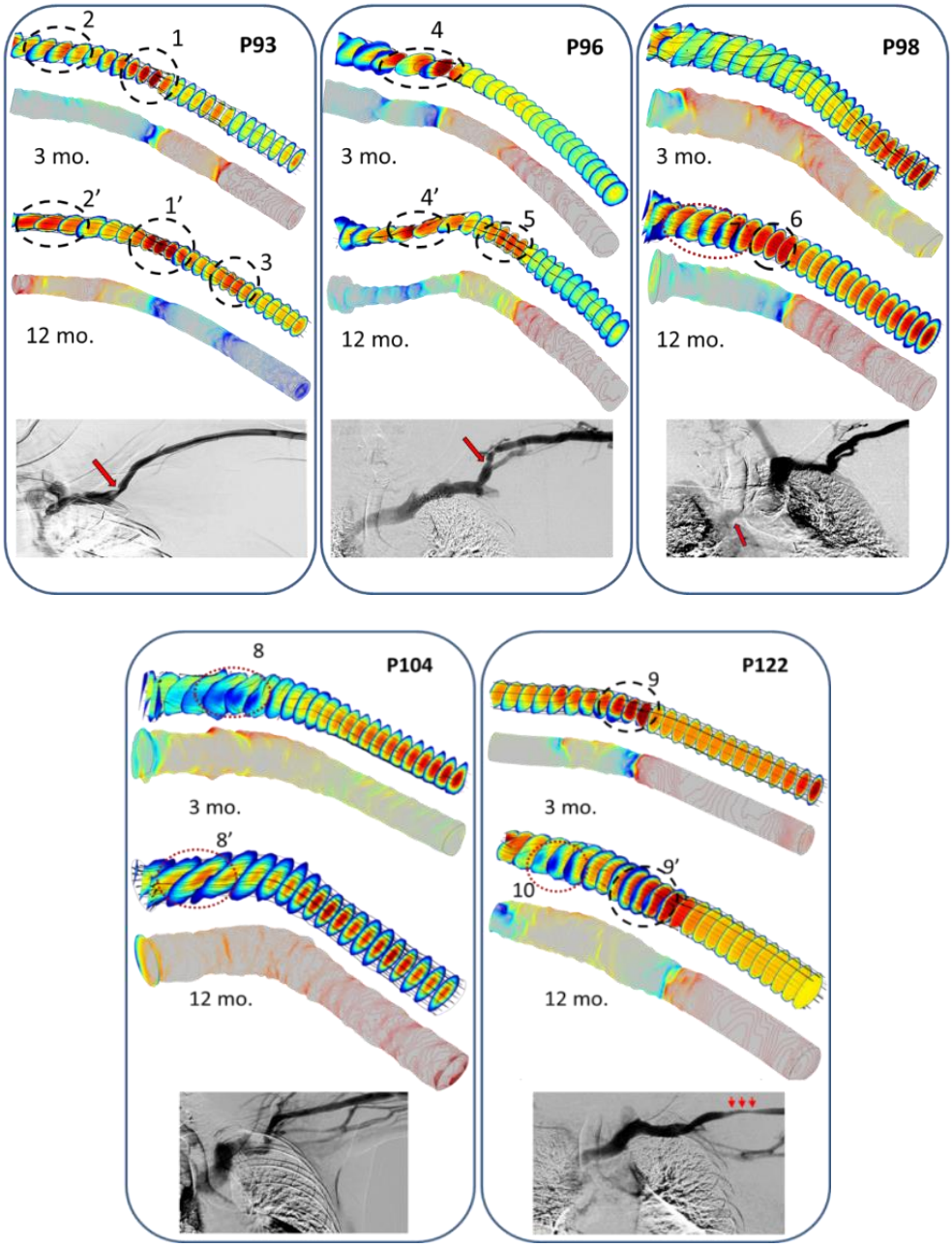

Figure 3.4: Panels P93, P96, P98, P104 and P122 show the velocity and pressure profiles in 3D models constucted from IVUS and venogram measurements on the five ESRD patients' CA at 3 mo. (top), 12 mo. (middle) and follow-up venogram (bottom) after AVF placement. The color indicates the magnitude of velocity and pressure, respectively following a rainbow scheme, with blue denoting the lowest and red the highest magnitude. Black tubes on the velocity profiles indicate the velocity field at that point with the tube diameter being proportional to the shear rate. Flow parameters obtained from each patient's vitals and Doppler data are used to simulate flow.

For all velocity and pressure profiles in **Fig. 3.4**, the color indicates the magnitude and the color bar uses a rainbow scheme with blue denoting the lowest values and red the highest. The black tubes marked on the velocity profiles in **Fig. 3.4.** indicate the velocity field at that point, with the tube diameter being proportional to the shear rate. We noted considerable variation in the velocity and pressure profiles across the 5 subjects.

Non-Newtonian flow (plug flow profile) was maintained along the bend and post-bend regions for all time-points. We observed low flow velocity and wall pressure along the inner wall of the bend in all cases (**Fig. 3.4**), which may provide possible nidi of endothelial activation that lead to stenosis and thrombosis. For each patient and time point, we identified potentially problematic areas (e.g., constrictions and low WSS) referred to as Regions Of Interest (ROIs). We circled and numbered some of them in the 3D velocity profiles in **Fig. 3.4.** We observed that ROIs that show up at 3 mo. likely persisted at the 12 mo. time-point, e.g., 1, 2 (**P93**), 4 (**P96**), 8 (**P104**), 9 (**P122**). These pre-exiting ROIs are marked as 1', 2', 4', 8', and 9', respectively in **Fig. 3.4**. Two categories of ROI were seen: the first, associated with the narrowing of the vein diameter, e.g., 1, 5, 6, 9 and the second, areas of low flow velocities at the inner bend which may be associated with abnormal wall shear stress, e.g., 2, 4, 8, 10. The black streamlines denoting the velocity vector field overlaid on the velocity profiles show that all flow are largely laminar in the pre-bend and post-bend regions under steady-state flow. Non-laminar streamlines and vortices appear in the bend regions under sufficiently high *Re* (>1,000), e.g., P96, 3 mo., P104, 3 mo. and P122, 3 and 12 mo.

Much like *Re* is used to predict global flow characteristics, Re_{cell} may be used to compare flow across the length of the CA, across different patients, flow conditions, time-points, etc. The Re_{cell} values under steady state flow are shown in **Fig. 3.5, top panel** for all subjects at all time-

points. WSS is plotted as a surface function for each model in **Fig. 3.5, bottom panel**. The values of Re_{cell} and WSS are indicated as heat maps for each figure, where red indicates high and blue indicates low values, as before.

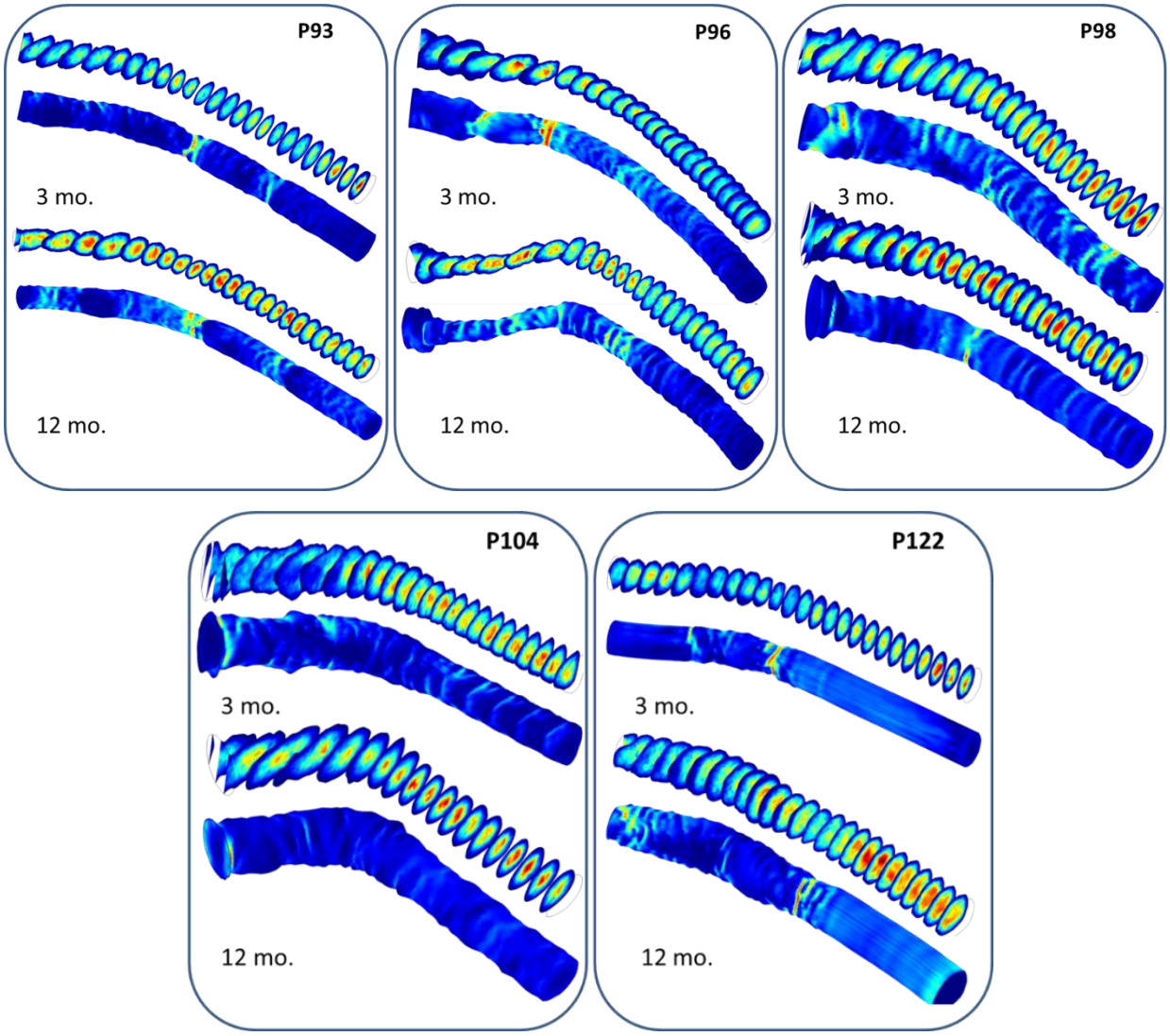

Figure 3.5: Each panel shows the Re_{cell} and WSS values in the 3D models of the five ESRD patients' CA at 3 and 12 mo. after AVF placement. The Re_{cell} and WSS values in these profiles are calculated from the velocity and pressure profiles shown in Figure 3.4. The color indicates the magnitude of Re_{cell} and WSS, respectively following a rainbow scheme, with blue denoting the lowest and red the highest values.

In all cases, Re_{cell} values were the highest at the center of the vein compared to the periphery, and increased at the bend of the CA, as expected in pipe flow. Re_{cell} values also increased in regions where the vein narrowed, compared to regions upstream or downstream of local constrictions. Higher Re_{cell} is associated with non-laminar flow and may lead to abnormal activation of endothelial cells lining the lumen. Interestingly, these regions also seemed to constrict further and develop stenosis over time (e.g., 12 mo. compared to 3 mo.). This may be due to the increasing activation of endothelial cells which activates a feedback mechanism to narrow the vein further, leading to higher velocities in the constriction and therefore, even higher Re_{cell}.

To characterize flow in CA, we calculated the average diameter, velocity, pressure, and WSS from randomly chosen slices in the 'pre-bend', 'bend' and 'post-bend' regions (**Table 3.3**). However, because of the high variability in patients' geometry and flow parameters, it was inherently difficult to estimate meaningful averages of parameters such as velocity, diameter, etc. that could be generalized across patients and time-points. Instead, we analyzed each patient individually as function of time and correlated the results from the 3 and 12 mo. models with outcome, in the form of medical follow-up and venograms taken at later times. In some cases, the medical follow-ups extended across the entire duration of the five-year study (see **Clinical Follow Up, p. 42**).

Table 3.3 Average area, diameters, velocity, WSS and pressure pre-bend, bend and post-bend regions of the cephalic arch

Patient ID: Time Point	Area pre-bend (mm^2)	Area bend (mm^2)	Area post-bend (mm^2)	Diameter pre-bend (mm)	Diameter bend (mm)	Diameter post-bend (mm)	Velocity pre-bend (m/s)	Velocity bend (m/s)	Velocity post-bend (m/s)	WSS pre-bend (Pa)	WSS bend (Pa)	WSS post-bend (Pa)	Pressure pre-bend (Pa)	Pressure bend (Pa)	Pressure post-bend (Pa)
P93: 3 months	373.6	301.8	526.1	21.8	19.6	25.9	0.22	0.33	0.29	0.72	1.22	1.41	2724.2	2677.5	2675.6
P93: 12 months	253.1	228.1	217.2	18.0	17.0	16.6	0.26	0.27	0.33	1.2	1.62	1.93	3076.5	3126.1	3138.8
P96: 3 months	271.8	215.4	270.6	18.6	16.6	18.6	0.96	1.1	1.3	2.7	6.7	8.3	3876.6	3549.8	2782.4
P96: 12 months	275.3	169.7	150.2	18.7	14.7	13.8	0.72	1.0	1	4.6	11.6	9	3732.5	3535.4	3060.8
P98: 3 months	369.9	502.8	526.9	21.7	25.3	25.9	0.76	0.5	0.5	4.0	2.2	3.9	2772.8	2808.6	2780.6
P98: 12 months	326.9	268.3	287.8	20.4	18.5	19.1	0.03	0.04	0.03	0.04	0.05	0.06	3067.4	3066.8	3066.7
P104: 3 months	281.8	357.4	275.6	18.9	21.3	18.7	0.68	0.45	0.44	2.1	6.8	3.5	2698.4	2765.3	2759.2
P104: 12 months	60.8	77.0	67.9	8.8	9.9	9.3	0.22	0.16	0.17	6.9	6	10.1	3217.1	3160.7	3154.9
P122: 3 months	306.4	295.6	426.4	19.8	19.4	23.3	0.64	0.8	0.6	2.7	6.9	2.5	2820.2	2653.3	2680.9
P122: 12 months	470.7	794.8	605.8	24.5	31.8	27.8	0.62	0.67	0.66	2.4	1.9	4.8	3345.5	3258.3	3284.5

P = patient; WSS = wall shear stress

3.3.4 Pulsatile Flow Simulations

Though blood flow in veins is not pulsatile under normal conditions, the local vein geometry and flow parameters after AVF placement get drastically remodeled over time [59, 60]. Not only do the vein diameter and blood flow velocity increase significantly, but the flow properties also change from primarily steady state to pulsatile flow [61], under the influence of the arterial flow created at the anastomosis. This is demonstrated by markedly different systolic and diastolic blood flow velocities recorded from Doppler measurements on mature AVF [62]. Interestingly, the effects of AVF maturation are not consistent among patients and strongly dependent on patient-specific physiological parameters. To simulate the effect of pulsatile flow in the idealized CA, we applied inlet flow velocity in the form of periodic waves (sinusoidal) at frequencies calculated from pulse rates measured from Doppler data.

Using pulse rates, blood pressure and peak systolic and diastolic blood flow velocities measured using Doppler, and assuming a sinusoidal flow pattern, we simulated time-dependent flow in the cephalic arch in patient P96 at 3 and 12 mo. using parameters described in **Flow Simulation Methods.** The pulse frequency (beat/min), *f* measured using Doppler is reported in **Table 3.1**. The first panel plots the inlet velocity applied on the CA for patient P96 at 3 mo. (**Fig. 3.6A**) and 12 mo. (**Fig. 3.6B**) as a function of time, and sampled during the course of a pulse beat.

A

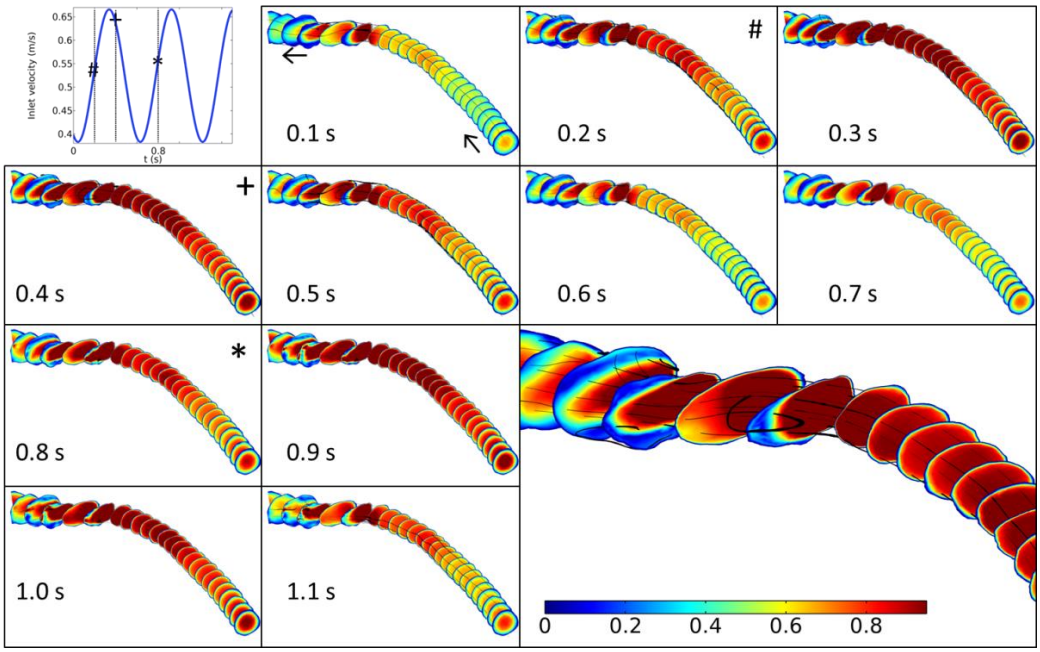

B

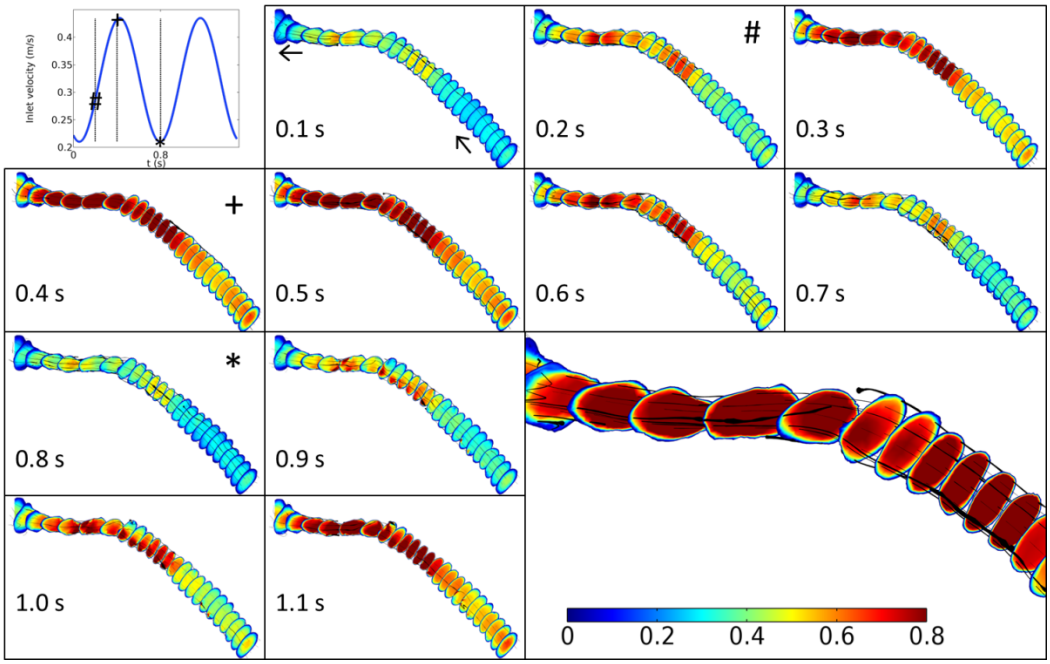

Figure 3.6: Each panel shows the velocity profile in the CA of patient P96 at 3 months (**A**) and 12 months (**B**) under pulsatile flow. In each figure, the first panel shows the inlet velocity as it cycles between peak systolic and diastolic as function of time sampled during pulsatile flow. The color bar in the last panel indicates the velocity magnitude. Black tubes marked on each velocity profile indicate the velocity field at that point with the tube diameter being proportional to the shear rate. Inlet velocities and their corresponding velocity profiles are highlighted at 0.2, 0.4 and 0.8 s, marked as '#', '+' and '*'. Arrows in the second panel indicate the direction of flow along the CA.

Subsequent panels in **Figs. 3.6** show snapshots of the 3D velocity profile in the CA for patient P96 at 3 and 12 mo. (**Figs. 3.6A**&**B,** respectively) as the amplitude changes over the period of an oscillation. As before, the color bar shown in the last panel of each figure indicates the velocity magnitude in m/s and ranges from blue (lowest) to red (highest). The black tubes marked on the velocity profiles indicate the velocity field with the tube diameter indicating the shear rate at that point. In both **Figs. 3.6A**&**B**, we marked three time-points- 0.2, 0.4 and 0.8 s as '#', '+', and '*' in the first panel to show the inlet velocity applied to the CA and the corresponding 3D velocity profiles generated periodically in the CA for those inlet velocities during a pulse-beat. We noted that the areas of high velocity and low WSS seen at the bend at the 3 mo. time-point under steady state conditions (**Figs. 3.4 and 3.5, panels P96**) were recapitulated under pulsatile conditions at peak systolic values. As the inlet velocity, *u* increased, this area of high velocity was seen to spread both upstream and downstream as function of *u* and then dissipated in a periodic fashion for every pulse, as *u* was varied between peak systolic and diastolic. As the peak systolic velocity, u = 0.67 m/s at WBV = 2.96 mPa.s (Re = 1,574) was reached at ~4 s (marked as '+' in **Fig. 3.6A**), we observed the periodic formation of a vortex at the bend of the CA, as shown by the black streamlines of the velocity field in a close-up of the bend in the last panel. The vortex dissipated as *u* decreased to the diastolic value. Deviations from non-laminar flow, vortices, etc. during pulsatile flow indicate that transient turbulent conditions may be generated in the CA during pulsatile flow that may lead to aberrant WSS and endothelial cell activation at high *u*.

We saw similar trends in P96 under pulsatile flow for the 12-month time-point too: as the inlet velocity increased, the two areas at the constrictions (marked as 4' and 5 in **Fig. 3.4, panel P96**) showed the most dramatic increase in velocity. The region between the constrictions also experienced marked increase in velocity as function of *u* which then dissipated in a periodic

fashion for every pulse, compared to the pre- and post-bend regions. Note that however, at comparatively modest u = 0.44 m/s and WBV = 4.08 mPa.s at 12 mo. (Re = 746), we do not see any vortex formation in the velocity vector field at the bend in the patient's CA at peak u (**Fig. 3.6B,** last panel, close-up of the bend), unlike at 3 mo.

Similar 3D velocity profiles in the CA of patients P93 and P122 are shown as functions of time under pulsatile flow in **Figs. 3.7** (P93) and **3.8** (P122) at 3 mo. (**A**) and 12 mo. (**B**), respectively.

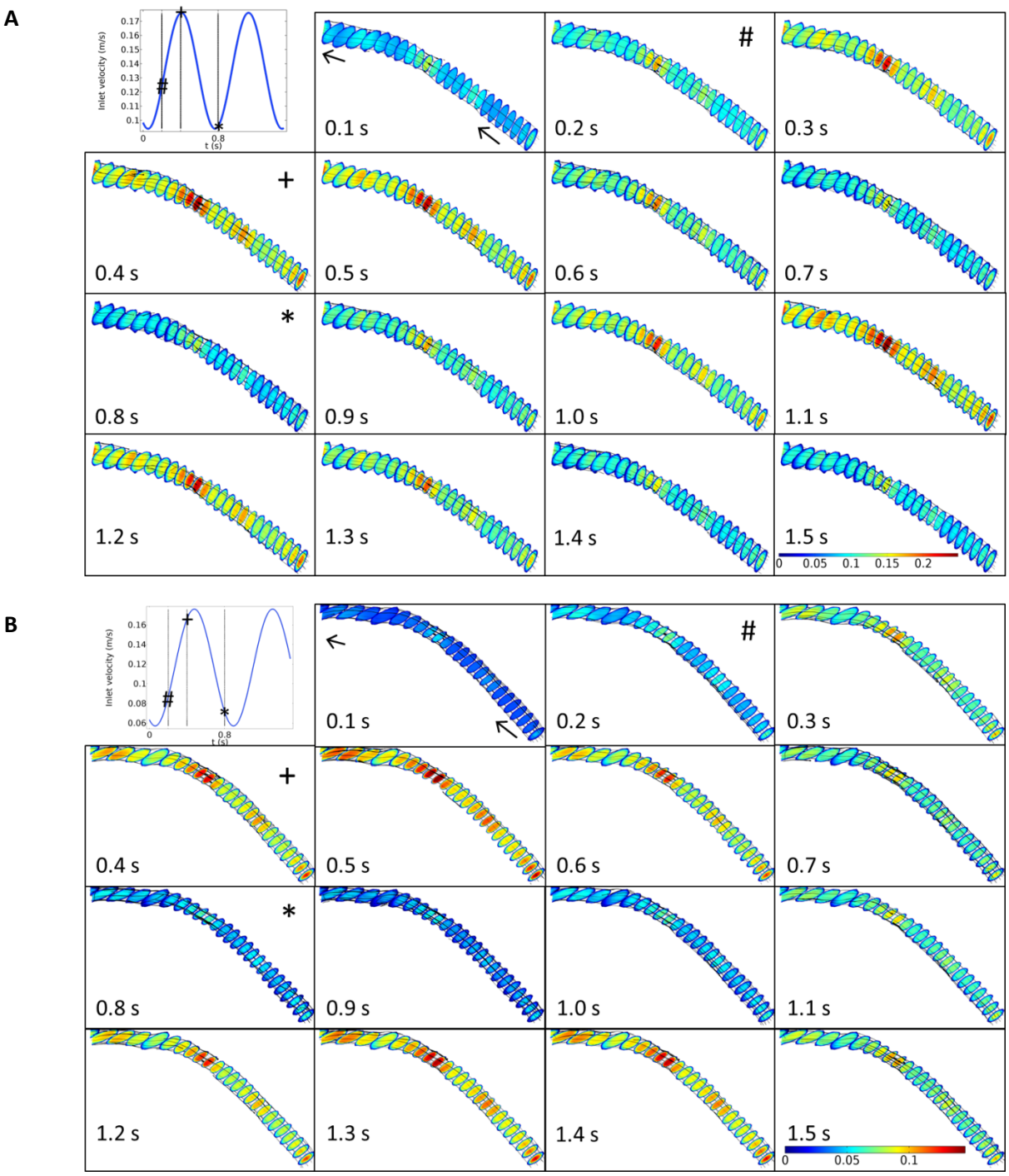

Figure 3.7: The velocity profile in the CA of patient P93 at (**A**) 3 months and (**B**) 12 months under pulsatile flow are shown at different times as indicated. The first panel in each figure shows the inlet velocity as it increases (systolic) and decreases (diastolic) as function of time. Inlet velocities and their corresponding velocity profiles are marked as '#', '+' and '*' at three time-points, 0.2, 0.4 and 0.8 s. The color bar in the last panel indicates the lowest velocity in blue and the highest in red. Arrows in the second panel indicate the direction of flow along the CA.

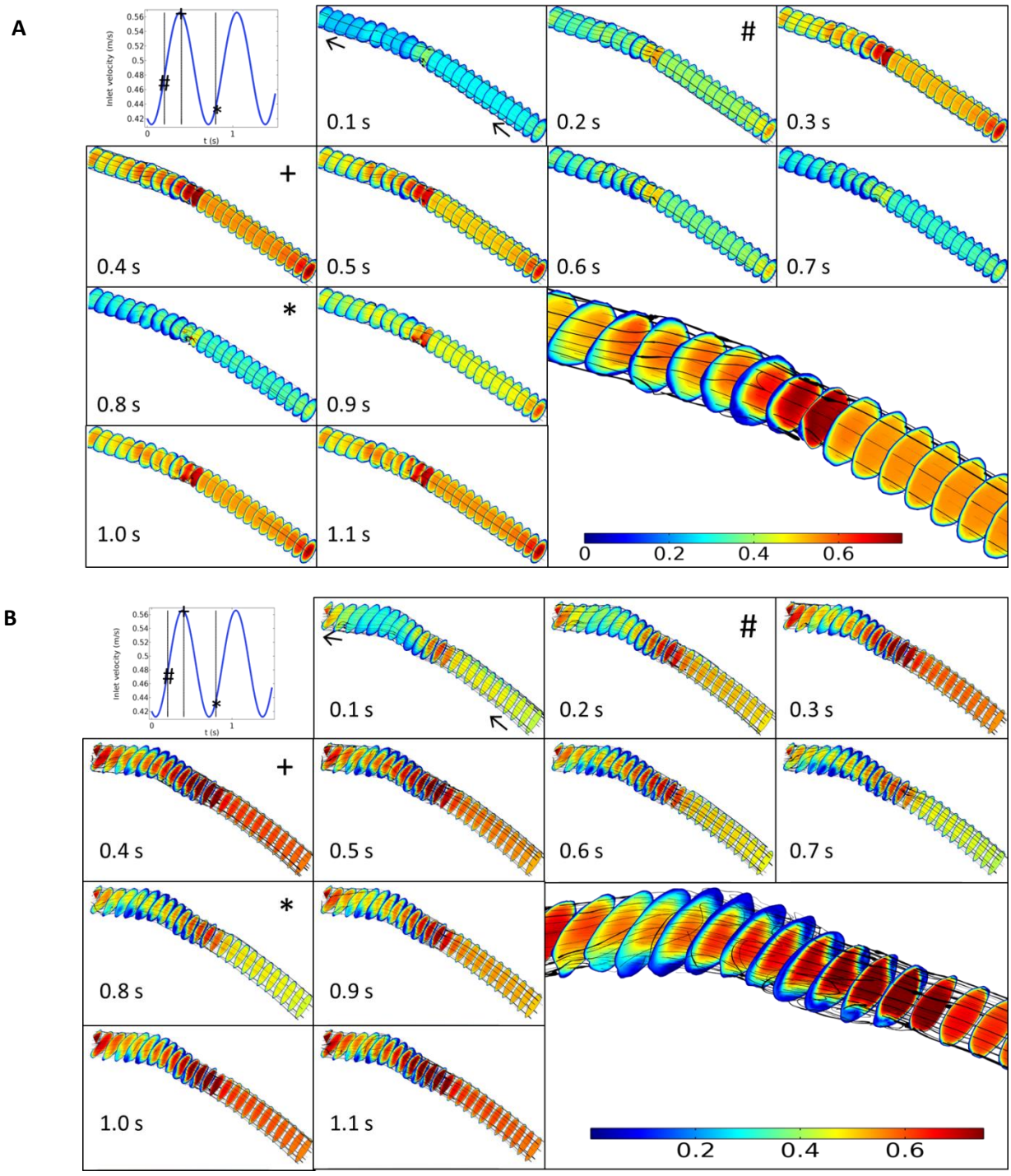

Figure 3.8: The velocity profiles in the CA of patient P122 at (**A**) 3 mo., and (**B**) 12 mo. under pulsatile flow are shown at different time-points. The first panel shows the inlet velocity as it increases (systolic) and decreases (diastolic) as function of time. Inlet velocities and their corresponding velocity profiles are highlighted at three time-points, 0.2, 0.4 and 0.8 s, marked as '#', '+' and '*'. The color bar in the last panel indicates the lowest velocity in blue and the highest in red. Arrows in the second panel indicate the direction of flow along the CA.

At overall low *u* and high WBV, patient P93 showed largely laminar streamlines and moderate flow irregularities (*Re* = 367, 311, respectively) at both 3 mo. (**Fig. 3.7A**) and 12 mo. (**Fig. 3.7B**) under sinusoidal flow. A constriction in the CA at the bend at 3 mo. developed slightly both upstream and downstream at 12 mo., causing moderate increase in flow velocities and shear rates in these regions. No vortex formations were noted in the velocity streamlines in the CA bend of P93 at the 3 mo. or 12 mo. time-points.

In contrast, patient P122, who had a constriction at the CA bend and also recorded high *u* and high WBV at 3 mo. (*Re* = 1,180; **Fig. 3.8A**) and 12 mo. (*Re* = 1,952; see last panel in **Fig. 3.8B**) underwent considerable remodeling of the cephalic arch geometry between the 3 and 12 mo. time-points. P122 also showed high flow velocities with non-laminar streamlines in the bend region of the CA.

While the flow velocities in the CA from Doppler data can be well approximated as sinusoidal in most cases, we also modeled flow in the CA of patient P96 (3 mo.) as the periodic variation in inlet velocity as non-sinusoidal waveforms: square (**Fig. 3.9A&B**, with duty cycle = 0.2 and 0.5, respectively) or saw-tooth (Supplementary **Fig. 3.9C**).

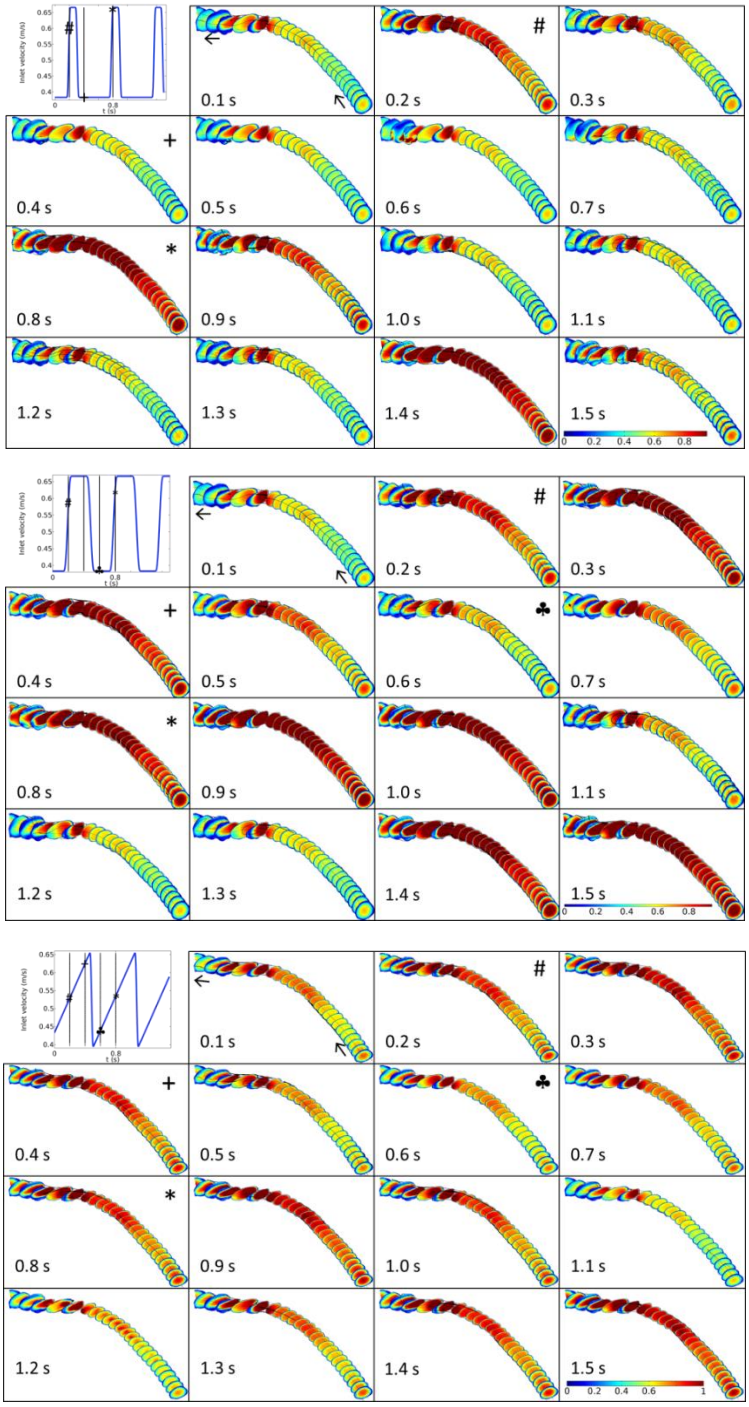

Figure 3.9: The velocity profile in the CA of patient P96 at 3 months under pulsatile flow. Each subfigure shows the inlet velocity applied as (**A**) a square wave with duty cycle = 0.5, (**B**) square wave with duty cycle = 0.2, and (**C**) a saw-tooth wave. As before, the first panel shows the inlet velocity as it increases (systolic) and decreases (diastolic) as function of time. Inlet velocities and their corresponding velocity profiles are highlighted at three time-points, 0.2, 0.4 and 0.8 s, marked as '#', '+' and '*'. The color bar in the last panel indicates the lowest velocity in blue and the highest in red. Arrows in the second panel indicate the direction of flow along the CA.

The duty cycle indicates the fraction of one period in which the inlet velocity in maintained at peak systolic velocity. For example, at a duty cycle of 0.5, the flow velocities experience the peak systolic value for 50% of the time during a pulse beat. In contrast, at duty cycle = 0.2, the CA experiences peak systolic velocity for only 20% of the pulse duration. By changing the duty-cycle parameter, we were able to investigate the effect of longer dwell times at the peak systolic values may have on flow in the CA.

In all cases, the consequences of pulsatile flow were seen to broadly hold true across patients (e.g., P96, P122) where, at high *Re,* the velocity streamlines transition from laminar to non-laminar flow and back in the CA bend as *u* varies between systolic and diastolic values. We posit that second-order effects, e.g., the time taken to transition between the peak systolic and diastolic values, may also influence non-linear flow behavior in the CA, leading to further abnormal endothelial cell activation.

3.3.5 Clinical Follow Up

The cohort exhibited outcomes ranging from patients having success with continued AVF use, to patients with recurrent thrombosis, cephalic arch stenosis, or steal syndrome. **Fig. 3.4, bottom, in each panel** shows the follow up venograms taken between 21-60 months after AVF placement with correlation. The details of the heterogeneity in patients as the clinical follow up are provided. Our study highlights the variety of outcomes in each case (**Table 3.4**) that may be traced back to patient-specific modeling.

Table 3.4: Clinical outcomes of patients

Patient ID	CAS	AVF Loss	Other
93	+	+	Recurrent thrombosis, stenosis of anastomosis, venous outflow and central veins
96	+	-	Recurrent stenosis, aneurisms
98	-	-	Central venous stenosis
104	-	-	Dual flow basilic and cephalic veins with aneurisms required surgical resection
122	+	+	Venous outflow stenosis and steal syndrome required AVF ligation

CAS = cephalic arch stenosis; AVF = arterial venous fistula ; + = yes; - = no.

Recurrent venous stenosis and thrombosis of the AVF occurred in subject P93 requiring numerous interventional procedures to maintain fistula patency. At 48 months after AVF placement, a venogram was done for thrombosis and showed CAS was evident as shown by the red arrow in (**Fig. 3.4, P93, bottom panel)** correlated with areas of high velocity both at 3 months **(2)** and 12 months **(2')** **(Fig. 3.4, P93, top and middle panels).** P93 eventually developed severe central venous stenosis in the brachiocephalic vein and juxta-arterial anastomotic stenosis, requiring angioplasty and stent placement (not shown). The patient eventually lost patency of the BCF and needed catheter access and a new AVF in the opposite arm.

At 21 months, high venous pressures were recorded in P96 during hemodialysis with pseudo-aneurysms at the cannulation areas. Venogram imaging showed that the patient had developed venous outflow stenosis and CAS (not shown). At 36 months there was evidence of significant CAS at the bend of the arch (**Fig. 3.4**, P96 bottom panel) which corresponded to the abnormal high flow profiles (**4** and **4'**). (**Fig. 3.4, P96, top and middle panels**).

P98 required a follow up venogram at 60 months for swelling of the arm. The venogram showed stenosis at the junction of the brachiocephalic vein and superior vena cava, indicated by

the red arrow (**Fig. 3.4, P98, bottom panel**) with retrograde flow up the internal jugular vein and small axillary collateral. The flow and pressure profiles at three months do not show high flow and pressure. The 12-month velocity profile is high (**6** and **7**) which correlates anatomically with collaterals evident on the follow up venogram.

P104 developed dual flow through the cephalic and basilic vein systems with most flow going through the basilic system. A vascular lab study at month 28 showed a volumetric flow of 3,336 ml/min in the basilic vein and a volumetric flow of 686 ml/min in the cephalic vein. This process of flow diversion (cephalic vein to basilic vein) may have been evident as early as 12 months after AVF, as shown by the low peak systolic velocity (**Table 3.1**). The patient subsequently developed a very large aneurysm of the basilic vein which required a basilic vein ligation and aneurysm resection. The high flow velocities at 3 and 12 months (**Fig. 3.4, P104, 8** and **8'**) correlate with a collateral vein imaged at the later time point.

CAS developed in P122, as shown by the red arrows, was first observed at 24 months (**Fig. 3.4, P122, bottom panel)** which correlated in location to high flow velocities at 3 months (**9**) and 12 months (**9'**). P122 also developed significant venous outflow stenosis which required angioplasty and later went on to develop a severe steal syndrome which resulted in AVF abandonment. The clinical outcomes and follow up above are also summarized in **Table 3.4**.

3.4 Discussion

While computational modeling has been constructed from IVUS images in coronary lesions [63] and used to determine WSS at the anastamotic angle in AVF [38], it has not been used to look at the effect of the AVF on flow downstream. Because of the unique geometry and dynamic remodeling of the CA as a direct consequence of the AVF placement, the CA can be an area of pathological and interventional relevance in context of ESRD and hemodialysis. This is the first

reported computational fluid dynamics simulation on a series of human patients with AVF access studied over time.

Using 3D computational modeling, we showed that abnormal hemodynamics, specifically high flow velocity in the CA, predicted areas that develop into stenosis or have abnormal collateral vessel formation. To test the effect of fluid flow in a simplified CA and decouple the effects of local vein topology/surface roughness and stenosis from vein diameter and flow velocities, we simulated blood flow in a 3D idealized vein model with dimensions similar to the CA in ESRD patients under hemodialysis. We observed that when the velocity increased from healthy values to the numbers measured in ESRD patients, the velocity profile across the vein cross-section changed from Newtonian to non-Newtonian. At the bend, the asymmetry in the velocity profile across the vein cross-section, with flow velocities higher along the outer wall and lower close to the inner wall. In the post-bend region, the idealized model again showed asymmetry in velocity profiles but with flow velocities higher along the inner wall and lower along the outer wall. These findings identified some general trends to investigate in patient-specific 3D models of the CA. The idealized CA model shown in **Fig. 3.1** with its smooth surface and uniform diameter lacks the intricate topographic changes found in the individualized models which greatly affect the hemodynamics.

Conventional angiography remains the main imaging modality used for vascular imaging. Traditionally, AVF complications have been diagnosed and treated with endovascular techniques most commonly by percutaneous angiography techniques which yield 2D images of the vessel of interest. As shown in our study, IVUS adds valuable information about the actual vessel's cross-sectional area showing areas of hemodynamic turbulence and venous stenosis that may not be otherwise appreciated from 2D venograms.

3D modeling of the CA was performed on five subjects at two time points: one at 3 mo. that represent a mature AVF, and another at 12 mo. at which restoration of WSS should occur [64]. The remodeling response in the vein after AVF creation should be greatest in the first 2-6 weeks, during which maturation is achieved. Beyond this time, the vein is found to be less "shear responsive" and adapted to the new flow environment, given venous stenosis does not occur [46]. Our 3D models suggest that the CA is an area of active remodeling beyond 3 mo., there being significant differences between the 3 and 12 mo. models for all 5 patients in our study. In fact, follow-up venograms of the CA (as late as 60 months from AVF placement) suggest that the CA continues to remodel over time.

Using baseline blood flow velocities measured in the patient cohort using Doppler, we identified areas of abnormal blood flow in our models at 3 and 12 mo. such as high velocity and low WSS. Correlating these areas between the two time-points and follow-up venograms taken at later times for the patients and outcome, we find that some areas of abnormal flow that show up as early as 3 mo. are seen to persist at 12 mo. and can be associated with stenosis. In addition, the areas of low WSS and high pressure at 3 and 12 mos. are predictive of venous stenosis. We show the venous bends of the arch have anisotropic (Low) velocity along the inner bend, low WSS and high pressure. In a blood vessel, velocity of blood flow increases after a constriction or venous stenosis. The velocity and diameter in our study may not show a relationship because of both upstream (central vein) and downstream (anastomotic) stenosis.

Patients are subject to further increase in blood flow during hemodialysis three times a week that is estimated to be 18% above the AVF baseline blood flow [65]. Elevated velocities during dialysis lead to increased *Re* and create turbulent conditions in the CA, affecting the endothelium and worsening the stenosis. High blood flow is prescribed during hemodialysis to

shorten treatment session duration and maximize solute clearance, but may put the AVF at risk for adverse outcomes due to altered hemodynamics [66]. The optimal blood flow during hemodialysis that can maintain adequate clearance without contributing to AVF failure is not known and warrants further investigation.

There are some limitations to our study which include a descriptive study in a small cohort of patients lacking racial diversity; the subjects were mostly males who were doing well without additional co-morbid conditions. None of the subjects required hospitalization during the study, and attended most hemodialysis sessions. Another limitation is that the current IVUS data were obtained only from the CA, as this was the area of interest at the time under investigation; we do not have images of the anastomosis and central veins for this cohort, which could further influence flow velocity and resultant hemodynamics. There are subtle changes in the CA such as constrictions which alter the hemodynamics and endothelial activation. There are also additional vessels known as collaterals (evident in venograms) that can divert flow away from the CA which affect the hemodynamics but are not accounted for in our model. Finally, and perhaps most importantly, our models did not account for the effect of biochemical properties on the system, such as: 1) interplay between the blood components, 2) endothelium, 3) the coagulation cascade, and 4) inflammatory response from the abnormal flow in the CA. Biochemical factors and cellular remodeling are also important in understanding and preventing complications and AVF failure and thus worthy of further investigation.

3.5 Conclusions

In summary, we have shown a systematic approach to exploring complications in individual ESRD patients under hemodialysis that was never been attempted before to construct a computational model of the cephalic arch using IVUS and 2D venograms. We emphasize the

importance of the CA geometry and abnormal hemodynamics, particularly in the bend, that make the CA downstream to an AVF a unique area for study. Our modeling shows that the signals for failure may come along early (3 mo.) and if left untreated, can become serious. Through systematic alterations of geometric or flow parameters, this modeling technique may also be used to prevent flow conditions that deviate from steady laminar flow which contribute to CA endothelial dysfunction. These computational models lay the foundation for a study to determine and optimize the flow and pressure parameters which could prevent altered hemodynamics that cause AVF complications and failure. Velocity and pressure could be optimized at the anastomosis by external devices such as Optiflow [66] and VasQ [67] or internal devices such as stents [68] which are designed to minimize flow disturbances with detrimental consequences on the CA. Computational modeling shows that hemodynamics may be able to predict clinical sequela, but this will not provide the whole picture. The endothelium and blood components are also important which need to be integrated into a model of the cephalic arch. Future studies will include prospective imaging with computational modeling on a greater number of subjects with statistical tests of the prognostic performance.

.

Chapter 4

Fabricating patient-specific cephalic vein arch millifluidic devices

4.1 Introduction

We detail the fabrication of transparent elastomer-based millifluidic models *in vitro* that capture actual patient-specific dimensions, overall geometry and local topography of their venous cephalic arches as areas of clinical follow-up. We validate the fidelity of our design and fabrication workflow using IVUS and optical measurement on such an elastomeric device prototype. We then build six fluidic devices, including two idealized 'physiologic' and 'pathologic' models and four devices that recreate the cephalic arches of 2 hemodialysis patients at 2 time-points from IVUS and venogram data. All six models are perfused with a transparent, engineered fluid matching the viscosity and density of blood and containing trace amounts of fluorescent microbeads under steady-state physiological conditions and imaged extensively to characterize flow in each device. Briefly, the tracer beads are imaged under epifluorescence and images of the microbeads under flow are acquired in time-series on each device's cephalic arch or 'bend', along with areas upstream (prebend) and downstream (postbend) to the bend. We also developed image analysis software to extract the velocity and WSS of the fluorescent tracer beads from the imaged streamlines.

Although the current study details the geometry-hemodynamics interplay under physiologic flow parameters and is unable to implement pathologic flow rates or pulsatile waveforms, these models enable a comprehensive study of thrombosis under pathologic flow upon further optimization. The aspiration is that the geometry and hemodynamics in the fluidic model matching the patient-specific abnormal flow conditions will help tease out the variability in thrombosis risk and outcome between patients. Our technology shows promise for systematic isolation and analysis of vein geometry, flow parameters, blood constituents, and endothelial cell activation. All factors play a critical role in the nucleation and propagation of thrombosis in an AVF. Therefore, these factors are worth studying, both individually and collectively, to help develop personalized care in dialysis that improves that quality of life for ESRD patients.

4.2 Materials and Methods

4.2.1 Device Fabrication

Two time point-specific 3D models of the patient's cephalic arch (P96 and P104) were reconstructed from IVUS and venogram of the cephalic arch taken 3 and 12 months (mo.) after AVF placement [44]. The physiologic and pathologic models were created in AutoCAD with an average diameter of 3 mm (physiologic) and 6 mm (pathologic) and bend angle of 125°. Importantly, the physiologic cephalic arch is much smaller than the (enlarged) pathological and patient-specific geometries presented in this study. Significant and continuous dilation of the cephalic vein in patients accompany cephalic arch remodeling after AVF placement and over time to be able to adapt and withstand high flow rates and pulsatile flow transmitted through the AVF from the bypass artery; these abnormal flow patterns transmitted into the cephalic arch through the AVF can dominate the steady-state, low-velocity flow seen under physiological conditions. We doubled the cephalic arch diameter to capture this vein dilation in the pathologic model.

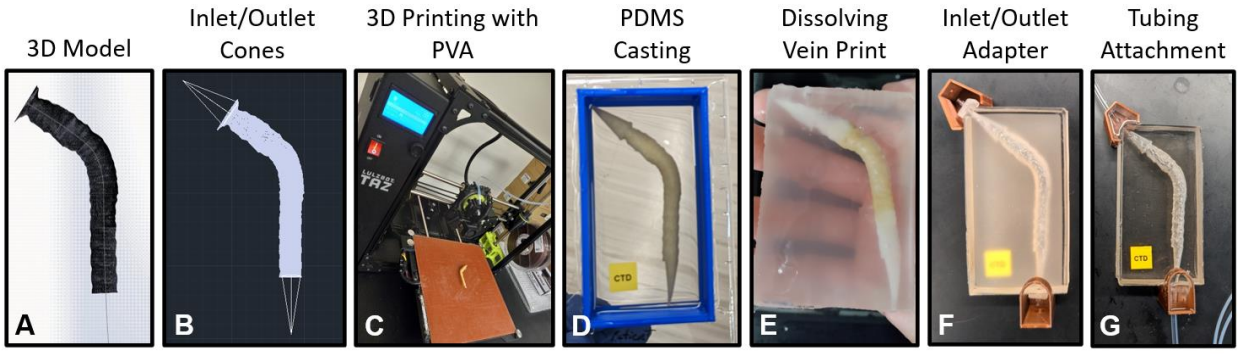

Figure 4.1: Fabrication of cephalic arch millifluidic devices. (A) Patient computational cephalic arch model. (B) Inlet/outlet cones addition to computational model to make flow setup tubing compatible with fabricated millifluidic device inlet/outlet dimensions. (C) Computational model 3D printing with water-soluble PVA filament by material extrusion 3D printer. (D) Post-PDMS casting, the cephalic arch 3D print is encased in a PDMS block. (E) Inlet/outlet holes are made in the PDMS blocks and these are submerged in water and autoclaved to dissolve until 3D print is completely dissolved. (F) Inlet/outlet adapters are incorporated to connect the millifluidic device to the flow setup and circuit. (G) Tubing is attach to connect it to fluid reservoirs in order to perform flow experiments and record them via epifluorescence microscopy.

Each model (**Fig. 4.1A**) was imported into AutoCAD and two cones, each 2 cm in height, were added to the two ends of each model to help stabilize the flow at the junctions between the vein model and the flow system (**Fig. 4.1B**). Additionally, a box-like mold was designed to ease fabrication of the millifluidic devices. The vein and box mold were exported as a .stl file and imported to Cura LulzBot Edition 3.2.21 software. 3D printing parameters were set to 0.38 mm (maximum) resolution, printing temperature of 210°C, with densities of 100% and 10% for the print and support, respectively. After adjusting the Print Setup, the file was exported as a GCode File (*.gcode) and transferred to the Taz4 3D printer (#LUKTPR0041NA, B&H Photo) using a water-soluble, polyvinyl alcohol (PVA; #PVA300N05, eSUN), filament (**Fig. 4.1C**).

Once the device and box mold were printed, the box mold was glued to a 150 mm x 15 mm polystyrene Petri dish (Sigma) with a hot glue gun. Polydimethylsiloxane (PDMS; Catalog # 4019862, Dow Sylgard 184) was mixed at 1:10 (cross-linker: base) ratio and poured on the inside of the box mold to form an initial thin layer. Air bubbles trapped within the PDMS mix were

removed by placing the Petri dish in a vacuum desiccator for 30 min before curing at 65°C for 2 hr. Subsequently, the 3D printed vein model was cleaned to remove all support filament and placed on top of the cured PDMS layer. Another PDMS layer was poured on the box and cured, covering half the height of the vein print. Upon vacuuming and curing, a final PDMS layer was poured and cured to completely cover the vein print. This resulted in a PDMS block with 3D printed vein embedded (**Fig. 4.1D**). The surrounding 3D printed box mold was removed by cutting out the PDMS block with a scalpel.

A 1 mm biopsy punch was used to cut into the PDMS to access the tips of the inlet and outlet cones. The device was immersed in DI water and autoclaved in a B4000-16 BioClave Research Autoclave (Benchmark Scientific) 4-5 times at 134 ^{o}C, 30 psi until the PVA printed models within the solidified PDMS block were dissolved (**Fig. 4.1E)**. Once dissolved, a cavity that recapitulates the patient-specific vein geometry (as reconstructed by us from IVUS and venogram data) remained inside the PDMS device. The millifluidic device was submerged in boiling water and wiped rapidly to remove any PVA particulate adsorbed onto the device surface. Unless removed, the PVA particulate coating makes PDMS surfaces significantly cloudy, which can deteriorate quality of fluorescent images of the device.

Since relatively high flow rates are necessary to mimic physiologic flow of the cephalic arch, it is critical that leakage-free connections between the fluid reservoirs and millifluidic devices are established. Given that our fluid reservoirs have tubing ports compatible with 1/16” outer diameter (OD), 1/32” inner diameter (ID) PEEK tubing and our millifluidic devices have inlet/outlet ports compatible with 1/16" ID, 1/8" OD Tygon PVC clear tubing (#6516T11, McMaster Carr), a cuffed tube-tube connection adapter was made to couple tubing. To achieve this, the ring portion of 8-gauge AWG crimp ring terminal connectors (#IGCRT8-10, Amazon)

were cut with a sheet metal cutter (#DWHT14675, Amazon) in order to obtain a cast-able cylindrical mold. Around 4 cm of the PEEK tubing was inserted into the Tygon tubing. A rubber sleeve was positioned to tightly cover the PEEK tubing-Tygon tubing connection placed in the center of the mold. The bottom of the cylindrical mold was then sealed with Parafilm M wrapping film (#S37440, Fisher) to keep tubing components in place. The PEEK tubing-Tygon tubing junction was positioned vertically such that both tubing ends were coaxially aligned relative to the cylindrical mold. Low-viscosity epoxy resin (#4336899262, Amazon) was poured into the cylindrical mold to encase the tubing junction. The resin was allowed to cure at room temperature for at least 24 hr. to ensure that any potential leaks in the tubing junction were sealed (**Fig. 4.2A**).

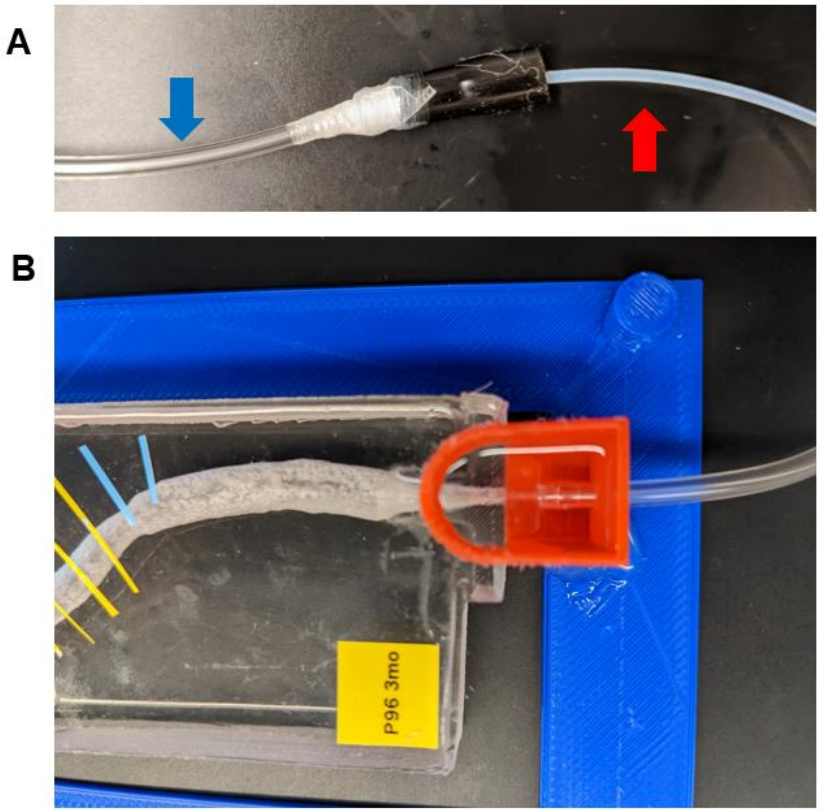

Figure 4.2: Tubing connections and inlet/outlet setup: (A) Tubing-tubing junction showing the different tubing diameters and materials. Tygon tubing (indicated by blue arrow) is connected to the millifluidic device while PEEK tubing (indicated by red arrow) is coupled to the BMF reservoirs. (B) Inlet adapter

To stabilize the junction between the millifluidic device and the coupled tubing adapter, two small 3D-printed box molds were used to cast PDMS (**Fig. 4.2B**). Plastic barbed tube fittings (3/32" OD x 1/16" ID, #5117K41, McMaster-Carr) were plugged into both the inlet and outlet of all devices (**Fig. 4.1F**). The smaller box molds were aligned with the device inlet and outlet and affixed to the device using a hot glue gun. The Tygon-tubing end of the tubing adapter was connected to the barbed fitting at the device inlet through a hole in the small box mold; the outlet tubing was similarly attached to the barbed fitting on the device outlet. Finally, PDMS (1:10 crosslink/elastomer) was cast and cured on the small box molds to seal the junctions. The inlet tubing was connected to the fluid reservoir; the pressure-driven flow control system also connected to the fluid reservoir and drove unidirectional flow in the millifluidic devices (**Fig. 4.1G**). The outlet tubing was allowed to drain out at atmospheric pressure. Six fluidic devices were fabricated: physiologic, pathologic, patient P96 imaged 3 (P96, 3 mo.) and 12 months (P96, 12 mo.) after AVF placement, and patient P104 also imaged 3 (P104, 3 mo.) and 12 months (P104, 12 mo.) after AVF placement. All fabricated devices are displayed in **Fig. 4.3A-F**, along with their average vein 'lumen' diameters.

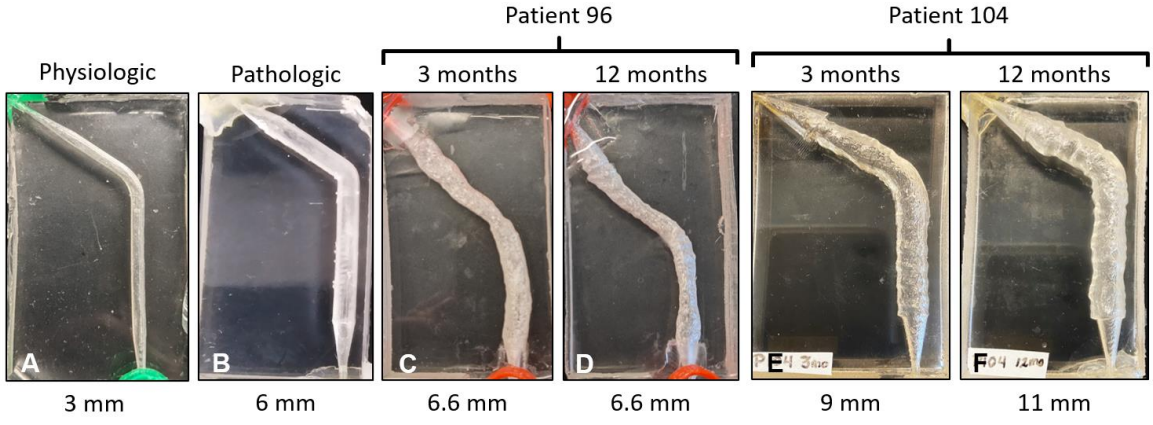

Figure 4.3: Fabricated cephalic arch millifluidic devices and respective average vein diameters (mm) capturing physiologic (A), pathologic (B) and patient-specific geometries at 3 and 12 months post-AVF creation (C-F).

A ‘phantom’ device, based on a patient (P98, 3 mo., average vein diameter = 8.5 mm) chosen at random, was created for geometric validation of our device fabrication method (**Fig. 4.4A**), to check if the internal cavity geometry of fabricated ‘phantom’ matched the geometry of the computational model it was based on. The inlet/outlet ports were simplified in the phantom model since flow was not necessary to image the internal cavity of the device**.**

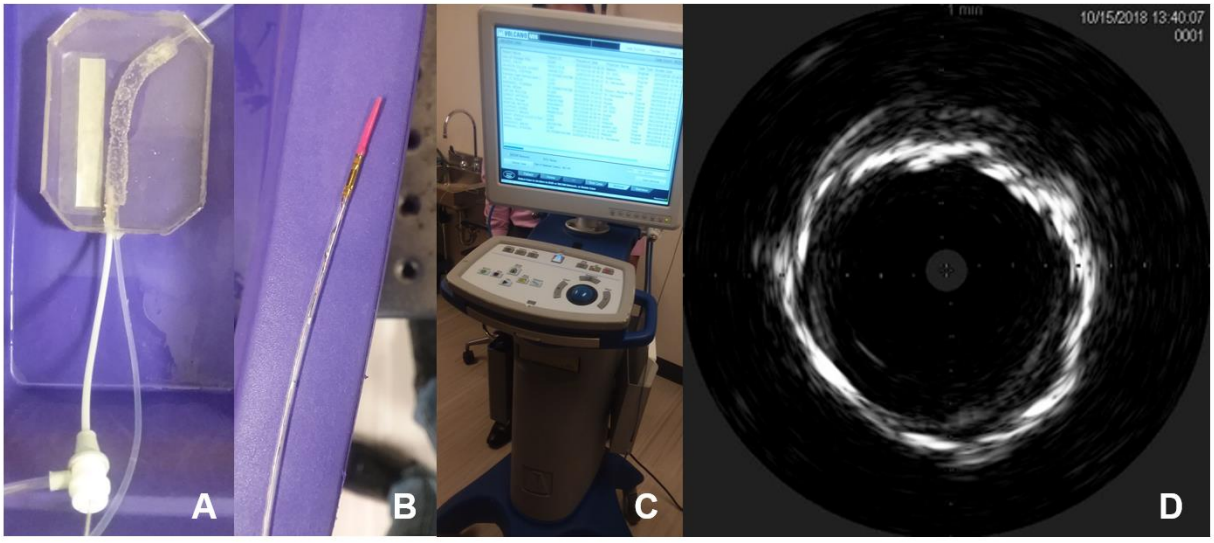

Figure 4.4: Validation equipment and phantom model imaging (A) Phantom model of the cephalic arch canulated with IVUS transducer catheter. (B) IVUS catheter. (C) Portable IVUS imaging console. (D) IVUS image obtained from the phantom model flushed with 1X PBS.

4.2.2 Validating Device Fidelity in Recapitulating Cephalic Arch Geometry

To confirm that the internal vein geometry of our millifluidic devices match the geometry of the computational models they are based on, we performed IVUS on the millifluidic phantom device, henceforth referred to as the ‘phantom’, to generate 3D computational models constructed from each IVUS pullback imaging performed on the phantom device that could be used for

geometric comparison. This process was followed to test consistency of IVUS imaging across different trials, as well as for fidelity of our 3D modeling and device fabrication processes in recapitulating vein geometry. We reasoned that if our phantom millifluidic model were faithful to the IVUS images, then the models reconstructed from different rounds of IVUS imaging of the said device would match each other, as well as the original model used to fabricate the millifluidic device in the first place.

The millifluidic phantom device (**Fig. 4.4A**) was filled with 1x phosphate buffered saline (PBS), punctured using a 21G micro-puncture needle and a 0.018" micro-puncture wire was inserted into the 'lumen' of the model, which served as a guide wire for the imaging catheter (**Fig. 4.4B**). Next, a 4 French (Fr) micro-puncture sheath was advanced over the guidewire and exchanged via a 0.035" guidewire for a 5-Fr Cordis vascular introducer sheath (Cordis Corporation, Miami Lakes, FL), de-gassed, flushed and secured in place. Then, a Hi-Torque Floppy II coronary guidewire (Abbott Vascular, Santa Clara, CA) with 0.014" x 190 cm dimensions was introduced into the lumen of the phantom and positioned distally. Finally, a Philips Volcano Eagle Eye Platinum 20 MHz Intravascular Ultrasound (IVUS) catheter was prepared, flushed and introduced over the coronary guidewire into the millifluidic phantom model and subsequently positioned within the proximal cephalic arch to simulate the *in vivo* starting IVUS position. The IVUS catheter was calibrated using the portable IVUS imaging console (**Fig. 4.4C**) to eliminate near-field ring-down artifact and the field of view was adjusted to ensure full circumferential visualization of the model (**Fig. 4.4D**). Interestingly, the contrast of the lumen images was higher in the PDMS millifluidic phantom model than in actual patient cephalic veins. Two independent IVUS pullback recordings in grayscale were performed using a research-quality pullback sled at a rate of 1.0 mm/s.

Venogram imaging was not required on the PDMS device; PDMS being transparent, allowed direct imaging of the general contour of the vein when perfused with food color dye. This image was processed using '*threshold*' and '*skeletonize*' functions in NIH ImageJ [69] to obtain the vein path. This was combined with the IVUS images of the millifluidic phantom device obtained as described above to reconstruct 3D models [44]**.**

4.3 Results and Discussion

Two series of IVUS pullback measurements were performed on the phantom, referred to as 'OG', (**Fig. 4.5A**), each of which was used to generate a 3D model *in silico* (**Fig. 4.5B, C**), referred as 'Val1' and 'Val2', respectively. 2D images of Val1 and Val2 in the xy-plane were captured at 5° rotational increment along the z-axis and co-axial to prebend vein path, up to 180° to compare the 3D models. Snapshots of OG, Val1 and Val2 were overlaid at each rotational angle and the overlap areas were calculated to quantify the differences in local topography. **Fig. 4.6** shows the models (in black) at rotational angles of 0°, 45° and 90°, along with their area overlap (white).

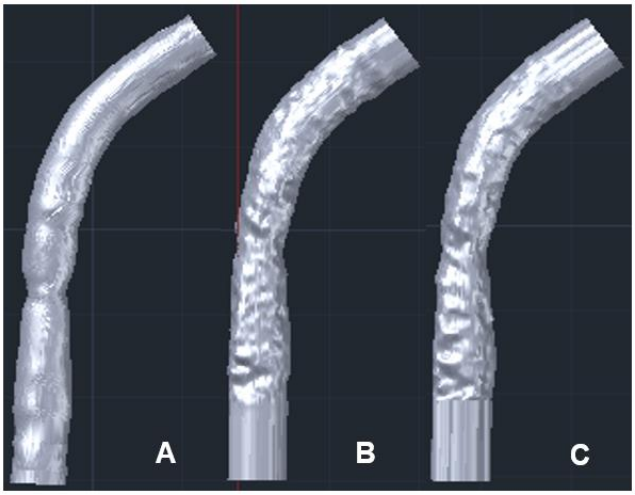

Figure 4.5: Computational phantom models used for geometric validation: (A) Original phantom computational model used for device fabrication. (B-C) Validation models reconstructed from IVUS and optical imaging performed on phantom millifluidic device (replicates).

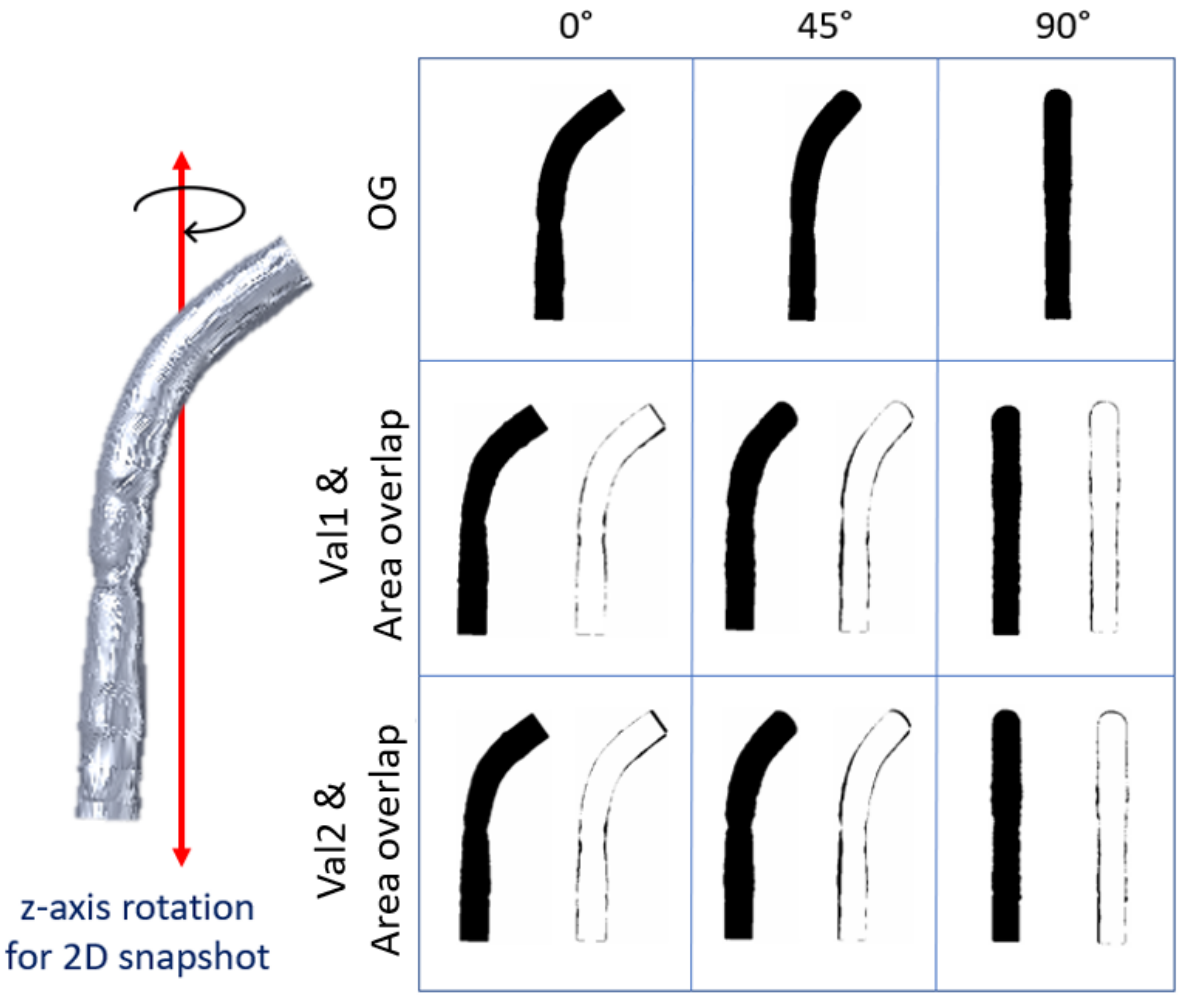

Figure 4.6: Geometric validation strategy schematic: all models were rotated with respect to the z-axis and 2D images from top perspective were overlapped to evaluate area overlap from 0-180° rotational angles with 5° rotational increments.

The total area projection in xy-plane for OG, Val1 and Val2 across 180° rotational angles are shown in **Fig. 4.7**, with an average overlap of 95.05 ± 3.92% (**Fig. 4.8**). This suggests that our 3D modeling of patient veins using IVUS and venogram imaging and 3D printing fabrication method yield reproducible vein models with relatively accurate representations of vein topographies. The Pearson correlation of the total areas between OG, Val1 and Val2 are > 0.5 across all rotational angles (**Table 4.1**). The area correlation between Val1 and Val2 is higher

($r_{(Val1\_Val2)}$ = 0.99) than either of these models with respect to OG ($r_{(OG\_Val1)}$ = 0.66 and $r_{(OG\_Val2)}$ = 0.62). We noted that IVUS imaging of the lumen in PDMS device offered higher contrast (**Fig. 4.4D**) compared to IVUS images of veins, potentially due to difference in material properties, leading to higher r value. Lower area correlation between the original and validation models could also result from the limited 3D-printing resolution. Overall, we see good agreement between the original and reconstructed models.

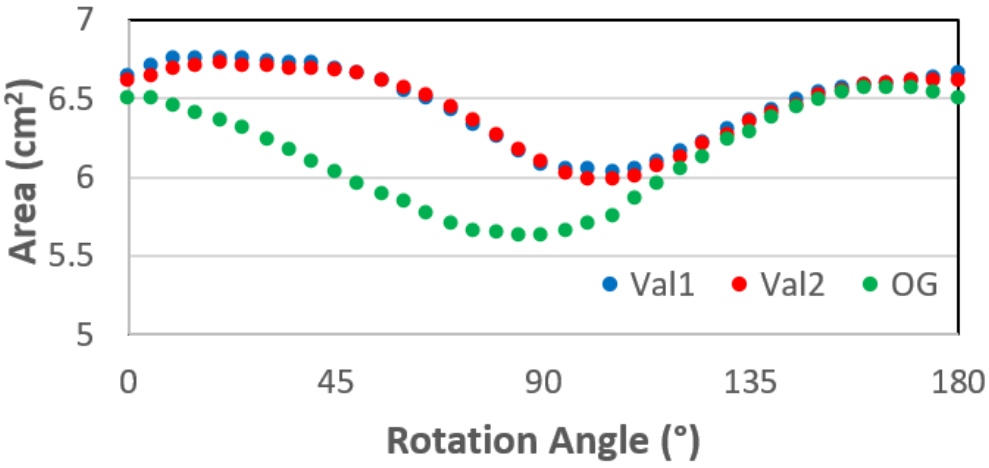

Figure 4.7: Area values for all models across 180° of z-axis rotation.

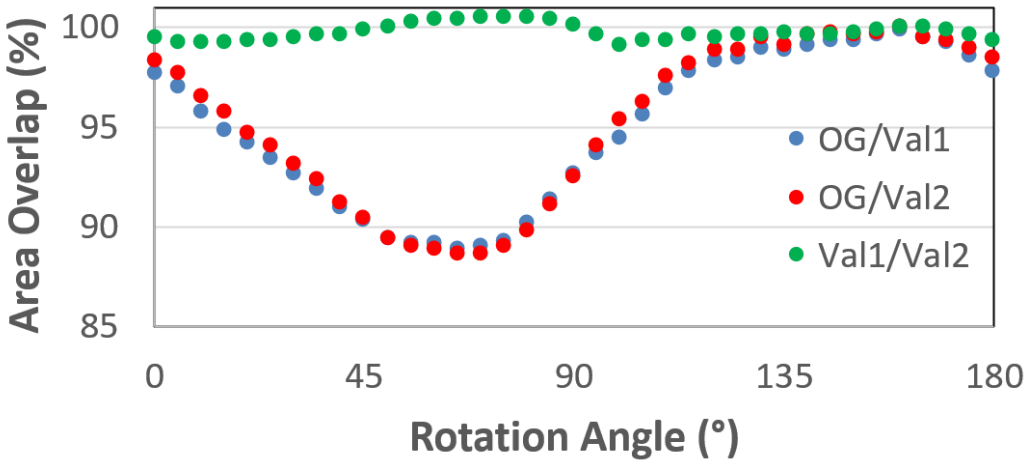

Figure 4.8: Area overlap between phantom computational models upon z-axis rotation.

Table 4.1: Area comparative analysis of original and validation phantom computational models

Phantom Model	Mean Total Area (cm^2)	Compared Models	Mean Area Overlap (%)	Area Pearson Coefficient (r)
Original	6.13 (±0.33)	$\frac{\text{OG}}{\text{Val1}}$	94.90 (±3.87)	0.66
Validation #1	6.46 (±0.25)	$\frac{\text{OG}}{\text{Val2}}$	95.20 (±4.08)	0.62
Validation #2	6.44 (±0.24)	$\frac{\text{Val1}}{\text{Val2}}$	99.70 (±0.40)	0.99

4.4 Conclusions

We were able to validate our fabrication method to confirm that it is able to faithfully recreate patient-specific vein geometries with high degree of fidelity. Subsequently, we will employ our 3D printing fabrication methods to create cephalic arch replicas of our studied patient cohort in the form of millifluidic devices. This will allow us to experimentally characterize WSS by imaging physiologic flow using a blood-mimicking fluid. Overall, this denotes a step closer towards quantifying WSS across patient-specific cephalic arches to better understand WSS influence over vascular pathologies.

Chapter 5

Wall Shear Stress Characterization at Constant Physiologic Flow Rates

This work is reprinted with permission from.; Moya-Rodríguez, A.; Xie, B.; Cook, D.; Klineberg, M.; Nathan, S.; Hammes, M; Basu, A. Creating Patient-Specific Vein Models to Characterize Wall Shear Stress in Hemodialysis Population. Submitted to Structural and Computational Biotechnology Journal on July 28th, 2022.

5.1 Introduction

Nonetheless, WSS studies in blood vessels have shown an exceptionally wide range of WSS values that are associated with stenosis which ultimately leads to thrombosis. Experiments carried out in porcine models show that carotid artery stenosis is promoted when WSS levels are around 800 mPa [70]. Moreover, in another study done in patients with moderately stenosed carotid arteries, Zhang et al found that the average axial WSS in local high and low-risk plaques was of 200 and 150 mPa, respectively [71]. Using a canine model for AVF stenosis, Jin et al reported that AVF regions prone to neointimal hyperplasia experienced a WSS range of [340 - 17,300] mPa while non-stenosed regions experienced a range of [1,150 – 11,730] mPa which makes it difficult to determine pathologic WSS given the range overlap [72]. Further studies in saphenous vein grafts and pulmonary veins show that stenosis-inducing WSS levels were 1,200 mPa and >1,000 mPa, respectively [73, 74].

Collectively, non-pathologic and pathologic WSS in different vascular systems (venous and arterial) and model organisms reported in literature often overlap, making it difficult to truly understand WSS influence in AVF maturation and patency [75]. Colley et al suggest that there is an optimal WSS range for each specific vascular segments which, upon surpassing in either

direction, result in vascular pathologies [76]. Given the differences in native blood vessel geometries and physiologic flow rates, what may be considered as pathologic WSS (i.e., inducing stenosis and/or thrombosis), has to be evaluated for a specific vein or artery, considering patient-specific patho-physiological parameters. Therefore, more studies that consider patient-specific geometries and hemodynamic conditions are necessary to understand how WSS affect stenosis and thrombosis through the course of disease.

5.2 Materials and Methods

5.2.1 Flow Setup

Millifluidic devices were imaged on an Olympus IX83 microscope (**Fig. 5.1**), perfused with blood-mimicking fluid (BMF, distilled water with 6.3 % (w/v) Dextran, D4876-50G, Sigma-Aldrich) with viscosity and density of 3.5 mPa*s and 1.022 ± 0.001 g/mL and containing trace amounts ($4x10^{-6}$ %, v/v) of 2-µm fluorescent polystyrene microbeads (Catalog # FCDG008, Bangs Labs). A concentration of 4 % Dextran in BMF (w/v) with a viscosity and density of 2.4 mPa.s and 1.013 ± 0.001 g/mL, respectively, was also used in some flow experiments. Comparing to physiologic blood, the reported viscosity range and density of human whole blood is [3.5 - 5] mPa*s and 0.994 ± 0.032 g/mL [77, 78]. BMF was perfused into the millifluidic devices under physiologic steady-state flow at 20 mL/min [18], using an OB1 MK3+ pressure-driven flow control system (Elvesys, France; **Fig. 5.1**). Component diagram of the fluidic circuit is shown (**Fig. 5.2**).

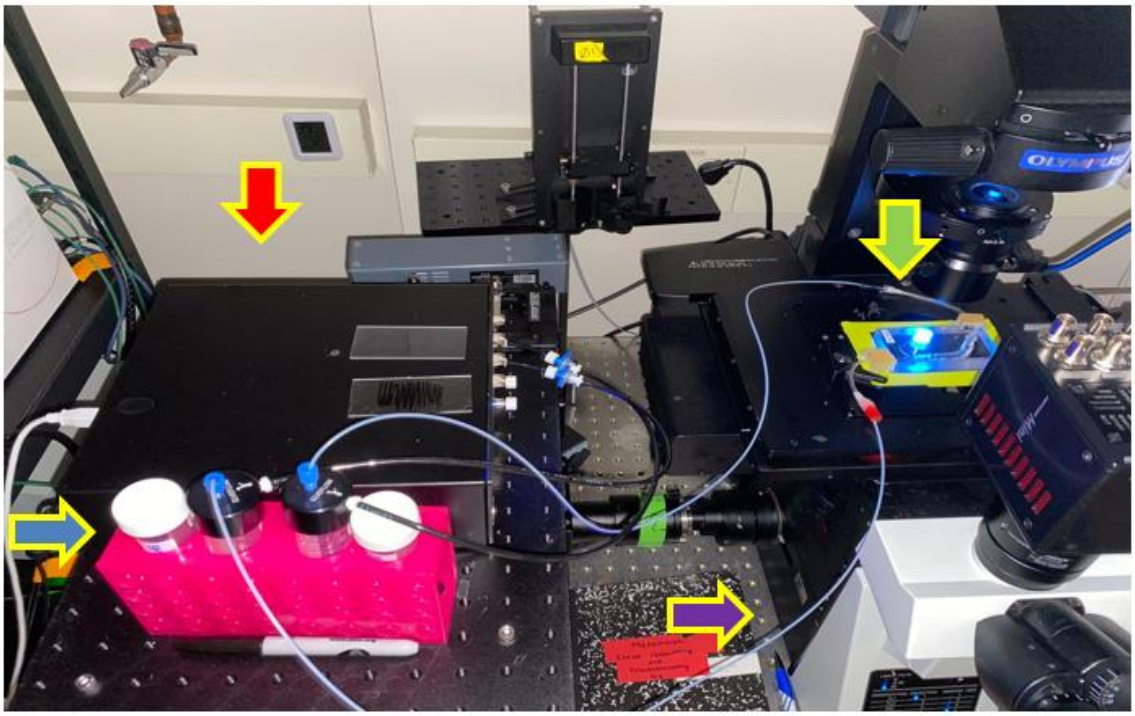

Figure 5.1: Experimental setup to image flow experiments. Components include: pressure modulator (red arrow) connected to air compressor, reservoir (blue arrow) of blood-mimicking fluid with fluorescent tracer beads, millifluidic device (green arrow) under flow mounted on the microscope stage.

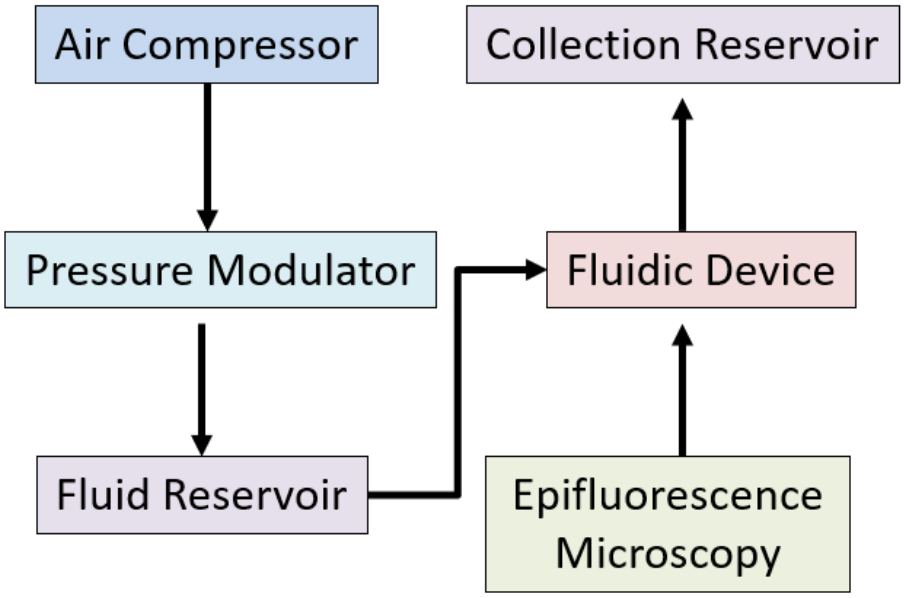

Figure 5.2: Component diagram of experimental flow/imaging setup.

5.2.2 Imaging

The steady-state flow at 20 mL/min, represents a healthy flow rate for non-arterialized cephalic veins [25]. BMF was flown at 20 mL/min into each device at steady-state to characterize WSS in the device as a function of local vein geometry; the flow rate was maintained while the cephalic arch models were imaged close to the device wall using epifluorescence microscopy. Image quality limitations only allowed imaging in areas close to the PDMS-BMF interface of the millifluidic device, henceforth referred to as the 'vein wall'. Focusing deeper into the BMF resulted in higher background fluorescence and also made the vein wall substantially more difficult to resolve in the images.

To calculate WSS, we imaged tracer beads flow close to the wall ($\leq$ 400 μm). Flow streamlines adjacent to the vein wall should accurately capture local flow velocities and WSS. Videos of flow trajectories of the fluorescent beads were imaged under 6.4X magnification (using a 4X, NA=0.16 objective and 1.6X built-in microscope magnification) at 40 frames per second (fps) and 50-100 ms exposure times (depending on device), using a Hamamatsu ORCA Flash4.0 camera and MetaMorph software (Molecular Devices, USA) under GFP illumination (488 nm/510 nm). Videos (100 image frames, each frame containing 2048x2048 pixels) of tracer beads streamlines were obtained from 18-22 positions, each referred to as a Region Of Interest (ROI), per device. Moreover, at least 10 streamlines were extracted per flow video frame. This yielded fluorescent streaks of reasonable lengths from which local flow velocities were calculated across outer and inner walls of prebend, bend and postbend regions (**Fig. 5.3**).

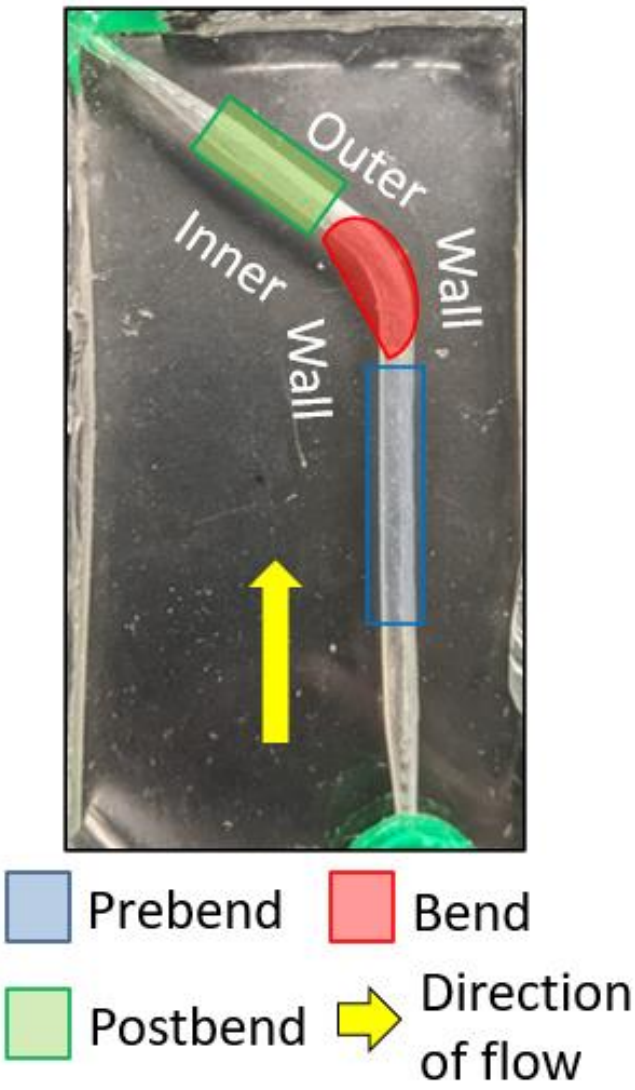

Figure 5.3: Vein region diagram showing prebend (blue), bend (red) and postbend (green) and employed direction of flow (yellow arrow).

Note that for a given flow velocity, longer exposure times lead to longer fluorescent streaks in the images (**Fig. 5.4A-C**). Videos containing 100 frames each were acquired per ROI and saved as 16-bit .tiff files for subsequent off-line data processing and analysis using ImageJ and Python, respectively. Overall, 18-22 ROIs were captured at a given flow rate per device, across prebend, bend and postbend regions.

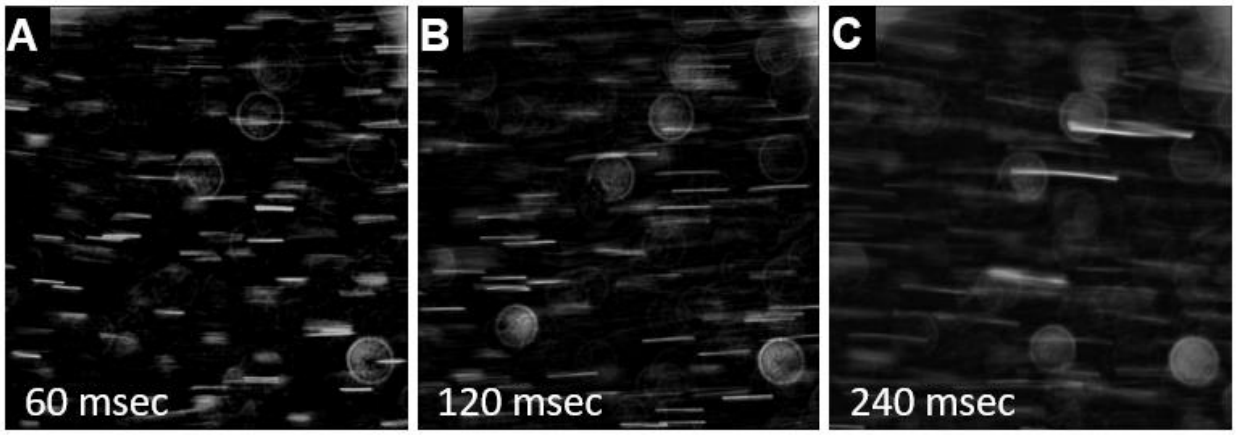

Figure 5.4: Sample ROI flow data depicting how increasing exposure time (msec) during image acquisition increases streamline length. Experimentally, exposure time is adapted to employed flow rates and millifluidic devices to yield sufficiently long streamlines for downstream analysis.

5.2.3 Image processing

All videos needed to be pre-processed with a macro-code written in NIH ImageJ [69] to extract a) high-contrast streamlines, and b) outline of the vein wall for any given ROI, before using our automated Python-based pipeline to calculate flow velocity and WSS. ImageJ pre-processing (**Fig. 5.5A-B**) consisted of the following functions performed sequentially on each raw image stack (**Fig. 5.6A**): contrast enhancement, background fluorescence subtraction, de-speckling, brightness and contrast adjustment (**Fig. 5.6B**), threshold adjustment (**Fig. 5.6C**), binarization, and 'Analyze Particles' to filter streamlines by size and circularity (**Fig. 5.6D**).

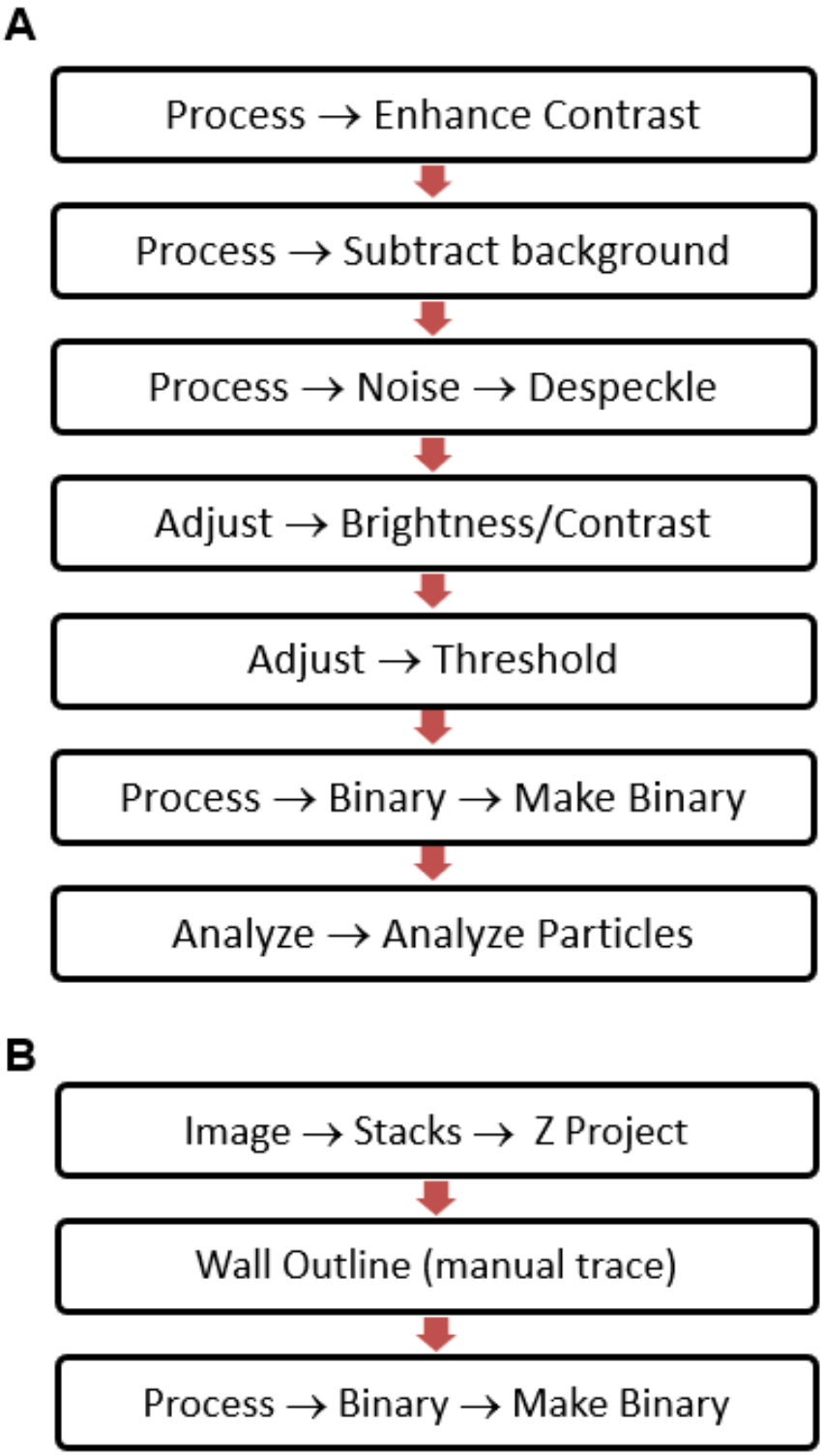

Figure 5.5: Image preprocessing steps using ImageJ to extract (A) streamlines, and (B) outline of the vein wall.

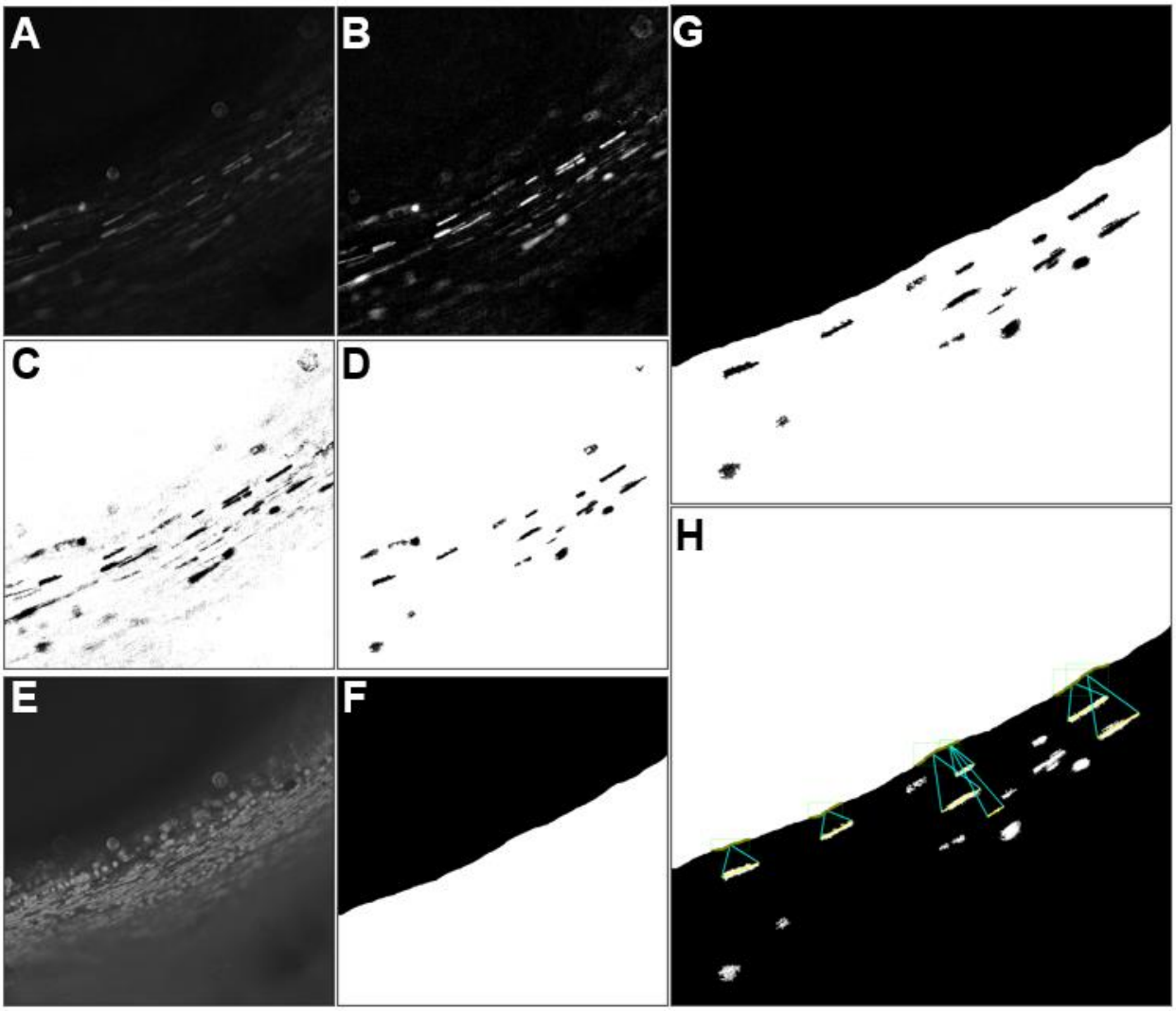

Figure 5.6: Image processing on sample ROI (A) ROI raw imaging data example from captured flow videos across the cephalic arch millifluidic devices. (B) Highlighted streamlines after sequentially: enhancing contrast, subtracting background, subtracting average intensity, despeckling and adjusting brightness and contrast (the latter being ROI dependent). (C) ROI dependent thresholding resulting in binary images that capture bright and well-defined streamlines. (D) Particle filtering by means of Analyze Particle function and adjusting size and circularity parameters to select for streamlines while filtering out low-quality out-of-focus streamlines and diffraction artifacts. € Max intensity projection of flow videos that facilitates outlining vein wall boundary. (F) Binary image generated after outlining vein wall boundary. (G) Addition of vein wall outline to filtered streamlines (D+F). (H) Streamline perpendicular projection onto vein wall boundary which allows calculating WSS.

The ‘Analyze Particles’ function is also useful to filter out image artifacts like diffraction rings, small debris, etc. Streamlines out of the focal plane that are less bright than the streamlines in the focal plane are filtered out. Given that experimental conditions such as flow rate, exposure time, magnification and numerical aperture of the objective, bead concentrations, etc. affected streamline quality and varied between experiments, the function parameters in the macro-code needed to be adjusted for each tiff-stack.

Identifying the vein wall boundary in the ROIs is important to calculate WSS. A maximum intensity Z-stack projection was made on the tiff-stack to generate a single wall boundary image from each ROI (**Fig. 5.6E**), manually outlined, binarized (**Fig. 5.6F**) and added to each frame of processed streamlines, using the ‘*Image Calculator*’ function. These image pre-processing steps generated .tiff files of 100 frames each for each ROI, with each frame containing binarized streamlines of fluorescent beads and the vein wall outline (**Fig. 5.6G**).

Since the binarized images produced by the ImageJ preprocessing were less susceptible to variation, we developed a customized image processing pipeline in Python to calculate velocity and WSS from the pre-processed data from each ROI. Individual image frames ordered in time were generated in .tiff format for analysis. To extract velocity streamlines in each image frame, we used the ‘*connected components detection*’ algorithm [79] in OpenCV, an open-source software package for computer vision [79], to obtain all connected objects in each image frame. Next, we assigned a tight bounding box to each connected component. Bounding boxes of those connected components that met the following criteria were selected as velocity streamlines per frame: size in pixels (area of the fitted bounding box ranging between [75, 9000]), shape (height/width ratio of the bounding box between [3, 100]), height between [15, 500], and width < 50.

After assigning velocity streamlines to each frame, we aggregated all streamlines in an ROI (as time series .tiff) into a global frame. We reconstructed the vein wall boundary per frame from the binarized contour of the wall boundary marked in each frame. We projected the velocity streamlines perpendicularly onto the wall boundary. For each pixel in the wall boundary, we searched all streamlines in the frame and collected those streamlines that were projected at 90^{o} onto the pixel point on the wall boundary (**Fig. 5.6H**). We also used the measured viscosity of the BMF and the perpendicular distance of detected streamlines to the wall boundary to calculate WSS. If multiple streamlines were projected to the same pixel in the wall boundary, an average WSS value was computed for the pixel.

Using the pipeline described above, we calculated frame-by-frame information on streamline count, mean velocity (mm/s) and mean WSS (mPa). Violin plots of the mean and distribution of velocity (red) and WSS (green) calculated from the streamlines in each frame are shown for a series of 100 frames acquired consecutively over time (**Fig. 5.7**) for an ROI chosen at random from the outer (top) and inner (bottom) walls of the prebend, bend and postbend regions of the pathologic model. For any given ROI, the velocity and WSS values fluctuate around an average that remains stable over time, as expected for constant flow rate.

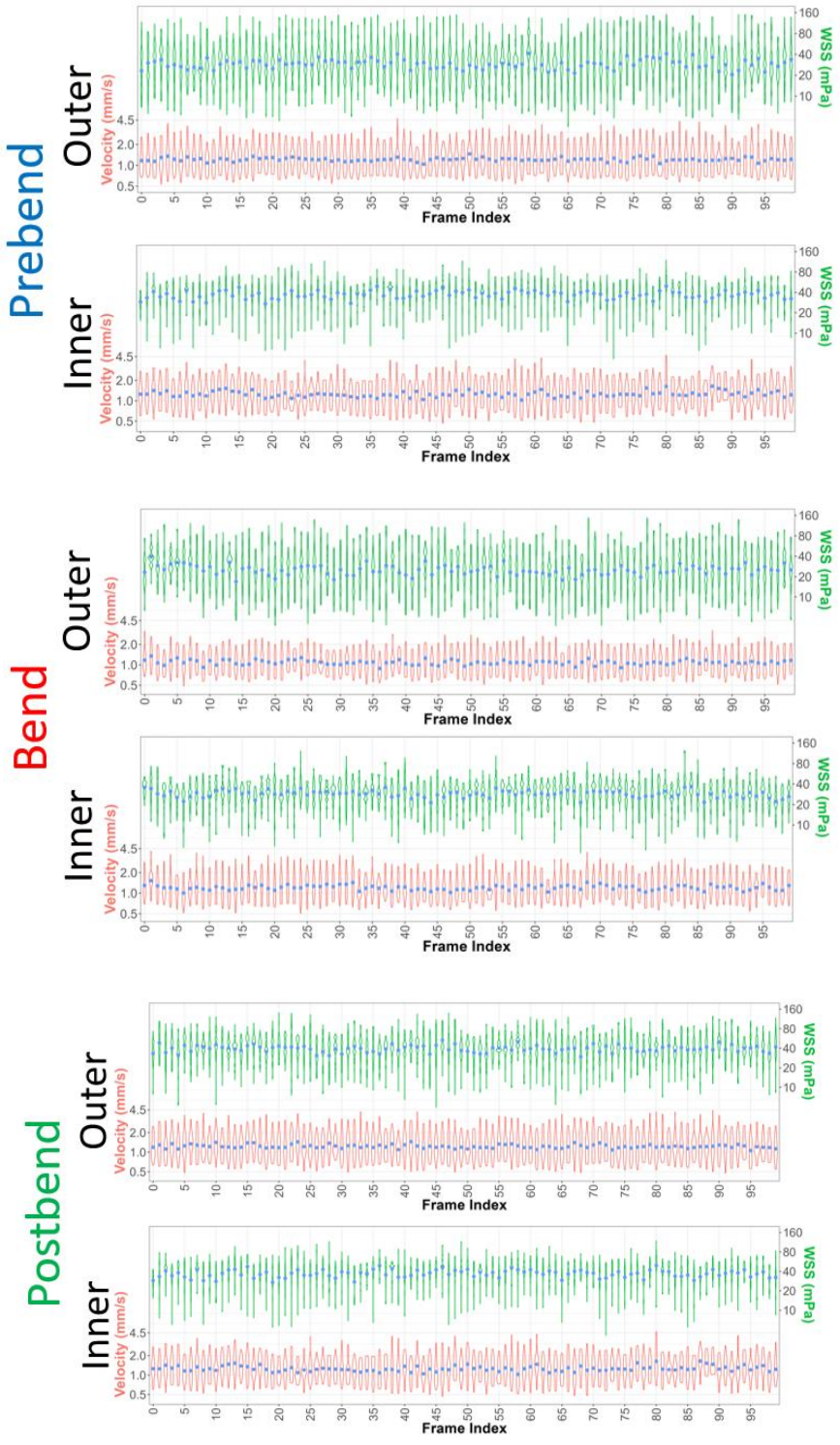

Figure 5.7: Flow video analysis output for six representative ROIs from the pathologic model across the three main regions (prebend, bend and postbend) and wall sides (inner and outer): WSS and streamline velocity violin plot across flow video frames.

5.2.4 Theory and Calculations

Wall shear stress, τ was calculated as:

$$\tau = \eta \frac{\mathrm{v}}{h},$$

where η is the fluid's dynamic viscosity, v is the streamline velocity and h is the distance between streamline and vein wall boundary.

Though the viscosity, η of blood and BMF are shear-thinning [80], we use an average value (3.5 mPa·s) for simplicity. This value was measured in BMF, using a rotational rheometer (Anton Paar MCR 301) under physiologic shear rates (20-200 s^{-1}) [63]. The coefficient of variation (CV) for WSS is calculated as $CV(\%) = \left(\frac{standard\ deviation_{WSS}}{mean_{WSS}}\right) * 100$. Since we used a fixed flow rate in all imaging experiments and vein diameter and surface topography influence flow velocity, we use CV to characterize and compare flow properties in different fluidic devices used in this study.

5.3 Results

ROIs in each device were grouped by the inner and outer walls of the prebend, bend and postbend regions and their WSS values were averaged to obtain a representative value for these regions. Average WSS values in the inner prebend, inner bend, inner postbend, outer prebend, outer bend and outer postbend regions in each device are shown in **Fig. 5.8**. When averaging across all ROIs in a given model, we found that the highest average WSS value of 255.38 ± 54.08 mPa was measured in the 'physiologic' device with the smallest average vein diameter (**Table 5.1**). Conversely, the lowest WSS values (26.89 ± 6.18 mPa) were measured in the inner prebend region of the 'P104, 12 mo.' device (**Fig. 5.8**) that also had the largest average vein diameter. Overall, average WSS, calculated from all ROIs in a device, scaled inversely with the average vein diameter of the device (**Fig. 5.9**).

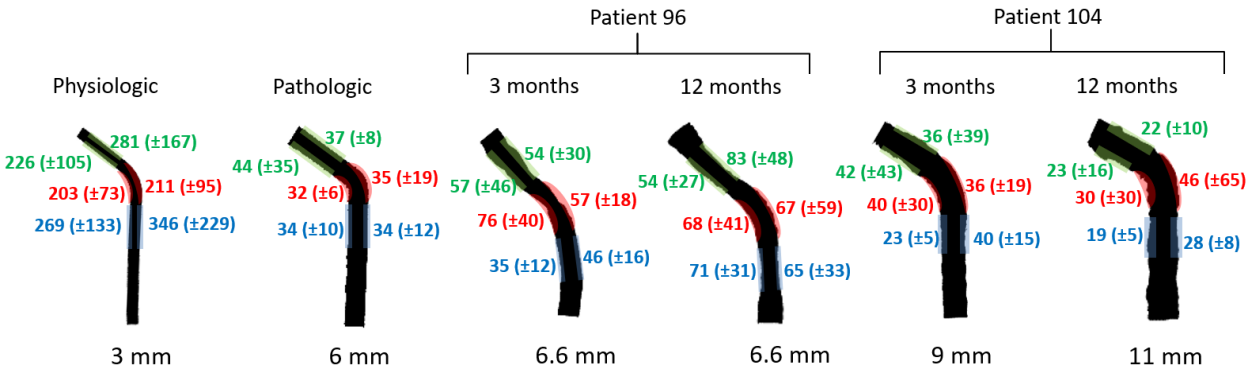

Figure 5.8: Experimental WSS profiles depicts the average WSS (mPa) value per vein region and wall side under normal physiologic flow of 20 mL/min using a blood-mimicking fluid. Vein model average vein diameter (mm) is shown below each cephalic arch outline.

Table 5.1: Geometric parameters, BMF viscosity, experimental WSS values (min, max, global average and median), mean frames per flow video, WSS CV values and ROI wall coverage values across cephalic arch millifluidic devices under physiologic flow.

Model	Diameter (mm)	Vein Surface Topography	BMF Viscosity (mPa*s)	Min WSS (mPa)	Max WSS (mPa)	Global Average WSS (mPa)	WSS Median (mPa)	Mean Frames per Flow Video	Average WSS CV (%)	Average ROI Wall Coverage (%)
Physiologic	3	Smooth	3.5	34.13	2688.16	255.38 (±54.08)	199.35	99.95	73.98	96.67
Pathologic	6	Smooth	3.5	4.56	479.55	34.52 (±1.36)	29.48	99.95	81.54	96.02
P96 3mo	6.6	Rough	3.5	8.29	431.44	54.11 (±10.32)	43.34	100.00	73.92	89.12
P96 12mo	6.6	Rough	3.5	11.92	561.90	70.76 (±3.26)	53.70	100.00	79.99	88.25
P104 3mo	9	Rough	3.5	3.23	1261.63	35.75 (±3.91)	22.04	99.55	118.61	97.92
P104 12mo	11	Rough	3.5	3.58	1132.31	26.89 (±6.18)	15.94	99.73	161.87	97.15

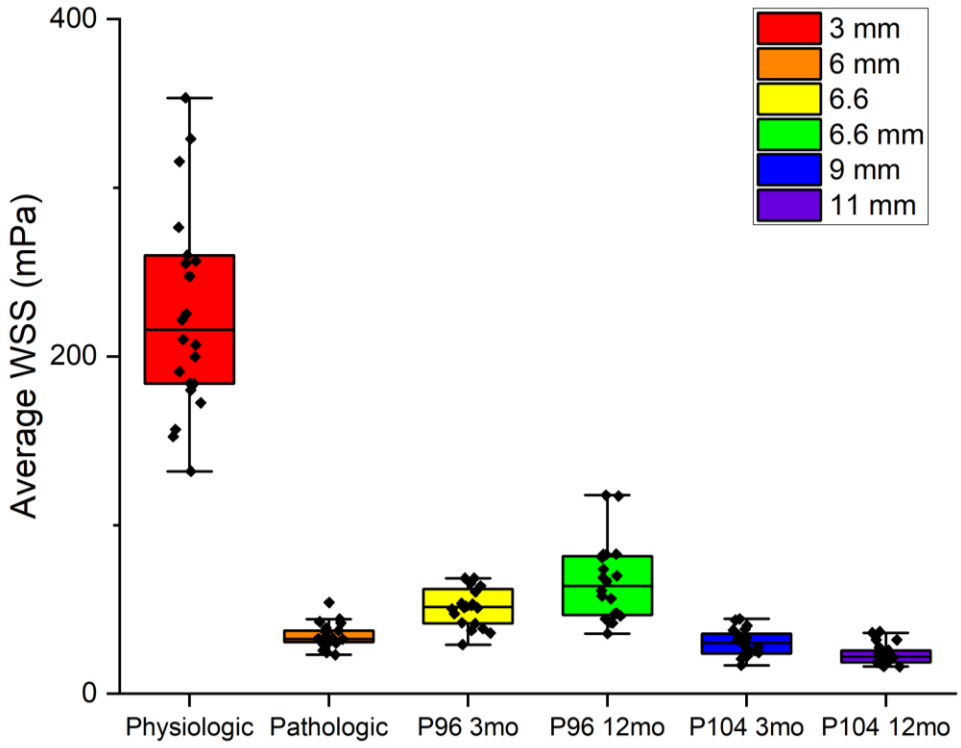

Figure 5.9: Average WSS box plot across all models and their respective ROIs, average vein diameters shown on legend. Flow data collected using BMF with viscosity of 3.5 mPa*s under physiologic flow.

WSS values measured in the physiologic model under physiological flow rates ranged between 203 ± 73 mPa in the inner bend to 346 ± 229 mPa in the outer prebend regions (**Fig. 5.8**). Note that these values are within the range of physiologic WSS values previously reported in the cephalic vein [81]. Next, we compared flow in the physiologic and pathologic models that have same arch angle but different vein diameters (3 and 6 mm, respectively). We measured relatively symmetric WSS in the bend region and striking asymmetry in the postbend region (**Figs. 5.8, 5.10A**). This agrees with fluid dynamics principles in pipe flow at geometric bends [44]. In this situation, higher velocities are expected at the outer wall of the postbend region, along with lower velocities close to the opposite wall (inner bend). WSS polarization in prebend region is absent in

the pathologic model, consistent with shorter velocity streamlines measured in the pathologic model, at similar volumetric flow rates [44]. We acknowledge that this polarization in WSS could also be due to artifacts in fabrication or flow setup (described later).

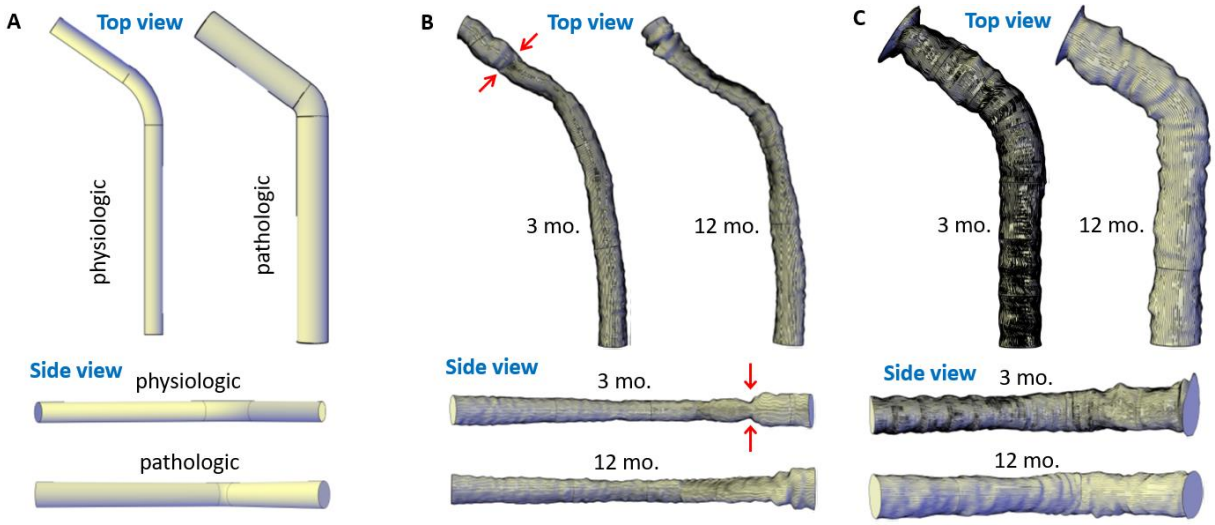

Figure 5.10: Top and side views of (A) physiologic and pathologic, (B) P96: 3 and 12 mo., and (C) P104: 3 and 12 mo. cephalic arch models. Red arrows in (B) in P96, 3 mo. model highlight a constriction in the postbend region. Patient-to-patient geometric heterogeneity and evolution is depicted across time.

Despite patient P96 having similar average diameters (6.6 mm) and arch angles (133° and 132° at 3- and 12-mo., respectively), we identified significant geometric remodeling of the cephalic arch in 3D, particularly at the postbend region, which narrowed between 3 and 12 mo. (**Fig. 5.10A**). These geometric changes influence resulting WSS across different regions of the cephalic arch. For example, we observed significant increase in WSS in the prebend region and the outer wall of the postbend region from 3 to 12 mo. Moreover, WSS evens out in the bend region at 12-months, which contrasts the striking asymmetry observed at 3 mo. These findings indicate that AVF maturation can prominently affect hemodynamics in the cephalic arch through subtle geometric and topographical changes.

Using the pathologic and P96 models to compare veins of similar sizes (6 and 6.6 mm, respectively), we note differences in WSS patterns in the prebend and bend regions between the models. Except for the postbend region, the pathologic model has similar WSS magnitudes on the inner and outer walls. This is not the case for P96 models at 3 and 12 mo. where WSS is asymmetric in the inner and outer bend, across all regions. This is most likely due to the uneven topography of the vein walls in P96, compared to the smooth wall of pathologic model and symmetric geometry along the vein lumen (**Fig. 5.8, 5.10A-B**). For patient P104, the average vein diameter increases from 9 mm to 11 mm and arch angle decreases from 125° to 115° between 3 and 12 mo., respectively (**Fig. 5.8, 5.10C**). Except for the outer bend region in P104, there is consistent decrease in WSS at decreased flow velocity due to increase in vein diameter (at fixed volumetric flow rate).

At fixed volumetric flow rate, we measure greater CV in average WSS with increased vein diameter (**Fig. 5.11**). Devices with narrower veins, e.g., physiologic device (3 mm) show low CV (74%), whereas devices with larger vein diameter (11 mm in P104, 12 mo.) record larger CV (162%). We also characterized WSS and CV in the pathologic and P104 (3 and 12 mo.) devices at 20 mL/min, but at two different viscosities, 2.4 and 3.5 mPa·s (**Figs. 5.12, 5.13)** by adjusting the concentration of dextran in BMF. We found reproducible trends at these viscosities, where WSS CV increased systematically with average vein diameter: the pathologic model (6 mm) showed the lowest CV, followed by the CV in P104, 3 mo. (9 mm) and P104, 12 mo. (11 mm) models (**Fig. 5.13**). We noted lower average WSS and standard deviation at 2.4 mPa.s, compared to 3.5 mPa.s. These results highlight the complexity of the system where vein diameter, geometry, surface topography and viscosity contribute to WSS in the cephalic arch.

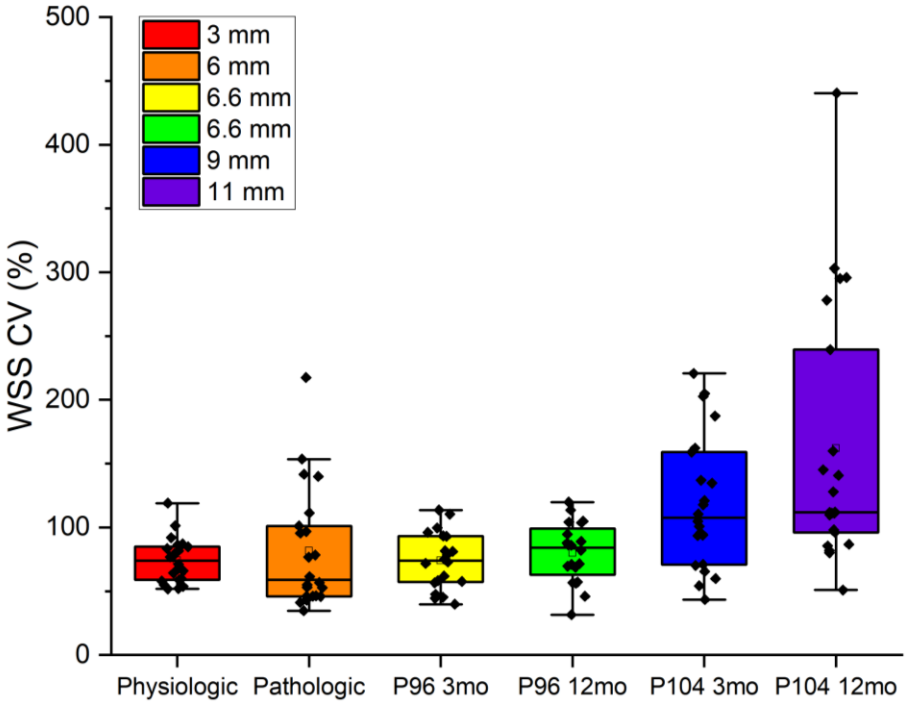

Figure 5.11: WSS CV box plot across all models and their respective ROIs, average vein diameters shown on legend. Flow data was collected using BMF with viscosity of 3.5 mPa*s under physiologic flow.

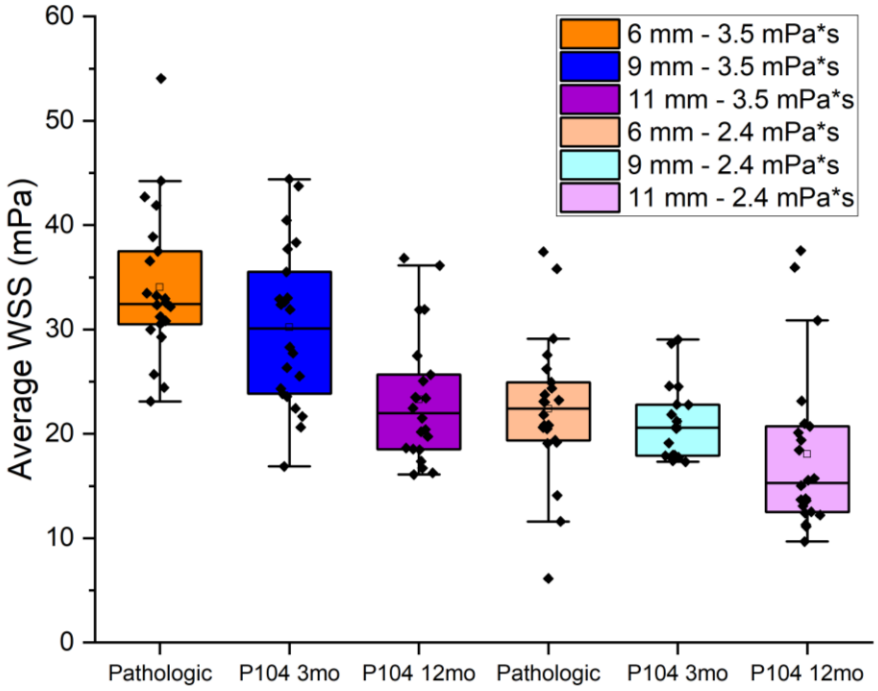

Figure 5.12: Average WSS plot for pathologic and P104 cephalic arch models under physiologic flow using BMF of varying viscosity (2.4 and 3.5 mPa*s). Average vein diameters and viscosities are shown in legend.

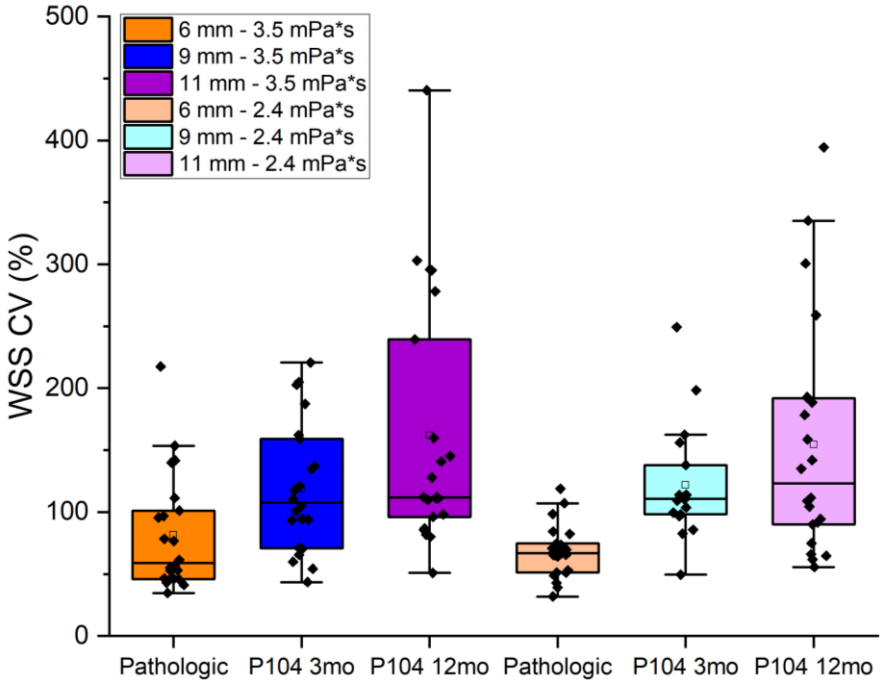

Figure 5.13: WSS CV box plot for pathologic and P104 cephalic arch models under physiologic flow using BMF of varying viscosity (2.4 and 3.5 mPa*s). Average vein diameters and BMF viscosity are shown on legend.

5.4 Discussion

Hemodialysis patients with AVF undergo continuous changes in the cephalic arch, including vein diameter, topography, arch angle, blood flow rate, viscosity and pulsatile flow. These physical factors collectively affect local WSS which elicit diverse and area-specific responses in the vein endothelium to initiate the coagulation cascade [82, 83] toward thrombosis. Changes in these physical parameters between patients as well as between time points (e.g., 3 and 12 mo. after AVF creation) for any given patient make it difficult to assess thrombosis risk in the patient population.

Our physical models present a means characterize WSS in the cephalic arch, understand the contribution of these factors in creating abnormal hemodynamic conditions that cause thrombosis and finally, systematically manipulate these physical parameters in patient-specific manner with the aim to adjust WSS in the cephalic arch, through clinical intervention within

physiological limits to prevent thrombosis in hemodialysis patients. This study presents the fabrication of fluidic models that recreate patient-specific vein geometry, infusion of the device models with a fluid that mimics blood density and viscosity, recapitulate physiologic flow on the devices, and imaging-based characterization of velocity and WSS of the models. We image close to the vein wall (within 400 μm) which was sufficient to calculate WSS across all ROI in all models.

We saw that average WSS decreased with increase in average vein diameter (**Fig. 5.9**); however, patient-specific vein geometry and wall topography also influenced WSS. CV in average WSS, however, roughly increased with increase in vein diameter (**Fig. 5.11**). For example, comparing the pathologic and P96 models with roughly similar vein diameters but marked different geometry and wall topography, the pathologic model recorded lower WSS than the P96 models but all three models showed similar CV. Surface topography does not seem to be a major contributor to WSS dispersion in relation to mean WSS in relatively small veins under physiologic flow.

WSS values outside the physiologic venous range [76-760] mPa can lead to stenosis (if < 76 mPa) and endothelial denudation (if > 40,000 mPa) [41]. In our experiments, we only get physiologic WSS values in the physiologic model. All other models had WSS values below 76 mPa, but we emphasize that we did these experiments under (lower) physiologic cephalic vein flow rates (at 20 mL/min). We are currently optimizing our device fabrication and experimental setup to achieve and endure higher pathologic flow rates [262 – 1,512] mL/min, as measured in the two patients in this study. We hypothesize that these high flow experiments will result in higher WSS values, potentially higher than 760 mPa, but might reveal regions throughout the cephalic arch that still retain WSS values < 76 mPa, as predicted in previous computational studies.

We found that the physiologic model and P96 models, the latter being more than double the diameter of the former and topographically rugged, had very similar CV values. Thus, surface topography does not seem to be a major contributor to WSS dispersion in relation to mean WSS in relatively small veins under physiologic flow. Moreover, comparable CV values are also obtained within the pathologic model, where the vein is twice times as wide as the physiologic model. Nonetheless, topographical descriptions of these models are strictly qualitative, so devising a quantifiable measure of ruggedness will progress our understanding of topography-WSS interplay.

It is evident that cephalic arches of patient models (P96 and P104 at 3 and 12 mo.) responded differently in terms of vein remodeling to AVF placement and hemodialysis treatment. Upon further optimization of our devices and flow imaging scheme to achieve pathologic patient-specific flows and generate pathologic experimental WSS profiles, we expect drastic differences in WSS magnitudes that could correlate with biophysical signaling resulting in observed patient-specific geometric phenotypes.

Blood viscosity, a crucial factor influencing WSS, can fluctuate over time in a patient-specific manner. We identified significant effect of viscosity on WSS (**Fig. 5.12**) but not on its CV (**Fig. 5.13**). Changes in whole-blood viscosity and WSS likely trigger endothelial cell activation before and after hemodialysis sessions where solute concentrations and osmotic pressures are readjusted, especially when treatment is administered three times a week [84].

5.5 Limitations and Future Directions

Certain limitations in our setup prevented reproducing hemodynamic conditions in the cephalic arch of AVF patients. As mentioned earlier, an eddy in the prebend region (**Fig. 5.14A**),

generated by a mismatch in tubing and device diameters, prevented us from imaging the entire device. In future studies, we will mitigate the effect by replacing our current connection tubing of 1/16" ID with wider tubing. This will create a more gradual transition in flow velocities from tubing to vein model, thus decreasing the size of the eddy. Preliminary experiments with wider tubing seem to eliminate any eddy formation in the prebend region (**Fig. 5.14B**), though further experiments are needed to confirm if this holds true across all models and different experimental conditions. We also expect that larger ID connection tubing will allow us to achieve pathologic flow rates. Also note that the size and magnitude of this eddy in the prebend also depend on viscosity, a parameter that varies from patient to patient.

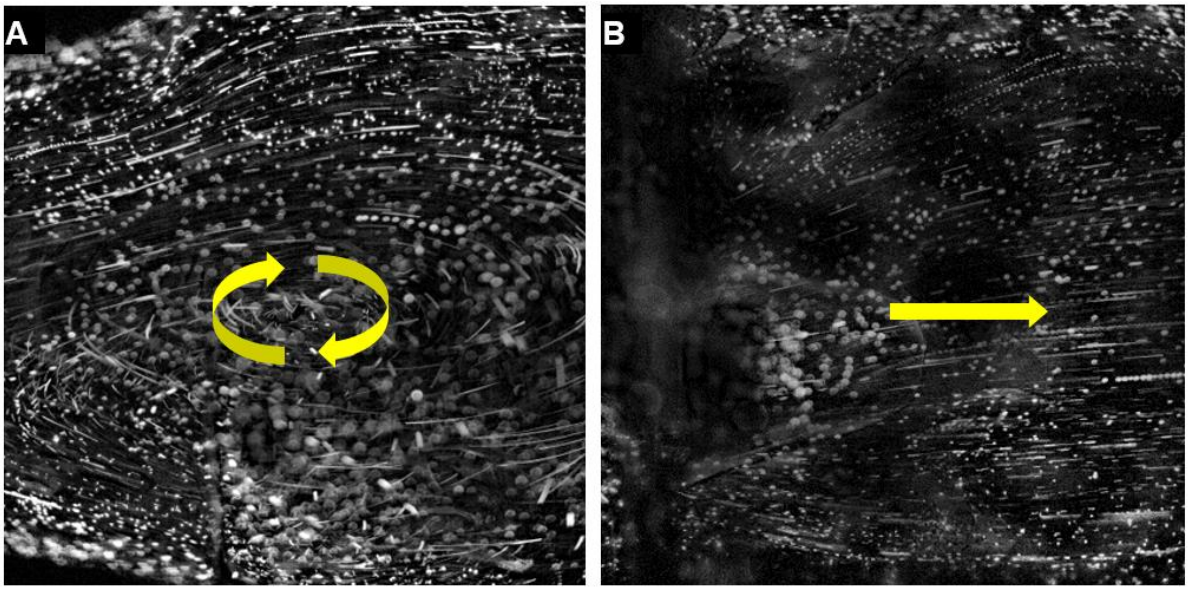

Figure 5.14: Images comparing the effect of narrow and wide inlet tubing diameter on flow at the prebend regions of millifluidic devices under physiologic flow condition. (A) Narrow tubing causes an eddy (yellow arrows indicate the direction of flow) extending up to a small portion of the prebend region. (B) Laminar flow (yellow arrow indicates the direction of flow) in the prebend region of the millifluidic device is achieved by increasing inlet tubing diameter and improving tubing-device connection. The images are constructed from videos of tracer beads in the prebend region.

Currently, our models reliably achieve flow rates of 20 mL/min seen in physiologic conditions but falls far short of flow rates > 350 mL/min seen in patients under hemodialysis [46]. Additionally, we are developing the capability of modulate flow rates in a programmable way on our current setup to match patient-specific pulse profiles, along with data processing tools to calculate WSS under pulsatile flow [43]. These flow parameters are also of interest since pulsed flow in veins, coupled with dramatically increased flow rates might synergize together, resulting in thrombosis and clotting pathology in the hemodialysis population. Finally, adding a layer of endothelial cells to the inner wall of these millifluidic devices [85] and quantifying their biochemical responses under flow [86, 87] are necessary to biologically complement generated WSS profiles [44].

Due to limitations in imaging setup (objective with low NA (0.16), imaging through thick layer of PDMS and high scattering), we were unable to image deep into the fluidic devices. As a consequence, we limit WSS measurements to the lower half of the vein (closer to the objective). However, the asymmetric geometry of the fluidic models requires better coverage in imaging the devices in the current configuration, including their upper half. This can be achieved by using confocal microscopy, objective with high NA and long working distance, and lower concentration of tracer beads in flow experiments (conversely, the device may be also flipped to image the upper half in the current configuration). Additionally, newer 3D printer models are now capable of XY and Z-layer printing resolutions that surpass TAZ4 3D printer used in this study. It is reasonable to expect higher correlations and area overlap between original and validation models by using improved 3D printing resolution.

Nonetheless, the present work shows that we have developed a robust workflow and analysis pipeline to characterize WSS under healthy, physiologic flow conditions, a base

knowledge needed to contrast from pathologic findings in the future. Also, if venous blood clots can be recreated *in vitro* in our devices, extracted and studied by histological and biochemical methods, they can lead to the synthesis of novel and more efficient anticoagulant and thrombolytic therapies that help decrease lethal thrombotic events.

5.6 Conclusions

In this work, we explored diverse geometries of the cephalic arch in hemodialysis patients with AVF. Nonetheless, we must recognize that vein physiology is constantly evolving and adapting to genetic and environmental inputs, especially in artificial circulatory scenarios such as AVFs. Therefore, in order to address current AVF failure rate, we set out to design and fabricate patient-specific cephalic arch replicas in the form of millifluidic devices to characterize hemodynamics and WSS under physiologic flow. We also created an image analysis pipeline to characterize flow and calculate WSS from videos of tracer particle streamlines. We applied novel 3D printing and advanced biomedical imaging technologies to study fistulas and connected vessels that are affected by thrombosis. To our knowledge, this is the first experimental work to generate patient-specific AVF vein models to help characterize geometric and flow abnormalities that underlie thrombosis and associated pathologies in the clinical setting.

References

1. United States Renal Data System. 2018 USRDS annual data report: Epidemiology of kidney disease in the United States. National Institutes of Health, National Institute of Diabetes and Digestive and Kidney Diseases, Bethesda, MD, 2018.

2. Konner K, Nonnast-Daniel B and Eberhard Ritz. The Arteriovenous Fistula. JASN June 2003; 14 (6): 1669-1680.

3. Pisoni RL, Zepel L, Fluck R, Lok CE, Kawanishi H, Süleymanlar G, et al. International Differences in the Location and Use of Arteriovenous Accesses Created for Hemodialysis: Results From the Dialysis Outcomes and Practice Patterns Study (DOPPS). American Journal of Kidney Diseases. 2018;71(4):469-78. doi: https://doi.org/10.1053/j.ajkd.2017.09.012.

4. Casserly LF, Dember LM. Thrombosis in End-Stage Renal Disease. Seminars in Dialysis. 2003;16(3):245-56. doi: 10.1046/j.1525-139X.2003.16048.x.

5. Quencer KB, Oklu R. Hemodialysis access thrombosis. Cardiovasc Diagn Ther. 2017;7(Suppl 3):S299-S308. doi: 10.21037/cdt.2017.09.08. PubMed PMID: 29399534.

6. Vachharajani, TJ. Dialysis Access Atlas. Fellows and Nephrologists on Access Nephrology, Nov 2010; https://www.slideshare.net/kenar78/dialysis-access-atlas.

7. Thamer M, Lee TC, Wasse H, Glickman MH, Qian J, Gottlieb D, et al. Medicare Costs Associated With Arteriovenous Fistulas Among US Hemodialysis Patients. American Journal of Kidney Diseases. 2018;72(1):10-8. doi: 10.1053/j.ajkd.2018.01.034.

8. Goodkin DA, et al. Association of Comorbid Conditions and Mortality in Hemodialysis Patients in Europe, Japan, and the United States: The Dialysis Outcomes and Practice Patterns Study (DOPPS). JASN December 2003, 14 (12) 3270 - 3277.

9. Pisoni RL, Zepel L, Fluck R, Lok CE, Kawanishi H, Süleymanlar G, et al. International Differences in the Location and Use of Arteriovenous Accesses Created for Hemodialysis: Results From the Dialysis Outcomes and Practice Patterns Study (DOPPS). American Journal of Kidney Diseases. 2018;71(4):469-78. doi: https://doi.org/10.1053/j.ajkd.2017.09.012.

10. Bello, A.K., Okpechi, I.G., Osman, M.A. *et al.* Epidemiology of haemodialysis outcomes. Nat Rev Nephrol 18, 378–395 (2022). https://doi.org/10.1038/s41581-022-00542-7.

11. Beathard GA, Jennings WC, Wasse H, et al. ASDIN white paper: Management of cephalic arch stenosis endorsed by the American Society of Diagnostic and Interventional

Nephrology. The Journal of Vascular Access. 2021;0(0). doi:10.1177/11297298211033519.

12. Kim Y, Kim HD, Chung BH, Park CW, Yang CW, Kim YS. Clinical predictors of recurrent cephalic arch stenosis and impact of the access flow reduction on the patency rate. J Vasc Access. 2022 Sep;23(5):718-724. doi: 10.1177/11297298211008758.

13. Huang, E.PY., Li, MF., Hsiao, CC. et al. Undersized stent graft for treatment of cephalic arch stenosis in arteriovenous hemodialysis access. Sci Rep 10, 12501 (2020).

14. Vachharajani TJ, Taliercio JJ, Anvari E. New Devices and Technologies for Hemodialysis Vascular Access: A Review. Am J Kidney Dis. 2021 Jul;78(1):116-124.

15. Bai H, et al.Artery to vein configuration of arteriovenous fistula improves hemodynamics to increase maturation and patency. Sci. Transl. Med., 12 (557) (2020).

16. Carroll JE, et al. Tracking geometric and hemodynamic alterations of an arteriovenous fistula through patient-specific modelling. Computer Methods and Programs in Biomedicine, Volume 186, 2020.

17. Iwai R, Shimazaki T, Kawakubo Y, Fukami K, Ata S, Yokoyama T, Hitosugi T, Otsuka A, Hayashi H, Tsurumoto M, Yokoyama R, Yoshida T, Hirono S, Anzai D. Quantification and Visualization of Reliable Hemodynamics Evaluation Based on Non-Contact Arteriovenous Fistula Measurement. Sensors. 2022; 22(7):2745. https://doi.org/10.3390/s22072745.

18. Suqin L, et al. Assessment of the Hemodynamics of Autogenous Arteriovenous Fistulas With 4D Phase Contrast-Based Flow Quantification MRI in Dialysis Patients. Journal of Magnetic Resonance Imaging 51, no. 4 (2020): p.1272-1280.

19. Bozzetto M, Soliveri L, Poloni S, et al. Arteriovenous fistula creation with VasQTM device: A feasibility study to reveal hemodynamic implications. The Journal of Vascular Access. 2022;0(0). doi:10.1177/11297298221087160.

20. Abreu, Rui. New hemodynamic variables as predictors of arteriovenous fistula maturation. Seminars in Dialysis 35, no. 4 (2022): p.358-362.

21. Kaufman JS. Antithrombotic Agents and the Prevention of Access Thrombosis. 2000;13(1):40-6. doi: 10.1046/j.1525-139x.2000.00012.x.

22. Dember LM, Beck GJ, Allon M, Delmez JA, Dixon BS, Greenberg A, et al. Effect of Clopidogrel on Early Failure of Arteriovenous Fistulas for Hemodialysis: A Randomized Controlled Trial. JAMA. 2008;299(18):2164-71. doi: 10.1001/jama.299.18.2164 %J JAMA.

23. Hammes M, Boghosian M, Cassel K, Watson S, Funaki B, Doshi T, et al. Increased inlet blood flow velocity predicts low wall shear stress in the cephalic arch of patients with brachiocephalic fistula access. PLoS One. 2016;11(4). doi: 10.1371/journal.pone.0152873.

24. McCullough JWS and Coveney PV. High fidelity blood flow in a patient-specific arteriovenous fistula. arXiv Jun 2021 arXiv:2012.04639.

25. Albayrak, R., Yuksel, S., Colbay, M., Degirmenci, B., Acarturk, G., Haktanır, A. and Karaman, O. (2007), Hemodynamic changes in the cephalic vein of patients with hemodialysis arteriovenous fistula. J. Clin. Ultrasound, 35: 133-137. https://doi.org/10.1002/jcu.20307.

26. Goldstein LJ, Gupta S. Use of the radial artery for hemodialysis access. Arch Surg. 2003 Oct;138(10):1130-4. doi: 10.1001/archsurg.138.10.1130. PMID: 14557132.

27. Çildağ B, Köseoğlu K. Discriminative Role of Brachial Artery Doppler Parameters in Correlation with Hemodialysis Arteriovenous Fistula. Medicine and Pharmacy Reports [Internet]. 30Oct.2017 [cited 28Sep.2022];90(4):407-10.

28. Fructuoso M, Ferreira J, Sousa P. Surgical Treatment of Cephalic Arch Problems in Arteriovenous Fistulas: A Center Experience. Ann Vasc Surg. 2018 Apr; 48:253.e11-253.e16. doi: 10.1016/j.avsg.2017.11.034. Epub 2018 Feb 5. PMID: 29421426.

29. Bennett S, Hammes MS, Blicharski T, Watson S, Funaki B. Characterization of the Cephalic Arch and Location of Stenosis. The Journal of Vascular Access. 2015;16(1):13-18. doi:10.5301/jva.5000291.

30. Hammes MS, Funaki B, and Coe FL. (2008), Cephalic arch stenosis in patients with fistula access for hemodialysis: Relationship to diabetes and thrombosis. Hemodialysis International, 12: 85-89. https://doi.org/10.1111/j.1542-4758.2008.00246.x.

31. Hammes MS, et al. Characteristic differences in cephalic arch geometry for diabetic and non-diabetic ESRD patients, Nephrology Dialysis Transplantation, Volume 24, Issue 7, July 2009, Pages 2190–2194, https://doi.org/10.1093/ndt/gfp062.

32. Hammes MS, et al. (2008), Cephalic arch stenosis in patients with fistula access for hemodialysis: Relationship to diabetes and thrombosis. Hemodialysis International, 12: 85-89. https://doi.org/10.1111/j.1542-4758.2008.00246.x.

33. Oklu, R. Thrombosis. Cardiovascular Diagnosis and Therapy 7(3) 2017.

34. Fitzgerald JT, Schanzer A, Chin AI, McVicar JP, Perez RV, Troppmann C. Outcomes of Upper Arm Arteriovenous Fistulas for Maintenance Hemodialysis Access. Arch Surg. 2004;139(2):201–208. doi:10.1001/archsurg.139.2.201.

35. Al-Jaishi AA, Oliver MJ, Thomas SM, Lok CE, Zhang JC, Garg AX, Kosa SD, Quinn RR, Moist LM. Patency rates of the arteriovenous fistula for hemodialysis: a systematic review and meta-analysis. Am J Kidney Dis. 2014 Mar;63(3):464-78. doi: 10.1053/j.ajkd.2013.08.023. Epub 2013 Oct 30. PMID: 24183112.

36. Oliver MJ. The Science of Fistula Maturation. JASN Nov 2018, 29 (11) 2607-2609; DOI: 10.1681/ASN.2018090922.

37. Hammes M, Boghosian M, Cassel K, Watson S, Funaki B, et al. (2016) Increased Inlet Blood Flow Velocity Predicts Low Wall Shear Stress in the Cephalic Arch of Patients with Brachiocephalic Fistula Access. PLOS ONE 11(4): e0152873. https://doi.org/10.1371/journal.pone.0152873.

38. Fitts MK, Pike DB, Anderson K, Shiu YT. Hemodynamic Shear Stress and Endothelial Dysfunction in Hemodialysis Access. Open Urol Nephrol J. 2014;7(Suppl 1 M5):33-44. doi: 10.2174/1874303X01407010033. PMID: 25309636; PMCID: PMC4189833.

39. Jean-Marc Corpataux, Erik Haesler, Paolo Silacci, Hans Beat Ris, Daniel Hayoz, Low-pressure environment and remodelling of the forearm vein in Brescia–Cimino haemodialysis access, Nephrology Dialysis Transplantation, Volume 17, Issue 6, June 2002, Pages 1057–1062, https://doi.org/10.1093/ndt/17.6.1057.

40. Hammes M, Cassel K, Boghosian M, Watson S, Funaki B, Coe F. A cohort study showing correspondence of low wall shear stress and cephalic arch stenosis in brachiocephalic arteriovenous fistula access. J Vasc Access. 2020.

41. Boghosian M, Cassel K, Hammes M, Funaki B, Kim S, Qian X, et al. Hemodynamics in the cephalic arch of a brachiocephalic fistula. Medical Engineering and Physics. 2014;36(7):822-30. doi: 10.1016/j.medengphy.2014.03.001.

42. Sigovan M, Rayz V, Gasper W, Alley HF, Owens CD, Saloner D. Vascular remodeling in autogenous arterio-venous fistulas by MRI and CFD. Annals of Biomedical Engineering. 2013;41(4):657-68. doi: 10.1007/s10439-012-0703-4.

43. Ene-Iordache B, Remuzzi A. Disturbed flow in radial-cephalic arteriovenous fistulae for haemodialysis: Low and oscillating shear stress locates the sites of stenosis. Nephrology Dialysis Transplantation. 2012;27(1):358-68. doi: 10.1093/ndt/gfr342.

44. Hammes M, Moya-Rodriguez A, Bernstein C, Nathan S, Navuluri R, Basu A. Computational modeling of the cephalic arch predicts hemodynamic profiles in patients with brachiocephalic fistula access receiving hemodialysis. PLoS One. 2021;16(7 July). doi: 10.1371/journal.pone.0254016.

45. Hammes M: Importance of the Endothelium in Arteriovenous Fistula Outcomes. Am J Nephrol 2016;44:426-427. doi: 10.1159/000452429.

46. Hammes M, McGill RL, Basu A, Blicharski T, Delaney K. Hemodynamic effects of hemodialyzer pump speed on arteriovenous fistulas. Clin Nephrol. 2019 Mar;91(3):138-146. doi: 10.5414/CN109456. PMID: 30526815.

47. Ene-Iordache B, Remuzzi A. Blood Flow in Idealized Vascular Access for Hemodialysis: A Review of Computational Studies. Cardiovasc Eng Technol. 2017 Sep;8(3):295-312. doi: 10.1007/s13239-017-0318-x. Epub 2017 Jun 29. PMID: 28664239.

48. Hull JE, Balakin BV, Kellerman BM, Wrolstad DK. Computational fluid dynamic evaluation of the side-to-side anastomosis for arteriovenous fistula. J Vasc Surg. 2013 Jul;58(1):187-93.e1. doi: 10.1016/j.jvs.2012.10.070. Epub 2013 Feb 20. PMID: 23433819.

49. Remuzzi A, Bozzetto M, Brambilla P. Is shear stress the key factor for AVF maturation? J Vasc Access. 2017 Mar 6;18(Suppl. 1):10-14. doi: 10.5301/jva.5000686. Epub 2017 Mar 5. PMID: 28297046.

50. Kroll MH, Hellums JD, McIntire LV, Schafer AI, Moake JL. Platelets and shear stress. Blood. 1996 Sep 1;88(5):1525-41. PMID: 8781407.

51. Teodorescu V, Gustavson S, Schanzer H. Duplex ultrasound evaluation of hemodialysis access: a detailed protocol. Int J Nephrol. 2012;2012:508956. doi: 10.1155/2012/508956. Epub 2012 Jul 10. PMID: 22848824; PMCID: PMC3400354.

52. Logason K, Bärlin T, Jonsson ML, Boström A, Hårdemark HG, Karacagil S. The importance of Doppler angle of insonation on differentiation between 50-69% and 70-99% carotid artery stenosis. Eur J Vasc Endovasc Surg. 2001 Apr;21(4):311-3. doi: 10.1053/ejvs.2001.1331. PMID: 11359330.

53. Bozzetto M, Rota S, Vigo V, Casucci F, Lomonte C, Morale W, Senatore M, Tazza L, Lodi M, Remuzzi G, Remuzzi A. Clinical use of computational modeling for surgical planning of arteriovenous fistula for hemodialysis. BMC Med Inform Decis Mak. 2017 Mar 14;17(1):26. doi: 10.1186/s12911-017-0420-x. PMID: 28288599; PMCID: PMC5348915.

54. John E. Carroll, Eamonn S. Colley, Shannon D. Thomas, Ramon L. Varcoe, Anne Simmons, Tracie J. Barber. Tracking geometric and hemodynamic alterations of an arteriovenous fistula through patient-specific modelling, Computer Methods and Programs in Biomedicine, Volume 186, 2020, 105203.

55. Alberts B (2012). . Molecular Biology of the Cell. NCBI Bookshelf. Archived from the original on 27 March 2018. Retrieved 1 November 2012. ISBN-10 0-8153-3218-1.

56. Chhabra, R. P., Richardson, J.F. Non-Newtonian Flow and Applied Rheology: Engineering Applications. Netherlands: Elsevier Science, 2011. SN - 9780080951607.

57. Shinbrot, T. Biomedical Fluid Dynamics: Flow and Form. United Kingdom: Oxford University Press, 2019. SN – 9780198812586.

58. Shiu YT, Rotmans JI, Geelhoed WJ, Pike DB, Lee T. Arteriovenous conduits for hemodialysis: how to better modulate the pathophysiological vascular response to optimize vascular access durability. Am J Physiol Renal Physiol. 2019 May 1;316(5):F794-F806. doi: 10.1152/ajprenal.00440.2018. Epub 2019 Feb 20. PMID: 30785348; PMCID: PMC6580244.

59. Asif A, Roy-Chaudhury P, Beathard GA. Early arteriovenous fistula failure: a logical proposal for when and how to intervene. Clin J Am Soc Nephrol. 2006 Mar;1(2):332-9. doi: 10.2215/CJN.00850805. Epub 2005 Nov 30. PMID: 17699225.

60. Cheng HS, Chang TI, Chen CH, Hsu SC, Hsieh HL, Chen CY, Huang WC, Sue YM, Lin FY, Shih CM, Chen JW, Lin SJ, Huang PH, Liu CT. Study protocol for a prospective observational study to investigate the role of luminal pressure on arteriovenous fistula maturation. Medicine (Baltimore). 2019 Oct;98(40):e17238. doi: 10.1097/MD.0000000000017238. PMID: 31577715; PMCID: PMC6783230.

61. Ren C, Chen J, Wang Y, Huang B, Lu W, Cao Y, Yang X. Application of ultrasonography in monitoring the complications of autologous arteriovenous fistula in hemodialysis patients. Medicine (Baltimore). 2018 Nov;97(44):e12994. doi: 10.1097/MD.0000000000012994. PMID: 30383654; PMCID: PMC6221746.

62. Shammas NW, Radaideh Q, Shammas WJ, Daher GE, Rachwan RJ, Radaideh Y. The role of precise imaging with intravascular ultrasound in coronary and peripheral interventions. Vasc Health Risk Manag. 2019 Aug 7;15:283-290. doi: 10.2147/VHRM.S210928. PMID: 31496717; PMCID: PMC6689566.

63. Boghosian ME, Hammes MS, Cassel KW, Akherat SMJ, Coe F. Restoration of wall shear stress in the cephalic vein during extreme hemodynamics. J Med Eng Technol. 2018 Nov;42(8):617-627. doi: 10.1080/03091902.2019.1591534. Epub 2019 Apr 3. PMID: 30942634; PMCID: PMC6714973.

64. Lu DY, Chen EY, Wong DJ, Yamamoto K, Protack CD, Williams WT, Assi R, Hall MR, Sadaghianloo N, Dardik A. Vein graft adaptation and fistula maturation in the arterial environment. J Surg Res. 2014 May 1;188(1):162-73. doi: 10.1016/j.jss.2014.01.042. Epub 2014 Jan 30. PMID: 24582063; PMCID: PMC3972303.

65. Hu Z, Zhu F, Zhang N, Zhang C, Pei G, Wang P, Yang J, Guo Y, Wang M, Wang Y, Yang Q, Zhu H, Liao W, Zhang Z, Yao Y, Zeng R, Xu G. Impact of arteriovenous fistula blood flow on serum il-6, cardiovascular events and death: An ambispective cohort analysis of 64 Chinese hemodialysis patients. PLoS One. 2017 Mar 7;12(3):e0172490. doi: 10.1371/journal.pone.0172490. PMID: 28267753; PMCID: PMC5340356.

66. Nikam M, Chemla ES, Evans J, Summers A, Brenchley P, Tavakoli A, Roy-Chaudhury P, Mitra S. Prospective controlled pilot study of arteriovenous fistula placement using the novel Optiflow device. J Vasc Surg. 2015 Apr;61(4):1020-5. doi: 10.1016/j.jvs.2014.11.082. Epub 2015 Jan 13. PMID: 25595404.

67. Karydis N, Bevis P, Beckitt T, Silverberg D, Halak M, Calder F. An Implanted Blood Vessel Support Device for Arteriovenous Fistulas: A Randomized Controlled Trial. Am J Kidney Dis. 2020 Jan;75(1):45-53. doi: 10.1053/j.ajkd.2019.05.023. Epub 2019 Aug 22. PMID: 31447072.

68. Kassem EL, Alghamdi I, Vazquez-Padron R, Asif A, Lenz O, Sanjar T, et al. The role of endovascular stents in dialysis access maintenance. Advances in chronic renal failure. 2015; 22(6):453-458.

69. Schneider CA, Rasband WS, Eliceiri KW. NIH Image to ImageJ: 25 years of image analysis. Nat Methods. 2012 Jul;9(7):671-5. doi: 10.1038/nmeth.2089. PMID: 22930834; PMCID: PMC5554542.

70. Millon A, Sigovan M, Boussel L, Mathevet JL, Louzier V, Paquet C, Geloen A, Provost N, Majd Z, Patsouris D, Serusclat A, Canet-Soulas E. Low WSS Induces Intimal Thickening, while Large WSS Variation and Inflammation Induce Medial Thinning, in an Animal Model of Atherosclerosis. PLoS One. 2015 Nov 17;10(11):e0141880. doi: 10.1371/journal.pone.0141880. PMID: 26575029; PMCID: PMC4648591.

71. Zhang G, Zhang S, Qin Y, Fang J, Tang X, Li L, Zhou Y, Wu D, Yan S, Liu WV, Zhu W. Differences in Wall Shear Stress Between High-Risk and Low-Risk Plaques in Patients With Moderate Carotid Artery Stenosis: A 4D Flow MRI Study. Front Neurosci. 2021 Aug 11;15:678358. doi: 10.3389/fnins.2021.678358. PMID: 34456667; PMCID: PMC8385133.

72. Jia L, Wang L, Wei F, Yu H, Dong H, Wang B, Lu Z, Sun G, Chen H, Meng J, Li B, Zhang R, Bi X, Wang Z, Pang H, Jiang A. Effects of wall shear stress in venous neointimal hyperplasia of arteriovenous fistulae. Nephrology (Carlton). 2015 May;20(5):335-42. doi: 10.1111/nep.12394. PMID: 25581663.

73. Khan MO, Tran JS, Zhu H, Boyd J, Packard RRS, Karlsberg RP, Kahn AM, Marsden AL. Low Wall Shear Stress Is Associated with Saphenous Vein Graft Stenosis in Patients with Coronary Artery Bypass Grafting. J Cardiovasc Transl Res. 2021 Aug;14(4):770-781. doi: 10.1007/s12265-020-09982-7. Epub 2020 Apr 2. PMID: 32240496; PMCID: PMC7529767.

74. Hammer PE, McEnaney K, Callahan R, Baird CW, Hoganson DM, Jenkins KJ. The Role of Elevated Wall Shear Stress in Progression of Pulmonary Vein Stenosis: Evidence from Two Case Studies. Children (Basel). 2021 Aug 25;8(9):729. doi: 10.3390/children8090729. PMID: 34572161; PMCID: PMC8470228.

75. Kudze T, Ono S, Fereydooni A, Gonzalez L, Isaji T, Hu H, Yatsula B, Taniguchi R, Koizumi J, Nishibe T, Dardik A. Altered hemodynamics during arteriovenous fistula remodeling leads to reduced fistula patency in female mice. JVS Vasc Sci. 2020;1:42-56. doi: 10.1016/j.jvssci.2020.03.001. Epub 2020 Mar 17. PMID: 32754721; PMCID: PMC7402599.

76. Colley E, Simmons A, Varcoe R, Thomas S, Barber T. Arteriovenous fistula maturation and the influence of fluid dynamics. Proceedings of the Institution of Mechanical Engineers, Part H: Journal of Engineering in Medicine. 2020;234(11):1197-1208. doi:10.1177/0954411920926077.

77. Vitello DJ, Ripper RM, Fettiplace MR, Weinberg GL, Vitello JM. Blood Density Is Nearly Equal to Water Density: A Validation Study of the Gravimetric Method of Measuring Intraoperative Blood Loss. J Vet Med. 2015;2015:152730. doi: 10.1155/2015/152730. Epub 2015 Jan 29. PMID: 26464949; PMCID: PMC4590883.

78. Nader E, Skinner S, Romana M, Fort R, Lemonne N, Guillot N, Gauthier A, Antoine-Jonville S, Renoux C, Hardy-Dessources MD, Stauffer E, Joly P, Bertrand Y, Connes P. Blood Rheology: Key Parameters, Impact on Blood Flow, Role in Sickle Cell Disease and Effects of Exercise. Front Physiol. 2019 Oct 17;10:1329. doi: 10.3389/fphys.2019.01329. PMID: 31749708; PMCID: PMC6842957.

79. Bolelli F, Allegretti S, Baraldi L, Grana C. Spaghetti Labeling: Directed Acyclic Graphs for Block-Based Connected Components Labeling. IEEE Transactions on Image Processing. 2020;29(1):1999-2012. doi: 10.1109/TIP.2019.2946979.

80. Baskurt OK, Meiselman HJ. Blood rheology and hemodynamics. Semin Thromb Hemost. 2003 Oct;29(5):435-50. doi: 10.1055/s-2003-44551. PMID: 14631543.

81. Van Tricht I, De Wachter D, Tordoir J, Verdonck P. Hemodynamics and Complications Encountered with Arteriovenous Fistulas and Grafts as Vascular Access for Hemodialysis: A Review. Annals of Biomedical Engineering. 2005;33(9):1142-57. doi: 10.1007/s10439-005-5367-X.

82. Hathcock JJ. Flow effects on coagulation and thrombosis. Arterioscler Thromb Vasc Biol. 2006 Aug;26(8):1729-37. doi: 10.1161/01.ATV.0000229658.76797.30. Epub 2006 Jun 1. PMID: 16741150.

83. Casa LD, Deaton DH, Ku DN. Role of high shear rate in thrombosis. J Vasc Surg. 2015 Apr;61(4):1068-80. doi: 10.1016/j.jvs.2014.12.050. Epub 2015 Feb 19. PMID: 25704412.

84. Shirazian S, Rios-Rojas L, Drakakis J, Dikkala S, Dutka P, Duey M, et al. The effect of hemodialysis ultrafiltration on changes in whole blood viscosity. Hemodialysis International. 2012;16(3):342-50. doi: https://doi.org/10.1111/j.1542-4758.2012.00671.x.

85. Jain A, van der Meer AD, Papa AL, Barrile R, Lai A, Schlechter BL, Otieno MA, Louden CS, Hamilton GA, Michelson AD, Frelinger AL 3rd, Ingber DE. Assessment of whole

blood thrombosis in a microfluidic device lined by fixed human endothelium. Biomed Microdevices. 2016 Aug;18(4):73. doi: 10.1007/s10544-016-0095-6. PMID: 27464497; PMCID: PMC4963439.

86. Rios DR, Carvalho MG, Figueiredo RC, Ferreira CN, Rodrigues VL, Souza RA, e Silva AC, Fernandes AP, Gomes KB, Dusse LM. ADAMTS13 and Von Willebrand factor in patients undergoing hemodialysis. J Thromb Thrombolysis. 2012 Jul;34(1):73-8. doi: 10.1007/s11239-012-0682-1. PMID: 22298244.

87. Péquériaux NC, Fijnheer R, Gemen EF, Barendrecht AD, Dekker FW, Krediet RT, Beutler JJ, Boeschoten EW, Roest M. Plasma concentration of von Willebrand factor predicts mortality in patients on chronic renal replacement therapy. Nephrol Dial Transplant. 2012 Jun;27(6):2452-7. doi: 10.1093/ndt/gfr735. Epub 2011 Dec 20. PMID: 22189209.